This is to certify that the
dissertation entitled

STRUCTURAL TRANSITIONS IN NANOSCALE SYSTEMS

presented by

Mina Yoon

has been accepted towards fulfillment
of the requirements for the

Ph.D. degree in Physics

David Tománek

Major Professor's Signature

06/22/2004

Date

MSU is an Affirmative Action/Equal Opportunity Institution

STRUCTURAL TRANSITIONS IN NANOSCALE SYSTEMS

By

Mina Yoon

A DISSERTATION

Submitted to
Michigan State University
in partial fulfillment of the requirements
for the degree of

DOCTOR OF PHILOSOPHY

Physics

2004

ABSTRACT

STRUCTURAL TRANSITIONS IN NANOSCALE SYSTEMS

By

Mina Yoon

In this work I investigate three different materials: nanoscale carbon systems, ferrofluid systems, and molecular-electronic devices. In particular, my study is focused on the theoretical understanding of structural changes and the associated electronic, mechanical, and magnetic properties of these materials.

To study the equilibrium packing of fullerenes in carbon nanotube peapods optimization techniques were applied. In agreement with experimental measurements, my results for nanotubes containing fullerenes with 60-84 atoms indicate that the axial separation between the fullerenes is smaller than in the bulk crystal. The reduction of the inter-fullerene distance and also the structural relaxation of fullerenes result from a large internal pressure within the peapods. This naturally induced "static" pressure may qualify nanotubes as nanoscale autoclaves for chemical reactions.

Combining total energy calculations with a search of phase space, I investigated the microscopic fusion mechanism of C_{60} fullerenes. I show that the $(2+2)$ cycloaddition reaction, a necessary precursor for fullerene fusion, can be accelerated inside a nanotube. Fusion occurs along the minimum energy path as a finite sequence of Stone-Wales (SW) transformations. A detailed analysis of the transition states shows that Stone-Wales transformations are multi-step processes.

I propose a new microscopic mechanism to explain the unusually fast fusion process of carbon nanotubes. The detailed pathway for two adjacent $(5,5)$ nanotubes to gradually merge into a $(10,10)$ tube, and the transition states have been identified. The propagation of the fused region is energetically favorable and proceeds in a morphology reminiscent of a Y-junction via a so called zipper mechanism, involving only

SW bond rearrangements with low activation barriers.

Using density functional theory, the equilibrium structure, stability, and electronic properties of nanostructured, hydrogen terminated diamond fragments have been studied. Such diamondoids can enter spontaneously into carbon nanotubes where polymerization of diamondoids is favourable.

I studied the equilibrium structure of large but finite aggregates of magnetic dipoles, modeling a colloidal suspension of magnetite particles in a ferrofluid. With increasing system size, the structural motif evolves from chains and rings to multi-chain and multi-ring assemblies. These structural changes depend on external parameters and result from a competition between various energy terms, which can be described analytically within a continuum approximation.

I use advanced quaternion molecular dynamics to model a potential application of magnetic nanostructures for targeted medication delivery. Inert microcapsules, containing the active medication and a small number of magnetite nanoparticles, may be transported using an inhomogeneous magnetic field through blood vessels to a desired location in the body. Triggered by an abrupt change in the applied field, structure of magnetite aggregates changes from a ring to a chain, thus puncturing the microcapsule and releasing the medication. The stability of the system under thermal and magnetic fluctuations has also been studied.

The investigation of the energetics, electronic structure and electron transport properties of oligo (phenylene ethylene) molecules shows that a net charge transfer to the molecules, induced by applying a bias voltage can result in a transition from the stable planar to a less stable twisted isomer. This structural transition alternates significantly its electric properties from a conducting to an insulating state.

Table of Contents

List of Figures

Chapter 1

Introduction

I have studied three different nanoscale materials: nanoscale carbon materials, ferrofluid systems, and molecular electronic devices. These seemingly completely different systems share interesting aspects that are both fundamentally interesting, and could be useful for applications in nanotechnology. My work was in particular focused on understanding structural transitions in those materials. It turns out that even minor structural changes in such nanoscale systems may dramatically affect their physical properties. Understanding ways to achieve such structural modifications will thus enable us to change the physical properties of these nanostructures. Hence, theoretical understanding of structural transitions opens a wide range of applications and is fundamentally important for the development of nanotechnology.

1. Nanoscale Carbon Materials

Carbon-based materials are unique due to the large variety of chemical bonding they exhibit. Depending on whether the interatomic bonds are sp, sp^2 or sp^3, the morphology ranges from linear chains to planar graphite and the bulk diamond structure. Among these, the 3-dimensional network of sp^3 diamond and 2-dimensional sheets of sp^2 graphite are prevalent due to their stability. The discovery of low dimensional carbon materials, such as fullerenes and nanotubes, has attracted great research interest during the past two decades. Their unique mechanical and electrical properties open new possibilities in many areas of nanotechnology.

I have focused my studies on selected mechanical, electrical, and magnetic properties of various nanoscale carbon materials such as carbon nanotubes, fullerenes, hybrid structures of nanotubes and fullerenes, carbon foams, and nanoscale diamond.

My study of 'peapods', consisting of fullerenes encapsulated in nanotubes, was inspired by the High-Resolution Transmission Electron Microscopy (HRTEM) observations of these systems. Nanotube peapods could be used as diodes, logic circuits based on single fullerene molecules or for quantum computing.

Some of the structural aspects of carbon nanotube peapods are intriguing, and even appear counter-intuitive. In particular, the equilibrium structure of fullerenes in peapods is quantitatively different from that in bulk solids. HRTEM images, electron diffraction and Raman measurements suggest that the equilibrium spacing between fullerenes in peapods is smaller by $3-4\%$ than in three-dimensional molecular crystals, but larger than in solids based on polymerized fullerenes. I investigated the energetics and the packing of fullerenes being encapsulated in nanotubes. I found a net energy gain associated with fullerene encapsulation in nanotubes, giving rise to a "capillary force". In nanotube peapods, this force compresses encapsulated fullerenes with an effective pressure of the order of GPa, inducing a strain in the nanotube wall. The naturally induced pressure in nanotube peapods could turn them into chemical reactors. The strain in the nanotube wall, associated with closely packed fullerenes, modifies locally the reactivity of the tube wall, which could be used for chemical functionalization. I also identified the optimum geometry of fullerenes and nanotubes, which maximizes the encapsulation energy.

Due to the unusual stability of the graphitic sp^2 bond, large-scale structural changes in bulk fullerene crystals occur only under extremely high pressures and temperatures. On the other hand, fullerenes in nanotube peapods have been observed to fuse at relatively low temperature near 1,100°C, far below the melting of fullerenes near 4,000°C, which seems puzzling. No information is available about the detailed fusion process except the obvious conclusion that strong sp^2 bonds should not be broken during structural rearrangements leading to fusion. In view of the fact that even minor structural changes in carbon nanostructures may modify significantly their physical properties, including magnetism, there is additional interest in understanding fusion as a way to control large-scale structural transformations.

In a collaborative research effort, I found that large-scale structural changes and also fusion can be achieved by a finite sequence of generalized Stone-Wales transformations, involving only bond rotation and avoid bond breaking. Also, the details of the transition states were identified so that the reaction time could be estimated. It turns out that the Stone-Wales transformations are multi-step processes with lower individual activation barriers. Especially, the C_{60} $(2+2)$ cycloaddition reaction [1], a necessary precursor for fullerene fusion, can be accelerated inside a nanotube.

Not only the fusion mechanism of fullerenes, but also that of nanotubes has been studied, to enable the use of nanoscale materials as potential building blocks for nanotechnology applications. I proposed a new microscopic mechanism to explain the unusually efficient fusion process of carbon nanotubes, where the pathway for the fusion process involves a sequence of Stone-Wales type bond rearrangements rather than energy intensive bond breakings. The zipper-like fusion mechanism proceeds by increasing the waist at the expense of the leg segments, and is energetically favorable. This finding offers a new insight into the observed fast coalescence of single-walled carbon nanotubes under irradiation and heating in a High-Resolution Transmission Electron Microscope.

---

[1] $(2+2)$ cycloaddition reaction is the reactions of two alkenes to form a cyclic product. In the peapod, the $(2+2)$ cycloaddition is initiated by two 'double bonds' facing each other in adjacent fullerenes.

It has been known that the minute changes in the spatial arrangement of carbon atoms can profoundly alter the electronic properties of materials such as nanotubes from a semiconductor to a metal or superconductor. One could expect that structural rearrangements might also significantly change the magnetic properties of all-carbon allotropes from their known diamagnetic behaviour. Only recently, a weakly magnetic all-carbon structure has been reported, formed under high-pressure and high-temperature conditions, consisting of rhombohedrally polymerized C_{60} molecules. Other experimental observations suggest the occurrence of ferromagnetism in a semiconducting nanostructured carbon foam with a low mass density.

In a collaborative effort I also investigated the possibility that structural changes in nanoscale carbon materials can significantly change the magnetic properties of all-carbon materials from their known diamagnetic behaviour. The unexpected magnetic behaviour of all-carbon systems can be quantitatively interpreted using spin-polarized *ab initio* calculations. Our results suggest that unpaired spins are introduced by sterically protected carbon radicals, which are immobilised in the non-alternant aromatic system of sp^2 bonded carbon with negative Gaussian curvature. This new mechanism to generate unpaired spins in semiconductors may find a useful application in the emerging field of spintronics.

A new class of carbon nanostructures, hydrogen terminated nanoscale diamond fragments ("diamondoids"), has been successfully isolated experimentally. The isolated diamondoids occur in very different shapes, and many of them form molecular crystals. These nanoscale building blocks are very different, but compare well in stability and light weight with fullerenes and nanotubes. These uncommon organic molecules can be chemically functionalized, by substituting carbon or hydrogen atoms at the surface by other atoms or groups, to promote formation of specific polymers.

I followed up on the interesting question whether these fragments can be encapsulated in nanotubes to make functional building blocks. These studies involved investigating the equilibrium structure, stability, and electronic properties of nanostructured, hydrogen terminated diamond fragments. The equilibrium atomic arrangement and electronic structure of these nanostructures turn out to be very similar to bulk diamond. I found that such diamondoids may enter spontaneously into carbon nanotubes that are wide enough .

2. Ferrofluid Systems

Ferrofluids, colloidal suspensions of magnetic particles in liquid carriers, are a unique class of materials, with high potential use in nanotechnology. The magnetic particles of an average size of about 10 nm are coated with a surfactant to prevent particle aggregation. They contain a single magnetic domain because of their small size. Many applications rely on the strong magnetic interaction between individual dipoles in these complex liquids. There already is a well developed ferrofluid technology based on successful applications, enhancing the performance of mechanical or electromechanical devices.

Of fundamental interest is the fact that finite dipole aggregates display a plethora of nontrivial equilibrium structures due to the competition between the strongly anisotropic dipole-dipole interaction, favoring open structures, and isotropic interparticle forces as well as surface tension, which favor compact structures. Experimentally, a wide range of ferrofluid morphologies, ranging from compact structures to complex labyrinthine patterns, have been observed. Many studies of complex fluids focus on pattern formation with infinitely many particles. A more detailed understanding of the equilibrium geometry of ferrofluid systems is essential for developing applications.

To gain microscopic insight into the causes of pattern formation in ferrofluids, which is beyond the scope of present experimental observations, I performed total energy and structure optimization calculations for ferrofluid systems with a *finite* number of magnetic particles, where the surface tension of the aggregate plays a dominating role in its equilibrium structure. I found a structural evolution of systems from chains to multiple rings and multi-wall tubes, as the number of particles increases. I mapped the inter-particle interactions in the colloidal suspension onto a continuum model, which offers an efficient tool to study the structural changes depending on external parameters, such as an external magnetic field or the liquid-particle interaction.

I further used advanced quaternion molecular dynamics simulations to model a potential application of magnetic nanostructures for targeted medication delivery. Inert microcapsules, containing the active medication and a small number of magnetite nanoparticles, may be transported using an inhomogeneous magnetic field through blood vessels to a desired location in the body. Triggered by an abrupt change in the applied field, the structure of magnetite aggregates may change from a ring to a chain, thus puncturing the microcapsule and releasing the medication. I obtained new results for the stability of the magnetic nanostructures under thermal and magnetic fluctuations, an important issue related to preventing an accidental delivery.

3. Molecular Electronic Devices

The revolutionary history of electronic devices started with the invention of the transistor in 1947 by John Bardeen, William Shockley, and Walter Brattain. The development of integrated circuits by putting millions of transistors on a single silicon chip brought the foundation of the development of modern electronics. Since then the number of transistors on a chip has doubled ca. every 18 months; this exponential behavior is known as Moore's Law. Today's chips based on silicon include often more than 100 million transistors and the typical transistor size is about 100 nm[2]. However, basic theoretical limits of the performance of silicon-based transistors will probably

---

[2] In 2003 NEC developed a chip with the record number of 40 billion transistors.

be reached within a decade. To shrink the size of transistors, while following Moore's law, we will rely on new types of transistors, consisting of few atoms or molecules.

The advent of the Scanning Probe Microscopy in the 1980s offers a tool to observe individual molecules, which led in the 1990s to the observation of individual molecules as electron conductors. This discovery gave researchers a vision of computers containing molecules as circuit components, as suggested by Mark Ratner and Ari Aviram in 1974. Since the late 1990s, a series of successful attempts were undertaken to build molecular devices, including molecular diodes and molecular fuses. The effort to go beyond these basic nanodevices has already been made by wiring these devices up into more complex circuits. The preliminary step was achieved by making circuits out of a single semiconducting nanotube, semiconducting nanowires, and organic molecules by the end of 2001. At that time people were very euphoric and molecular-electronics-based computer chips were expected to be in the stores by 2005. But the implementation of molecular electronic turned out to be more problematic than anticipated.

I have contributed to a theoretical study of electronic and transport properties of oligo (phenylene ethylene) molecules sandwiched between two gold electrodes. This system is an interesting representative of organic molecules being used in molecular electronic devices. Due to their small size, in comparison with the electron mean free path, individual molecules conduct electrons in the 'ballistic' regime, without internal Joule heat dissipation. I used the Landauer-Büttiker formalism to calculate the quantum conductance through molecules, such as oligo (phenylene ethylene) as a function of their structure.

I found that a net charge transfer to the molecule, possibly correlated with the applied bias voltage, may cause an internal twist within a monolayer of charged molecules. Since the twisted molecule acts as an insulator, whereas the planar molecule is a good conductor, this device can be viewed as a molecular switch. When this molecule is entangled in a monolayer, its change from the energetically unfavorable twisted state to the planar ground state may be delayed due to inter-molecular interactions, resulting in a memory effect.

Chapter 2

Structural Changes in Nanoscale Carbon Materials

2.1 Theoretical Techniques

The total energy of fullerene-nanotube systems has been calculated based on an energy functionals using a linear combination of atomic orbitals (LCAO). This functional successfully described the formation of peapods [1], multi-wall nanotubes [2], the dynamics of the "bucky-shuttle" [3], and the melting of fullerenes [4].

Our total energy formalism describes accurately not only the covalent bonding within the sp^2 bonded graphitic substructures, but also the modification of the fullerene-nanotube interaction due to the inter-wall interaction and weak inter-fullerenes interaction. We find the use of an electronic Hamiltonian to be required in this system, as analytical bond-order potentials do not describe the rehybridization during the fullerene or nanotube fusion process with a sufficient precision. Our numerical results based on LCAO basis are compared to the first principles pseudopotential method [5, 6] that employs a numerical basis set for localized atomic orbitals [7], and which has been applied successfully to nanotubes and fullerenes [8].

When we consider the energetics and electronic structures of nanoscale diamonds, we employ methods based on the *ab initio* density functional theory (DFT) within the local density approximation (LDA). We use Troullier-Martins pseudo-potentials to describe the effect of atomic nuclei plus core electrons on the valence electrons, and the Perdew-Zunger parametrized exchange-correlation potential, as implemented in the SIESTA code [9]. Our optimized diamondoid structures are in good agreement with those inferred experimentally [10, 11] and theoretically [12, 13].

The magnetic properties of different nanoscale carbon tetrapods were investigated using the first principles pseudopotential method [5, 6] within the local spin density approximation (LSDA) [14, 15]. To facilitate the numerical treatment of very large aggregates containing hundreds of atoms within LSDA, we make use of our recently developed approach based on an atom-centered numerical basis set [16], proven to describe correctly similar carbon systems [17].

2.1.1 Total Energy Calculations: *Ab initio* Density Functional Theory

The fundamental Hamiltonian of many-body system is

$$\begin{aligned} H = -\sum_{i} \frac{\hbar^2}{2m_e} \nabla_i^2 + \sum_{i,I} \frac{Z_I e^2}{|\mathbf{r}_i - \mathbf{R}_I|} + \frac{1}{2} \sum_{i \neq j} \frac{e^2}{|\mathbf{r}_i - \mathbf{r}_j|} \\ - \sum_{I} \frac{\hbar^2}{2M_I} \nabla_I^2 + \frac{1}{2} \sum_{I \neq J} \frac{Z_I Z_J e^2}{|\mathbf{R}_I - \mathbf{R}_J|}. \end{aligned}$$

Usually, the nuclear degrees of freedom are frozen in, and our interest focuses on the electronic degrees of freedom. This all-electron Hamiltonian can be decomposed as

$$H = T + V_{ext} + V_{int}, \tag{2.1}$$

where T is the kinetic energy of electrons, V_{ext} is the potential energy acting on the electrons due to the nuclei, and V_{int} is the many-body electron-electron interaction term. The total energy E can be evaluated by

$$E = \frac{<\Psi|H|\Psi>}{<\Psi|\Psi>}, \tag{2.2}$$

where $|\Psi>$ is the all-electron wavefunction.

In the electronic ground state, Density Functional Theory (DFT) allows us to replace the complex many-electron wavefunction and the associated Schrödinger equation by the total electron density $n(\mathbf{r})$ and a total energy functional, which depends only on $n(\mathbf{r})$. This approach is based on the Hohenberg and Kohn theorem [18], which states that the total energy of a system in the ground state $E[n]$ is a unique functional of the total charge density $n(\mathbf{r})$, except for a constant. An important corollary states that the correct density $n(\mathbf{r})$ can be obtained variationally by minimizing this functional. In analogy to Eq. 2.1, Hohenberg and Kohn separate the energy functional $E[n]$ as

$$E[n] = T[n] + \int d\mathbf{r} V_{ext}(\mathbf{r}) n(\mathbf{r}) + E_{int}[n], \tag{2.3}$$

where the explicit functional $E_{int}[n]$ is unknown.

Kohn and Sham [19] replaced the system of interacting electrons, which establish the total charge density by a system of non-interacting quasi-electrons with the same density. In this way, they were able to replace the many-electron Schrödinger equation by a set of one-(quasi)electron equations, the Kohn-Sham equations. Formally equivalent to the one-electron Schrödinger equation, the set of Kohn-Sham equations describes the behavior of a quasi-electron in an effective potential, which is a functional of the total electron density $n(\mathbf{r})$. The normalization of the Kohn-Sham wavefunctions ϕ_i of all occupied states, which yield $n(\mathbf{r})$, is established by Lagrange multipliers, which enter as Kohn-Sham energy eigenvalues ϵ_i,

$$(H_{eff} - \epsilon_i)\,\phi_i(\mathbf{r}) = 0. \tag{2.4}$$

The Kohn-Sham Hamiltonian acting on the Kohn-Sham states is

$$H_{eff}(\mathbf{r}) = -\frac{\hbar^2}{2m}\nabla^2 + V_{eff}(\mathbf{r}), \tag{2.5}$$

where

$$\begin{aligned} V_{eff}(\mathbf{r}) &= V_{ext}(\mathbf{r}) + \frac{\delta E_{Hartree}}{\delta n(\mathbf{r})} + \frac{\delta E_{XC}}{\delta n(\mathbf{r})} = \\ &= V_{ext}(\mathbf{r}) + V_{Hartree}[n] + V_{XC}[n]. \end{aligned}$$

These different contributions in the effective potential V_{eff} reflect the expression for the total energy, given as

$$E[n] = T_s + \int d\mathbf{r} V_{ext}(\mathbf{r}) n(\mathbf{r}) + E_{Hartree}[n] + E_{XC}[n]. \tag{2.6}$$

This translates to

$$E = \sum_{i=1}^{N} \epsilon_i - \frac{1}{2}\int d\mathbf{r} V_{Hartree}(\mathbf{r}) n(\mathbf{r}) + \left(E_{XC}[n] - \int d\mathbf{r} V_{XC} n(\mathbf{r})\right), \tag{2.7}$$

where

$$\begin{aligned} \sum_{i}^{N} \epsilon_i &= \left\langle \phi_i \middle| -\frac{1}{2}\nabla^2 + V_{eff} \middle| \phi_i \right\rangle \\ &= T_s[n] + \int d\mathbf{r} V_{eff}(\mathbf{r}) n(\mathbf{r}). \end{aligned}$$

For a given electron density n, the exchange-correlation energy functional E_{XC} is defined by Eq. 2.6 as the total energy difference between the exact total energy of the homogeneous electron gas, and the sum of $T[n]$, $E_{ext}[n]$, and $E_{Hartree}[n]$. There is no simple correlation between the quasi-electron wave functions ϕ_i and energies ϵ_i, and the corresponding observables in the interacting system. Only the total energy density $n(\mathbf{r})$ is rigorously correct.

The DFT calculation largely depends on the appropriate functional form for $E_{XC}[n]$. By definition, the universal exchange-correlation functional, $E_{XC}[n]$, and the exchange-correlation potential $V_{XC}(\mathbf{r})$, are exact for a homogeneous electron gas. In the Local Density Approximation (LDA), $E_{XC}[n]$ is replaced by

$$E_{XC} = \int d\mathbf{r} n \epsilon_{XC}(n(\mathbf{r})), \tag{2.8}$$

where ϵ_{XC} is energy density for the homogeneous electron gas. The LDA exchange-correlation functional may further be subdivided into an exchange functional E_X and a correlation energy E_C,

$$E_{XC}[n] = E_X[n] + E_C[n]. \tag{2.9}$$

The exchange functional can be calculated [20]

$$E_X[n] = -\frac{0.458}{r_s} Hartree, \tag{2.10}$$

where r_s ($\frac{4}{3}\pi r_s^3 = \frac{1}{n}$) is the average free-electron radius. The correlation term is found by substracting the kinetic and exchange energy from the total energy.

The numerical procedure within the DFT scheme is the following: An initial guess for the total electron density is used as input. The effective potential can be calculated based on the input density. Solving the Kohn-Sham equations yields a new electron density as the output of the calculation. This charge density output is used as the input for the next iteration. This procedure is repeated, until self-consistency is achieved.

2.1.2 Total Energy Calculations: Semiemprical Methods

The time-independent Schrödinger equation of a many-body system consisting of electrons and atomic nuclei is the following:

$$H\varphi = E\varphi,$$

where the exact Hamiltonian H within the Born-Oppenheimer approximation reads

$$H = -\sum_i \frac{\hbar^2}{2m_e}\nabla_i^2 + \sum_{i,I}\frac{Z_I e^2}{|r_i - R_I|} + \frac{1}{2}\sum_{i\neq j}\frac{e^2}{|r_i - r_j|},$$

which describes the motion of electrons in the field of atomic nuclei. Based on density functional theory the exact ground state energy can be found in principle as discussed in the previous section, yet the calculation is computationally costy. Approximations can be made in the Hamiltonian and the wavefunction to solve the Schrödinger equation in a computationally cheap way. The most common approximation to make is the independent electron model, 'one-electron model', in which the explicit interaction between electrons is ignored. Instead, each electron is described by the mean field created by other electrons and fixed nuclei. The corresponding one-electron wavefunction is called as a orbital.

Hückel Method

In the tight-binding approximation, it is assumed that the full molecular Hamiltonian can be approximated by the Hamiltonian for a single atom. Also, the localization of the bound levels of this atomic Hamiltonian is assumed. Therefore, it is natural to expand the tight-binding wavefunction $|\varphi>$ in a linear combination of atomic orbitals (LCAO) $|i>$,

$$|\varphi> = \sum_{i=1}^{N} c_i|i>$$

. This one-electron function contains no fundamental natures of the wave function such as the Pauli exclusion principle and the information about spins. Using a LCAO basis set, we can minimize the energy E with respect to the coefficient c_i by applying variational methods, which results the secular equation,

$$\sum_i c_i \left(H_{ji} - ES_{ji}\right) = 0,$$

where $j = 1, \cdots, N$, $H_{ji} = \langle j|H|i\rangle$, and $S_{ji} = \langle j|i\rangle$. To find non-trivial solutions, the following determinant needs to be solved,

$$\det|H_{ji} - ES_{ji}| = 0,$$

which determines the coefficients c_i and hence the molecular wavefunction and the energies. In the tight-binding method H_{ji} is zero unless j and i are nearest neighbor atoms: electrons are tightly bound.

Hückel [21] approximation goes further simplification in the tight-binding method by neglecting the overlap integrals between different atomic orbitals and by treating energy of all atomic orbitals to identical energy, i.e.:

$$H_{ii} = H_{jj} = \alpha, H_{ij} = H_{ji} = \beta,$$

$$S_{ii} = S_{jj} = 1, S_{ij} = S_{ji} = 0,$$

where α and β are called as the Coulomb integral and the hopping integral, respectively. The parameters can be determined based on experiments of other theoretical calculations. The Hückel hamiltonian can be written down in a matrix form,

$$H = \sum_i \alpha|i><i| + \sum_{i\neq j} \beta|i><j|.$$

Since the Hückel model does not take into account the repulsion between electrons nor the bond length, this model depends on the system topology. It has been very successfully in describing the π-system like certain polymer and planar hydrocarbons. However, for the non-planar system it is not obvious whether it correctly describes the system or not due the mixing between π and σ electrons in such systems.

In the extended Hückel method [22, 23], overlap integral has been taken account,

$$H_{ij} = \frac{1}{2} K S_{ij} (H_{ii} + H_{jj}),$$

where K is a fitting parameter based on the experiments or other theoretical information about the charge distribution in molecules or binding energy. K is usually taken between 1.0 and 2.0.

Parametrized Linear Combinations of Atomic Orbitals(LCAO)

Our energy formalism which is parametrized based on *ab initio* density functional methods, employs linear combinations of atomic orbitals (LCAO) as a basis set. This scheme treats the nonlocality of bonding in very large systems properly, yet scales linearly with the number of atoms so that molecular dynamics simulations for large clusters can be performed in a computationlly efficient way.

The total cohesive energy of a solid E^{coh} can be evaluated by the summation of all individual atomic binding energy E_i^{coh},

$$E^{coh} = \sum_i E_i^{coh}.$$

The binding energy of each atom i, E_i^{coh}, can be mapped into the summation of the attraction energy and the repulsion energy, E_i^r. The attraction energy, the local one-electron band structure energy (molecular orbital energy), originates from the rehybrization of orbitals. On the other hand, the repulsive interaction comes from the inter-nuclear interaction, closed-shell repulsion, and the correlation part containing all other effects.

In one-electron picture, the band structure energy [24] is written as

$$E_i^{bs} = -\int_{-\infty}^{E_F} (E - E_0) n_i(E) dE,$$

where E_F and E_0 represent the Fermi energy and the reference energy of an isolated atom, respectively. $n_i(E)$ indicates the local density of states at i. The local density of states at site i [25] can be evaluated by

$$n_i(E) = -\frac{1}{\pi} \mathrm{Im} \langle i|G|i\rangle ,$$

where the Green's function matrix can be obtained by

$$G(E) = \left(\frac{1}{E - H}\right).$$

Here, the Hamiltonian H, which determines the local density of states and hence the band structure energy, is based on the Slater-Koster parametrization [26] and evaluated using recursion technique [24]. It makes the use of the fact that the moments of the density of states of the local orbitals are related to the Hamiltonian [24].

The remaining energy contributions are combined into the repulsive energy E^r, which is parametrized by the pairwise interaction [27]. The repulsive energy at site i, the functional of local atomic density ρ_i, is fitted to a finite polynomial of ρ_i as follows

$$E_i^r[\rho_i] = \left(a_0 + a_1\rho_i + a_2\rho_i^2\right) \xi(\rho_i),$$

where ξ is a cutoff function and the local atomic density ρ_i is evaluated by

$$\rho_i = \sum_{i \neq j} \left[\frac{d_0}{r_{ij}} \exp(-\frac{r_{ij}}{\sigma}) \right]^{\mu} \chi_{ij},$$

where r_{ij} is the distance between site i and j. χ_{ij} $(0 < \chi_{ij} < 1)$ is described by a Fermi-Dirac function with a cutoff r_c, which determines whether the connection between the site i and j is to be considered a bond. The parameters (a_0, a_1, a_2, d_0, σ, μ, r_c, ξ) for carbon have been obtained from a global fit to density functional calculation with LDA for the electronic structure of a carbon chain, a graphite monolayer and bulk diamond for different nearest-neighbor distances [28, 30, 24].

2.2 Equilibrium Packing Geometry of Fullerenes in Nanotube Peapods

The following discussion on the equilibrium packing geometry of fullerenes and nanotube peapods follows that presented in Reference [31].

I use structure optimization techniques to study the equilibrium packing of fullerenes in carbon nanotube peapods. My results for nanotubes containing fullerenes with 60-84 atoms indicate that the axial separation between the fullerenes is smaller than in the bulk crystal, in agreement with High-Resolution Transmission Electron Microscopy and electron diffraction measurements. According to our calculation, the reduction of the inter-fullerene distance and also the structural relaxation of fullerenes result from a large internal pressure within the peapods. This naturally induced "static" pressure may utilize nanotube as a nanoscale autoclave for chemical reactions.

2.2.1 Introduction

Following the discovery of fullerenes [32] and carbon nanotubes [33] (NTs), nanotube peapods emerged as very interesting nanostructures [34]. The first observation of the hierarchical self-assembly of C_{60} molecules and single-wall carbon nanotubes (SWNTs) to peapods by High-Resolution Transmission Electron Microscopy (HRTEM) [34] was followed by reports of other fullerenes and metallofullerenes being encapsulated in single-walled carbon nanotubes [35, 36].

Some of the structural aspects of carbon nanotube peapods are intriguing, and even appear counter-intuitive. In particular, the equilibrium structure of fullerenes in peapods is quantitatively different from that in bulk solids. HRTEM images [37], electron diffraction [38] and Raman measurements [35] suggest that the equilibrium spacing between fullerenes in peapods is smaller by $3-4\%$ than in three-dimensional molecular crystals, but larger than in solids based on polymerized fullerenes. Elastic deformations, associated with a fullerene-to-nanotube charge transfer in the peapod, have been offered as a tentative explanation for the reduction of the inter-fullerene distance [35, 38]. Unfortunately, there is no independent evidence for such a charge transfer in these all-carbon systems. Also, like charges on adjacent fullerenes should enhance the inter-fullerene repulsion, thus increasing the inter-fullerene distance.

Here I investigate the energetics and packing of fullerenes upon their encapsulation in nanotubes. I find a net energy gain associated with fullerene encapsulation in nanotubes, giving rise to a "capillary force". In nanotube peapods, I find this force to compress encapsulated fullerenes with an effective pressure of the order of GPa, inducing strain in the nanotube wall. My results indicate that the encapsulation energy of fullerenes depends only on the diameter, not the chirality of the enclosing nanotube. For a given fullerene, I identify the optimum nanotube radius, which maximizes the encapsulation energy. The encapsulation energy is lower in wider nanotubes, and eventually approaches the adsorption energy of the fullerene on graphite in very wide tubes. Also in narrow nanotubes, encapsulation is energetically less favorable, and may even become endothermic. I map our total energy results for specific fullerene-nanotube combinations onto a continuum model, enabling us to make general predictions for axial separation and off-axis displacement of fullerenes in nanotube peapods.

2.2.2 Energetics of Fullerene Encapsulation

The energetics of fullerene encapsulation is described in Fig. 2.1. A static "capillary" force F, depicted in Fig. 2.1(a) and associated with the energy gain across a finite distance Δ_z during fullerene encapsulation, compresses other fullerenes in the peapod. The encapsulation energy [39] ΔE of isolated C_{60} and C_{84} fullerenes in single-wall nanotubes with radii in the range 0.6 nm$\leq R_{NT} \leq$0.8 nm is shown in

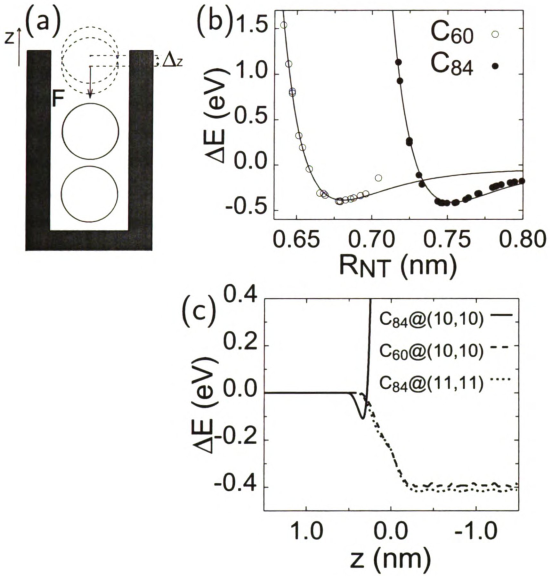

Figure 2.1: (a) During the insertion into a nanotube, a fullerene is pulled in by a "capillary" force F, which is linked to the energy gain upon axial displacement Δz. (b) The encapsulation energy ΔE of C_{60} (○) and C_{84} (●) in single-wall carbon nanotubes with radii ranging from 0.6 nm$\leq R_{NT} \leq$0.8 nm. Best fitting fullerene/nanotube pairs show an encapsulation energy of $\leq$0.4 eV. (c) Energy change during the fullerene insertion process along the tube axis z, with $z = 0$ at the tube end. C_{60} and C_{84} are pulled into the best fitting $(10, 10)$ and $(11, 11)$ nanotubes by $F \geq$0.1 nN, reflected in a constant slope of $\Delta E/\Delta z$ near the tube end. The high energy cost prevents the entry of the C_{84} fullerene into the narrow $(10, 10)$ nanotube.

Fig. 2.1(b). The results of our atomistic calculations, given by the data points, also reflect the relaxations in the nanotube peapod system. These data indicate how energetically favorable the encapsulation process is for a particular fullerene/nanotube combination. Following our expectations, only nanotubes with a radius R_{NT} beyond a threshold value may encapsulate a particular fullerene with an energy gain. Somewhat surprising is our result that the encapsulation energy ΔE seems to depend only on the nanotube radius and shows only a negligible dependence on the chirality of a particular (n, m) nanotube. I find the minimum of the $\Delta E(R_{NT})$ curve, reflecting the favorable fullerene/nanotube combination, at $\approx$0.4 eV for C_{60}@(10, 10) and C_{84}@(11, 11). This value agrees with *ab initio* calculations [40], but is lower than empirical fits to experimental data [41]. In general, we find the optimum snug fit to occur at $R_{NT} \approx R_F + 0.3$ nm, where R_F is the fullerene radius. Increasing the nanotube radius reduces the snug fit and the fullerene-nanotube attraction. For very large tube radii, the encapsulation energy should approach the fullerene adsorption energy on planar graphite. As expected, fullerene encapsulation is energetically less favorable and eventually turns endothermic with decreasing tube radius.

Close inspection of the structural relaxations in optimized peapods, both in absence and presence of an external force F, reveals that the major modifications occur in the inter-fullerene and fullerene-nanotube distances, with only a minor shape deformation of the fullerenes and the enclosing nanotube. Furthermore, I have found that the continuum approximation [42], which ignores discrete atomic positions, provides a good estimate of the packing geometry. Indeed, our data in Fig. 2.1(b) for near-spherical C_{60} and C_{84} fullerenes in various (n, m) nanotubes lie very close to model predictions for perfect spheres inside smooth tubes, given by the solid lines.

As mentioned above and shown in Fig. 2.1(c), the maximum energy gain upon encapsulation is close to 0.4 eV in case of the snug fit of C_{60}@(10, 11) or C_{84}@(11, 11). This energy gain near the tube end at z=0 occurs across the short distance $\Delta z \approx R_F \approx 0.5$ nm, resulting in a typical capillary force of $F \geq 0.1$ nN. Even though the insertion of C_{84} inside the narrow $(10, 10)$ nanotube is strongly energetically unfavorable, the potential well near the tube end may be used to manipulate a fullerene, which adheres to a carbon nanotube tip of a Scanning Probe Microscope (SPM) [43, 44].

At nonzero temperature, the static "capillary force" $F \geq 0.1$ nN is augmented by the force resulting from collisions between the encapsulated fullerenes. Assuming thermal equilibrium, the average collision force amounts to ≈ 0.5 nN at room temperature. In view of the small cross-section of the nanotube, the effective compressive force in the nN range translates into an effective pressure in the sub-GPa range. This effective pressure modifies the packing geometry, in particular reducing the inter-fullerene distance [35, 38]. In view of this high effective pressure, the nanotube may be considered a nanoscale pressure container or autoclave.

2.2.3 Packing of Fullerenes in Nanotube Peapods

The equilibrium geometry of the encapsulated fullerenes, which are subject to an external force F, is discussed in Fig. 2.2. This force can be thought of as being mediated by a "piston", shown schematically in Fig. 2.2(a). The main effect of the effective pressure is to reduce the axial inter-fullerene distance D_z, and to increase the off-axis displacement Δ. I focus my investigation on peapods based on 1.4 nm wide nanotubes, which are most abundant among the single-wall nanotubes, and which have been used in Ref. [38]. In the atomistic calculations, I considered the most stable fullerene isomers with 60-84 atoms, selected the $(18, 0)$ nanotube to represent 1.4 nm wide nanotubes of Ref. [38], and performed a global structure optimization for a given applied force. I found that also these results can be reproduced well by a continuum model, which considers rigid spheres contained in a rigid tube.

As suggested by our results in Fig. 2.1(b), the packing geometry inside an (n, m) nanotube depends primarily on its radius, given by $R_{NT} = 3.92 \times 10^{-2}$ nm $(m^2 +$

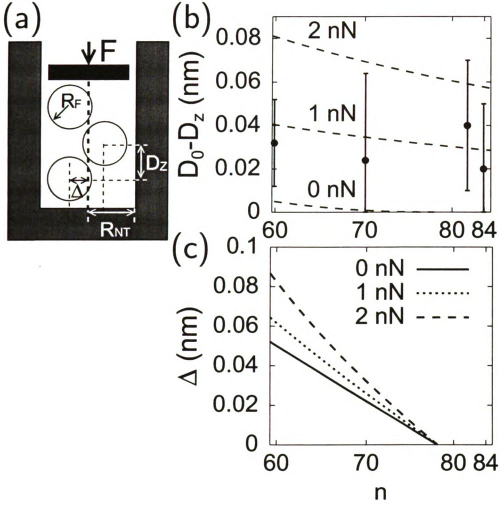

Figure 2.2: (a) An external "capillary" force F reduces the axial inter-fullerene distance D_z. An off-axis fullerene displacement Δ is expected especially if the fullerene radius R_F is much smaller than the nanotube radius R_{NT}. (b) Reduction of the axial inter-fullerene distance D_z in peapods with respect to the equilibrium separation D_0 in bulk crystals of C_n fullerenes with $60-84$ atoms. Observations for different fullerenes inside a 1.4 nm wide nanotube, reported in Ref. [38] and given by the data points with error bars, are compared to our analytical results for various applied forces F, shown by the dashed lines. (c) Predicted off-axis displacement Δ inside a 1.4 nm wide nanotube as a function of the fullerene size, for various applied forces F.

$mn + n^2)^{1/2}$, and not the chiral index. Similarly, I may neglect deviations from sphericity for encapsulated fullerenes, and will assume their mean radius to be given by $R_F = 4.58\times10^{-2}\text{nm}\ n^{1/2}$. I will also assume $d_{vdW} = 0.3$ nm as the equilibrium separation between the walls of fullerenes and nanotubes in absence of external forces. I find that close to equilibrium, the interaction energy between two C_n fullerenes can be expressed by a harmonic potential with the force constant $c_{FF} = (0.41n)$ N/m. In the limit of very wide nanotubes, the fullerene-nanotube interaction resembles the fullerene-graphite interaction, which also can be represented by a harmonic potential with the force constant $c_{FG} = (0.36n)$ N/m. With these values, the optimum packing structure within any peapod, consisting of fullerenes with radius R_F encapsulated inside a nanotube of radius R_{NT} and subject to an external force F can be determined analytically from total energy minimization.

My quantitative results for the reduction of the axial separation between C_n fullerenes inside a 1.4 nm wide nanotube are presented in Fig. 2.2(b). Comparison between my predictions and the experimental data of Ref. [38], suggesting an inter-fullerene distance reduction by 3 – 4% and displayed by the data points, suggests that encapsulated fullerenes are likely subject to an axial compressive force in the nN range, in agreement with my estimates above.

For peapods containing fullerenes with a radius below the optimum value $R_F = R_{NT} - d_{vdW}$, a nonzero off-axis displacement [45, 46] Δ of the encapsulated fullerenes is expected even for small external forces $F \rightarrow 0$. Increasing the fullerene radius leads to a more snug fit and reduces Δ, as seen in Fig. 2.2(c). Furthermore, in presence of an axial compressive force, we also find a significantly larger off-axis displacement, which has been observed by HRTEM [38].

In Fig. 2.3 I depict the strain distribution on the wall of nanotube peapods by displaying the reduction of the atomic binding energy. The schematic packing geometry of peapods containing too small and too large fullerenes is shown in Figs. 2.3(a) and

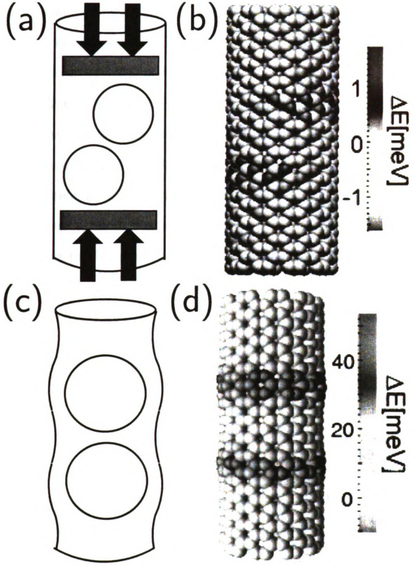

Figure 2.3: (a) In peapods containing fullerenes equal to or smaller than the optimum size, strain in the nanotube wall is induced by an axial force. (b) Strain distribution on the wall of a $(10, 10)$ nanotube containing C_{60} fullerenes, subject to the axial force of 0.5 nN. (c) In peapods containing fullerenes exceeding the optimum size, strain is induced even in absence of an axial force. (d) Strain distribution on the wall of a $(10, 10)$ nanotube containing C_{84} fullerenes. The strain energy is represented by the reduction of the atomic binding energy on a grey scale in (b) and (d).

2.3(c), respectively. Our results in Fig. 2.3(b) suggest that the strain on the $(10,10)$ nanotube, induced by C_{60} molecules, is localized near the fullerenes. When subject to an axial compressive force of 0.5 nN, the encapsulated fullerenes press towards the nanotubes wall, thus locally reducing the atomic binding energy by as much as 1 meV from the initial value of $\approx$7 eV/atom.

In Fig. 2.3(d) I display the strain on the $(10,10)$ nanotube wall containing C_{84} molecules. According to my results presented in Fig. 2.1, insertion of this large fullerene into the $(10,10)$ nanotube is energetically highly unfavorable. In this case, the fullerene is centered on the nanotube axis. Even in absence of an external force, the larger C_{84} molecules locally reduce the binding energy of atoms on the nanotube wall by as much as $\approx$50 meV. The resulting bulge on the wall is still very small, and preserves the cylindrical symmetry of the initial nanotube.

My results suggest two unusual applications of nanotube peapods. The first application is a possible way to separate nanotubes by diameter, due to the energetic preference of particular fullerenes to enter nanotubes within a narrow diameter range. All currently known synthesis techniques produce fullerenes and nanotubes in a wide diameter range. Whereas separation of fullerenes by isomer is possible using high-pressure liquid chromatography, there is no analogous technique allowing to separate nanotubes by diameter. Exposing nanotubes with a wide diameter distribution to a particular fullerene should lead to a preferential formation of peapods with an optimum nanotube diameter. The fact that nanotube peapods should have a higher gravimetric density than their empty nanotube counterparts could be utilized for a physical separation of peapods with a specific diameter from other nanotubes in a sample.

A second possible application is related to the high effective pressure inside the nanotube, caused by the motion of the encapsulated fullerenes. In view of the small nanotube cross-section, even forces in the nN range give rise to GPa pressures, suggesting a possible use of nanotubes as nanoscale autoclaves to facilitate chemical reactions. As a matter of fact, HRTEM observations of peapods subject to electron irradiation [47] or elevated temperatures [48] suggest a spontaneous fusion of fullerenes to long nanocapsules, in contrast to the more inert 2D and 3D fullerene structures [49, 50]. Also other molecules besides fullerenes, which can be encapsulated at an energy gain, should exhibit a similar behavior. As an example, selected diamondoid molecules [11] are expected to enter carbon nanotubes spontaneously [51]. Taking advantage of the physical confinement within the nanotube template, these diamondoids may fuse to one-dimensional diamond wires at nominal pressure.

2.2.4 Summary

In summary, I have studied the energetics and equilibrium packing geometry of fullerenes encapsulated in nanotubes. I found that each fullerene has an energetic preference for a narrow range of nanotube diameters for peapod formation. Resulting selective filling of particular nanotubes could be utilized to separate nanotubes according to diameter. Nanotubes, which are too narrow to encapsulate a particular fullerene, may still bind it at the open end and manipulate it, when attached to a Scanning Probe Microscope tip. We found that insertion of a fullerene inside an optimum nanotube host is associated with an energy gain of $\geq$0.4 eV. The "capillary" force produced by the entering fullerene may be augmented by an average force caused by inter-fullerene collisions at nonzero temperatures to a value in the nN range. In view of the small nanotube cross-section, this force should be equivalent to a pressure of the order of GPa. I find the observed reduction of the axial inter-fullerene distance to evidence this effective pressure. This large nominal pressure may become beneficial when using nanotube peapods as nanoscale pressure containers. The equilibrium packing geometry of smaller-than-optimum fullerenes inside nanotubes is a zig-zag arrangement, with an expected increase in the off-axis displacement with increasing pressure. The strain in the nanotube wall, associated with closely packed fullerenes, may locally modify the reactivity of the tube wall, which could be used for chemical functionalization.

2.3 Fullerene Fusion Mechanism

The following discussion on the equilibrium packing geometry of fullerenes and nanotube peapods follows that presented in Reference [52].

Combining total energy calculations with a search of phase space, I investigate the microscopic fusion mechanism of C_{60} fullerenes. I find that the $(2+2)$ cycloaddition reaction, a necessary precursor for fullerene fusion, may be accelerated inside a nanotube. Fusion occurs along the minimum energy path as a finite sequence of Stone-Wales transformations, determined by a graphical search program. Search of the phase space using the 'string method' indicates that Stone-Wales transformations are multi-step processes, and provides detailed information about the transition states and activation barriers associated with fusion.

2.3.1 Introduction

The discovery of fullerenes [32] and nanotubes [33] has ignited strong interest in these and related carbon nanostructures. Due to the unusual stability of the graphitic sp^2 bond, large-scale structural changes in bulk fullerene crystals occur only under extremely high pressures and temperatures [49, 50]. On the other hand, fullerenes in nanotube peapods [34] have been observed to fuse [47, 48] at relatively low temperatures near 1,100°C, significantly below the decomposition temperature of fullerenes [4] or graphite [53] near 4,000°C. No information is available about the detailed fusion process except the obvious conclusion that strong sp^2 bonds should not be broken during structural rearrangements leading to fusion. In view of the fact that even minor structural changes in carbon nanostructures may modify significantly their physical properties, including magnetism [54, 55], there is additional interest in understanding fusion as a way to control large-scale structural transformations.

Here I study the microscopic fusion mechanism of fullerenes. I show that large-scale structural changes, including fusion, can be achieved by a finite sequence of generalized Stone-Wales transformations, which involve only bond rotations and avoid bond breaking. Using a graphical search program, we determine the optimum reaction pathway for thermal fusion of fullerenes. Search of the phase space by the 'string method' provides detailed information about the optimum pathway, including the identification of activation barriers and transition-state geometries. I find the fusion process to be exothermic. The fusion dynamics is fast in spite of the formidable total activation barrier close to 5 eV, associated with each Stone-Wales transformation, since bond rotations turn out to be multi-step processes with lower individual activation barriers.

2.3.2 Microscopic Mechanism of Fullerene Fusion

The fusion of two C_{60} molecules to a C_{120} capsule, which has been observed in peapods [47, 48], is driven by the energy gain associated with reducing the local curvature in the system. Still, this reaction involves a large-scale morphological change and will only occur, if the required activation barrier is small.

A previous study [57], based on minimizing the classical action, suggests that the fusion reaction should involve multiple steps with relatively high activation barriers of $\approx$8 eV. This value may be considered an upper bound for the true activation barrier, since the authors had to guess the one-to-one atomic mapping between the initial and the final structure. Also, this study encountered computational limitations in the unconstrained search of a contiguous minimum-energy path in the 360-dimensional configurational space of the system.

It appears that the most likely fusion path may involve a sequence of bond rotations, called generalized Stone-Wales (GSW) transformations. GSW transformations are known to require much lower activation energies than processes involving bond breaking, and have been studied extensively in sp^2 bonded carbon structures [58]. A possible GSW pathway for fusion has been suggested based on a 'qualitative reasoning assisted search' for structures along the minimum-energy path [59]. The initial step in that study, however, is a reaction between two pentagons facing each other, which is energetically unaccessible.

In order to obtain microscopic insight into the fusion reaction, avoiding the above shortcomings, I investigated the optimum reaction path for the the $2C_{60}\rightarrow C_{120}$ fusion. It is well established that polymerization [60] and subsequent fusion [61, 62] of adjacent fullerenes starts by the $(2 + 2)$ cycloaddition reaction. This reaction, depicted as the $0\rightarrow 1$ transition in Fig. 2.4(a), requires two "double bonds", which connect adjacent hexagons in the C_{60} molecule, to face each other at the contact point of adjacent fullerenes.

With the $(2+2)$ cycloaddition reaction completed, we investigated the possibility to complete the $2C_{60}\rightarrow C_{120}$ fusion by generalized Stone-Wales transformations only. We searched all topologically possible pathways for the reaction with the aid of a graphical search program [56, 62]. Among these, I identified the shortest pathway, which is likely associated with the fastest fusion mechanism. This pathway involves only 23 GSW transformations and is depicted in Fig. 2.4(a). Tracing the atomic positions during this structural rearrangement, I found that the diffusion range of individual carbon atoms is limited to about three atomic bond lengths in the structure. Snapshots of intermediate state geometries along the optimum fusion pathway are shown in Fig. 2.4(b).

The energetics of the $2C_{60}\rightarrow C_{120}$ fusion process along the optimum path is depicted in Fig. 2.5(a). The energy results for the optimized metastable states of Fig. 2.4(a) are given by the data points. I conclude that the *ab initio* density functional and our parametrized total energy functional give consistent results for the relative energies of the intermediate states, and also for the large net energy gain of $\approx$13 eV associated with the fusion.

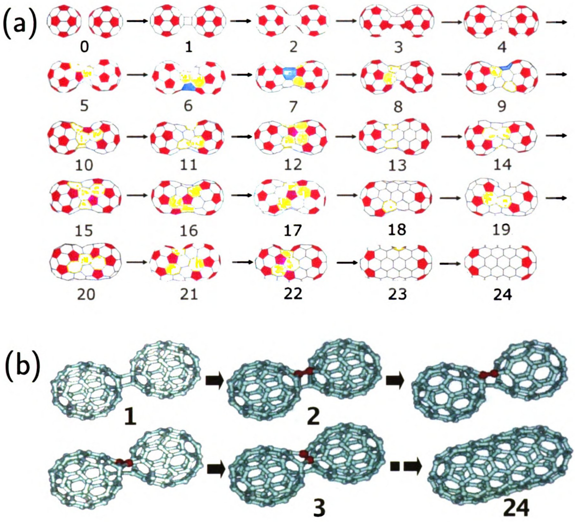

Figure 2.4: (a) Optimum pathway for the $2C_{60} \rightarrow C_{120}$ fusion reaction, involving the smallest number of generalized Stone-Wales bond rotations, determined by a graphical search of all possible bond rotation sequences. Polygons other than hexagons are emphasized by color and shading. (b) Snapshots of the optimized initial and final structures, and the metastable structures "2" and "3", depicted in (a). Also shown are two intermediate structures along the optimum fusion pathway between "2" and "3", resulting from the phase space search by the 'string method'. The bond involved in the 2→3 Stone-Wales transformation is emphasized by color. Images in this thesis dissertation are presented in color.

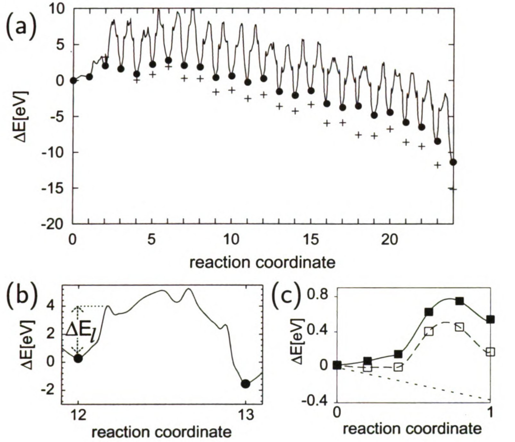

Figure 2.5: (a) Energy change along the optimum reaction path, given by the solid line. Energy results for the 25 intermediate structures, shown in Fig. 2.4, based on our total energy functional (•), are compared to *ab initio* Density Functional results (+). The contiguous minimum energy path in configurational space was identified using a 'string' technique. (b) Details of the energy change along the optimum path between structures "12" and "13" of Fig. 2.4, showing several local minima and implying a multi-step nature of this Stone-Wales transformation. The activation barrier limiting the reaction rate is denoted by ΔE_l. (c) Energetics of the $(2+2)$ cycloaddition reaction, corresponding to the 0→1 transition in Fig. 2.4(a), which is a necessary prerequisite for the fusion process.

To evaluate the reaction barriers of individual GSW transformations between the 24 intermediate states, we searched for the minimum energy path using the recently developed 'string' method [63]. This method represents the reaction pathway connecting the initial and final 120-atom geometry in the 360-dimensional atomic configuration space by a string line. In practice, the string is subdivided into finite segments of equal length, connecting structural replicas. The suitability of an energy path is determined by investigating the atomic force acting on each replica. Along the minimum energy path, the force component normal to the string must vanish. We employ $60 - 100$ replicas for each GSW step and relax the atomic positions, until the normal component of the atomic force becomes less than 0.05 eV/Å in magnitude.

Close inspection of the reaction energy along the contiguous optimum fusion path in Fig. 2.5(a) indicates a sequence of 23 activated processes connecting the 24 metastable states. I find the activation energy barriers $\Delta E_{GSW} \approx 5$ eV of these GSW transformations to be significantly lower than in graphite [64], as expected for Stone-Wales processes in non-planar structures due to the deviation from sp^2-bonding. In presence of extra carbon atoms, the activation barriers for GSW transformations may be lowered further to below 4 eV by autocatalytic reactions [65, 66]. Also, under electron irradiation, this process can proceed relatively fast in view of the high rate of sub-threshold energy transfer to the structure [67]. In extended fullerene systems, moreover, the energy release during the fusion process should heat up the structure locally, thus further promoting activated processes in the local vicinity.

Maybe the most significant finding of our study is the occurrence of multiple shallow local energy minima in the course of each GSW transformation. Details for the energy landscape, associated with the 12→13 reaction, are shown in Fig. 2.5(b). This implies that GSW transformations are multi-step rather than single-step [68] or two-step [69] processes, as postulated earlier. The local minima originate from local stress release during the bond rotation, which can be viewed as breaking of two C-C bonds at the same time as new bonds are being formed. The barriers separating these local minima are very small, suggesting a short lifetime with little effect on the overall reaction rate. I notice that GSW transformations are multi-step processes only in non-planar structures, as no such local minima occur during Stone-Wales transformations in a graphene layer due to the absence of tensile stress in that system.

Subdividing the GSW process into discrete steps with lower activation barriers $\Delta E_l < \Delta E_{GSW}$, shown in Fig. 2.5(b), also speeds up the transformation reaction. To estimate the overall reaction time at the temperature of $1,100°$C, where the onset of fusion has been observed [47, 48], I considered the fusion process as a sequence of 23 GSW transformations. Assuming the attempt frequency of 3×10^{13} Hz for the GSW transfomations [66] and a limiting activation barrier $\Delta E_l = 4.5$ eV in the Arrhenius formula [70], I find that the fusion reaction should be completed in 7 hours. Reduction of the activation barrier by 0.5 eV should reduce the total fusion time to 6 minutes. In view of the fact that fusion is generally more complex than an optimum sequence of GSW transformations, these values agree well with the observed fusion time of several hours [47, 48].

In spite of its lower activation barrier in comparison to the GSW steps, the initial $(2+2)$ cycloaddition reaction between the structures "0" and "1", the energetics of which is depicted in Fig. 2.5(c), may play an important role, and possibly even limit the rate of the fusion process. Fusion can only be initiated in the optimum geometry, where two double bonds in adjacent fullerenes face each other at the contact point. The probability of this configuration will multiply the attempt frequency ν of the $0 \rightarrow 1$ reaction in the Arrhenius formula [70] and thus reduce the reaction rate, since the low activation barrier of ≈ 0.7 eV only applies to attempts with the optimum fullerene orientation.

At low temperatures, polygons rather than double bonds should preferentially face each other in adjacent fullerenes, effectively preventing the fusion. Only at high enough temperatures, when unhindered fullerene rotation is activated [71], will the probability of double bonds facing each other increase, while each fullerene probes the configurational space. At that moment, the $(2+2)$ cycloaddition reaction should stop the rotation [72], and may initiate fusion.

To estimate the probability of the configuration required for the $(2+2)$ cycloaddition to occur, I first consider the phase space describing the motion of two rigid fullerenes at constant equilibrium distance (structure "0" in Fig. 2.4), which are freely rotating in space. The 8-dimensional configurational space, spanned by the three Euler angles defining the orientation of each fullerene and the two-dimensional vector defining the orientation of the inter-fullerene connection, is explored uniformly by the rotating fullerenes. Next, we assume that the difference between a "correct" and an "incorrect" fullerene alignment corresponds to a misorientation exceeding $\Delta\varphi \geq 1°$ in any dimension, which naturally introduces a grain size for the discretized configurational space.

In view of the fact that each fullerene has thirty double bonds, each of which can have two orientations, 3,600 out of 3×10^{19} cells in this space represent favorable configurations. Assuming that the configurational space exploration by the freely rotating fullerenes occurs at random in-between two cycloaddition attempts, separated by the period of the inter-fullerene vibration, the probability of finding an optimum configuration is $\approx 10^{-14}$. Using $\nu = 7\times10^{12}$ Hz for the inter-fullerene vibration frequency [42], the $(2+2)$ cycloaddition step with an activation barrier $\Delta E = 0.725$ eV should occur on the time scale of one week at $1,100$°C, significantly longer than the time frame of a GSW transformation. Thus, this step should be rate limiting in a close-packed three-dimensional C_{60} system, which – while molten at this temperature – could be prevented from evaporation by external pressure.

Restricting the configurational space to one dimension, which occurs when chains of fullerenes are packed in peapods, increases the fusion probability substantially. The crucial role played by the enclosing nanotube is to keep adjacent fullerenes in place long enough for them to probe the configurational space at close range. Since the vector connecting adjacent fullerenes coincides with the nanotube axis, the possibility of non-central collisions is eliminated, the dimensionality of the configurational space is reduced to six, and the number of discrete cells to only 5×10^{14}. This increases the probability of the optimum fullerene orientation by five orders of magnitude, and reduces the reaction time of the $(2 + 2)$ cycloaddition step to only 7 s at $1,100$°C. I conclude that fusion should occur more easily, when fullerenes are packed in peapods, than in three-dimensional bulk C_{60}.

In a three-dimensional C_{60} system, the fusion rate should further be reduced due to the fact, that more than one GSW transformation involving the same fullerene may occur simultaneously. Each C_{60} molecule has initially the ability to form at least four initial connections with neighboring fullerenes by the $(2 + 2)$ cycloaddition reaction [50]. Considering the finite size of the C_{60} molecule, GSW transformations associated with one fusion reaction are likely to interfere with transformation necessary for a separate fusion reaction, occurring concurrently. Due to resulting frustration, the activation barriers of individual GSW transformations could increase significantly, possibly even stopping the fusion. Since this effect is less severe in lower dimensions, the reduction of the overall fusion rate associated with concurring binary fusion reactions should be much less important in one-dimensional peapods than in bulk C_{60}.

2.3.3 Summary

In summary, I combined total energy calculations with a search of phase space to investigate the microscopic fusion mechanism of C_{60} fullerenes. I found that the $(2 + 2)$ cycloaddition reaction, a necessary precursor for fullerene fusion, may be accelerated inside a nanotube due to the reduced freedom of the system. Fusion should occur along the minimum energy path as a sequence of 23 generalized Stone-Wales transformations, determined by a graphical search program. These reactions can be viewed as bond-rotations, involving relatively low activation barriers. Our search of the phase space using the 'string method' indicates that Stone-Wales transformations are multi-step processes, and provides detailed information about the transition states and activation barriers associated with fusion.

2.4 Nanotube Fusion Mechanisms

The following discussion on the Nanotube Fusion Mechanisms follows that presented in Reference [73].

Here, I propose a new microscopic mechanism to explain the unusually efficient fusion process of carbon nanotubes. The model system under considerations, two adjacent (5,5) nanotubes that fuse into a (10,10) tube, is morphologically related to pants, with the narrow tubes representing the legs and the wider, fused tube segment the waist. I find a new pathway for the fusion process that involves a sequence of Stone-Wales type bond rearrangements rather than energy intensive bond breaking. The zipper-like mechanism of fusion I propose proceeds by increasing the waist at the expense of the leg segments, and is energetically favorable. I have probed all topologically possible reaction pathways through a graphic search program and identified transition states for each pathway using a novel technique. Corresponding atomic-level optimization and molecular dynamics simulations reveal that the energy barriers associated with the Stone-Wales transformations are very low, suggesting a fast fusion process. This finding is supported by time-resolved High-Resolution Transmission Electron Microscopy observations revealing the structural evolution of the system.

2.4.1 Introduction

Fullerenes [74] and nanotubes [75] are likely candidates for hierarchical self-assembly of nanoscale devices with complex geometries. As potential building blocks of nanotechnology, they are unusually stable and inert, suggesting that they should remain structurally stable once synthesized. Consequently, it remains an unsolved problem, why nanotubes and other sp^2-bonded carbon nanostructures are observed to fuse so efficiently [76, 77]. Especially puzzling appears the high speed of these structural transformations even at relatively low temperatures, implying a process with a very low activation barrier. A detailed understanding of this process may open a route to directing the assembly of more complex functional nanostructures.

Fusion pathways that have been discussed so far involve vacancy generation to establish a local connection between tubes and to propagate this connection as the tubes merge [76]. Yet the high energy cost associated with bond breaking is inconsistent with the high speed of the fusion process following the formation of the initial connection. Here, I propose a microscopic zipper mechanism that involves only bond rotations instead of bond breaking to speed up the merging process in partially fused tubes. Our findings offer a new insight into the observed fast coalescence of single-walled carbon nanotubes (SWNTs) under *in situ* irradiation and heating in a High-Resolution Transmission Electron Microscope (HRTEM) [76].

2.4.2 The Zipper Mechanism of Nanotube Fusion

The Y-junction structure used in our study of nanotube fusion, resembling the shape of pants, is shown in Fig. 2.6(a). This generic structure forms when, in presence of atomic defects, a local connection is established between adjacent nanotubes. The structure consists of a $(10,10)$ nanotube section representing the waist and two $(5,5)$ nanotubes representing the legs, and could be created by bond rearrangement during electron irradiation under experimental conditions. The bonding topology in the defective region, where the tubes are connected, is vacancy-free, which has never been considered before. The junction region shows negative Gaussian curvature. It contains higher polygons, including heptagons or octagons, inserted in the sp^2-bonded hexagonal network forming the tubes. In this work, I show that a continuous fusion process is possible in this geometry. In view of the instability associated with the insertion of high polygons, I focused on Y-junction geometries containing only heptagons and octagons in the hexagon network.

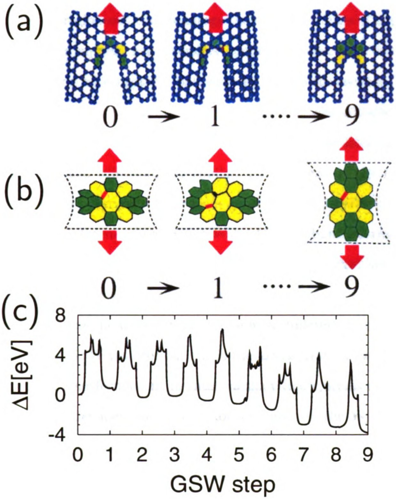

Figure 2.6: Front view (a) and structural diagrams detailing the bond switching (b), as two $(5,5)$ nanotubes merge to a $(10,10)$ nanotube in a morphology reminiscent of 'pants'. The fusion process requires nine generalized Stone-Wales (GSW) transformations to propagate the branching region axially by one period of the armchair nanotube without creating vacancies. Bonds, which are rotated during the individual GSW transformations, are emphasized by thick lines. Details of the complete process are presented at the URL `http://nanotube.msu.edu/ntyjct/`. The calculated total energy change ΔE along the minimal energy path connecting the intermediate steps is shown in (c).

Our main objective is to find out if it is possible to advance the axial position of the defect region and thus to merge the tubes by means of bond rearrangements only, similar to a zipper that reversibly connects or disconnects two pieces of fabric. In order to find all acceptable pathways leading to coalescence, a nontrivial topological problem, I use a graphical search program that was initially developed to study the fusion of fullerenes [78]. Since the initial steps of the local bridge formation between nanotubes and fullerenes are similar, I focus here on the major portion of the fusion process. Our search program generates all possible geometries, obtainable by a sequence of generalized Stone-Wales (GSW) bond rearrangements starting from one initial structure, and compares them to the target structure [78]. I restricted our search to GSW transformations [79], which were initially proposed as a general mechanism for the inter-conversion between fullerene isomers [80]. The main advantage of the GSW transformations is the low activation barrier, which accelerates the structural transformations in these vacancy-free systems during the zipper closure.

The zipper mechanism of nanotube fusion in the Y-junction geometry, containing one octagon and four heptagons in the junction region, is presented in Fig. 2.6. Figure 2.6(a) depicts one transformation cycle in front view. The detailed bond rearrangements are displayed in Fig. 2.6(b) as structural diagrams. Each GSW step within the transformation cycle is identified by a rotation of a single bond near the junction of two $(5,5)$ nanotubes. I emphasize the respective bonds by a thick red line prior and a thick black line after the rotation. Our results show that a sequence of only nine sequential GSW transformations is sufficient to propagate the connecting region by one step and thus increase the waist section axially by one period of the $(10,10)$ nanotube, at the expense of the leg section. In an alternative geometry not discussed here, which contains six heptagons and no higher polygons in the junction region, the axial propagation of the junction by one period can be achieved by only twelve sequential GSW transformations. Following such a full transformation cycle, the final structure ('9') is topologically equivalent to the initial structure ('0'). A related structural transformation, which involves an energetically unstable twelve-membered ring in the junction region, has also been found to provide a pathway to nanotube fusion [81]. There, the GSW sequence has been determined using a 'qualitative reasoning assisted search' instead of a computer-assisted complete search. The energetics of the optimized fusion process discussed here, depicted in the Fig. 2.6(c), suggest a monotonic stability increase upon each GSW transformation, in stark contrast to the findings of Ref. [81].

As seen in Fig. 2.6(c), the fusion process is exothermic. Based on strain energies of infinite structures, I expect an energy gain of 4.8 eV by converting two 0.21 nm long $(5,5)$ nanotube segments to a $(10,10)$ nanotube within one transformation cycle [82]. Total energy calculations for the intermediate structures i, encountered during the fusion process and shown in Fig. 2.6(c), are performed using the parameterized linear combination of atomic orbitals functional [83] for an $N = 364$-atom cluster representing the structure. All intermediate structures of the system have been fully relaxed using the conjugate gradient technique [84]. Our cluster calculation indicates that the energy is lowered by 4 eV during the complete 9-step transformation cycle, in good agreement with the above 4.8 eV value in view of the finite size of the cluster.

To evaluate the reaction barriers associated with each individual GSW transformation, which play a crucial role in the reaction rate of the zipping process and have not been investigated in Ref. [81], I determine the minimum energy path in the configuration space using the so-called "string method" [85]. In the string method, the reaction pathway connecting the initial and final N-atom configuration is represented by a string line in the $3N$-dimensional configuration space. In practice, the string is discretized into a sequence of replicas with the constraint of equal arc length between them. The minimum energy path is found, when the atomic force of every replica along the string is parallel to the tangent of the string. I employ 50 replicas for each

GSW step and relax the atomic positions until the normal component of the atomic force becomes less than 0.05 eV/Å in magnitude.

The details of the reaction energy ΔE along the contiguous minimum-energy path, corresponding to the zipper process, are depicted in Fig. 2.6(c). These results suggest that most GSW transformations are multi-step processes with well-defined transition states, as discussed below. I find the maximum energy barrier for a single GSW step to lie near $5 - 6$ eV. As I discuss in the following, this activated process can proceed relatively fast under the experimental conditions in view of the high rate of sub-threshold energy transfer to the structure during electron irradiation [86]. Alternatively, the activation barrier for GSW transformations may be lowered to below 4 eV by autocatalysis reactions [87] involving extra carbon or nitrogen atoms [88]. The $5 - 6$ eV activation energy for the GSW transformation in the Y-junction system lies significantly below the graphene sheet value of $\approx$9 eV based on our approach, or $\approx$8 eV based on *ab initio* calculations [89]. Such a lowering of the activation barrier is expected in non-planar structures due to the deviation from sp^2-bonding. I find this hypothesis confirmed in our calculations, since lower barriers are found when more heptagons or octagons are closer to the rotating bond.

As mentioned above, I find that most Stone-Wales transformations involve multiple shallow local energy minima, implying a multi-step process. These minima originate from local stress release, as two C-C bonds are being broken at the same time as other bonds are being formed during the bond rotation. The barriers surrounding these local minima are very small, suggesting a short lifetime with little effect on the overall reaction rate. In contrast to these findings in the nanotube Y-junction, no such local minima occur during the Stone-Wales transformation in graphite due to the absence of tensile stress in that system.

To investigate the effect of high temperatures on the activated fusion process and to identify a possible mechanism that would lower the activation barriers even further, I performed Nosé-Hoover molecular dynamics (MD) calculations at temperatures between 400 K and 2400 K. The upper limit of this temperature range is determined by the onset of melting at 2800 K, which starts at the exposed edges of the finite Y-junction or 'pants' structure. With increasing temperature, particular vibration modes are stepwise activated. Below 400 K, I observe only local atomic vibrations without global shape changes of the structure. At 800 K, a radial breathing mode of the tubes dominates the dynamics. At 1200 K, the 'legs' of the pants structure exhibit a vibration mode, reminiscent of walking and twisting. At 1600 K, this 'walking' mode is replaced by a 'scissor' mode of the legs, which strains the junction region and lowers the activation barrier for GSW transformations [90]. Snap shots of our molecular dynamics simulation at 1200 K are shown in Fig. 2.7(a-c).

To obtain independent experimental information about the fusion mechanism, we observed the structural evolution of the nanotube system in an HRTEM. The SWNT samples were generated using either an arc discharge technique involving Ni-Y-graphite electrodes in a He atmosphere [91], or the HiPco (High-Pressure CO conversion) process involving the disproportionation of carbon monoxide over an Fe catalyst [92]. The nanotube material was dispersed ultrasonically in ethanol and deposited onto lacey carbon grids for TEM observations. The experiments were carried out in a high-voltage Atomic Resolution Transmission Electron Microscope with an accelerating voltage of 1.25 MeV (JEOL-ARM 1250, located at the MPI Stuttgart). Observations were performed at specimen temperatures of 800°C using a Gatan heating stage. Images were recorded with a slow-scan CCD camera. The nanotube behavior was monitored under the electron irradiation corresponding to standard imaging conditions (1.25 MeV electron energy and beam intensity of $\approx$10 A/cm^2).

The time sequence of HRTEM observations in Fig. 2.7(d-g) provides information about the stability of the nanotube Y-junction with respect to electron irradiation and high temperatures. As discussed above, our MD simulations shown Fig. 2.7(a-

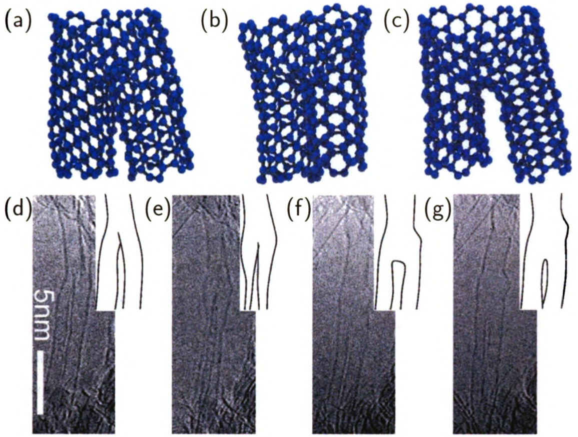

Figure 2.7: (a-c) Snap shots of nanotube 'pants' structures, obtained during a molecular dynamics simulation at $T = 1200$ K, illustrating the excitation of soft vibration modes resembling a 'walking' motion. The corresponding movies are posted at the URL `http://nanotube.msu.edu/ntyjct/`. (d-g) Time sequence of HRTEM images of partially merged SWNTs, where the fusion process was interrupted by an impurity or a chirality difference between the constituent tubes. (d) Initial structure, involving two tubes of similar diameter in close proximity. (e) In spite of electron irradiation for five minutes, the tubes ('legs' of the 'pants') stopped merging, but rather collapsed into a ribbon while being twisted. (f) A few minutes later, a region with negative Gaussian curvature, involving heptagons or other higher polygons, becomes visible between the 'legs', as the merging continues and the whole system rotates. (g) Two minutes later, the tubules start merging from the bottom, with little change to the previous zipper closure. No further changes occur during the remaining observation time, indicating that the fusion process slows down and stops. The white scale bar is 5 nm long.

c) suggest the occurrence of 'walking' and 'twisting' modes close to 1200 K, the temperature used in the HRTEM observations of Fig. 2.7(d-g). Figure 2.7(d) depicts the initial local connection between the tubules, yielding the Y-junction. In spite of a subsequent five-minute exposure to electron irradiation, the overall structure appears stable and the shape of the nanotube branches remains essentially the same. The only noticeable change is an overall rotation and twisting of the structure about the axis, as seen in Fig. 2.7(e). Figure 2.7(f) provides an optimum view of the junction region, where heptagons and octagons induce a negative Gaussian curvature. During the following three minutes of irradiation, the fusion process continues, but slows down and eventually stops, as shown in Fig. 2.7(g).

The termination of the fusion process might be due to impurities. Another possible reason is a chirality mismatch of the tube 'legs', or the torsion energy required to fuse initially twisted legs, which may be firmly anchored in the substrate. Conceptually, I can imagine one of initially straight tube segments of length L to be cut out first, then twisted by the angle $\Delta\Phi$, and seamlessly reinserted. The resulting average twist of $\Delta\Phi/L$ in the segment comes at a cost in the total torsion energy that is inversely proportional to L. As the constituent tubes continue to merge, thus reducing L while approaching the anchor point, the total strain energy in the twisted tube increases [93]. Independent of the tube stiffness or the initial twist $\Delta\Phi/L$, the strain energy eventually outweighs the energy gain caused by tube fusion. At this point, the fusion process turns endothermic and stops.

In order to study whether nanotubes may merge completely via the zipper mechanism, I have examined two adjacent tubes lying in a plane under electron irradiation at 800°C. Figure 2.8(a-c) shows a sequence of the zipping process in the 'pants' geometry. In Fig. 2.8(a) we can distinguish two nanotubes, lying close and parallel to each other. Few minutes later, the tubes were observed to approach even more and started overlapping, as seen in Fig. 2.8(b). Subsequently, the nanotubes formed a local connection and started merging fast. Figure 2.8(c) depicts the final stage of this process, a single wide nanotube. The observed fusion process of two tubes into one tubule with a larger diameter, including the intermediate stages and the speed of interconversion, is consistent with our zipper mechanism.

2.4.3 Summary

In summary, I introduced a microscopic mechanism to explain the efficient and fast fusion process of two adjacent nanotubes in the Y-junction geometry, reminiscent of pants. I found the fusion process, which proceeds by increasing the waist at the expense of the leg section, to be energetically favorable. I proposed a microscopic zipper mechanism that consists of a sequence of Generalized Stone-Wales transformations corresponding to bond rotations. In two representative pathways, distinguished by the local bonding geometry in the junction region, only nine or twelve bond rotations are needed to complete a full transformation cycle. I investigated the detailed energetics of the zipper process, including the transition states, using the string technique. Our atomic-level optimization calculations and molecular dynamics simulations reveal that the energy barriers associated with the Stone-Wales transformations are low, consistent with a fast fusion process. The suggested propagation of the zipper-like motion and the vibration modes of the nanotube 'pants' were observed in a time sequence of transmission electron micrographs.

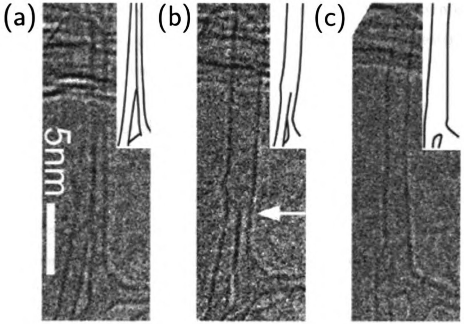

Figure 2.8: (a) Tubes prior to coalescence at 800°C. (b) As electron irradiation continues, the nanotubes get closer, overlap, and start merging into one. The fused region is emphasized by the white arrow. (c) The coalescence process is completed, as the fusion region moves down, completing the zipper closure. The white scale bar is 5 nm long.

2.5 Diamondoids as Building Blocks of Functional Nanostructures

The following discussion on the diamondoids as building blocks of functional nanostructures follows that presented in Reference [51].

We investigate the equilibrium structure, stability, and electronic properties of nanostructured, hydrogen terminated diamond fragments. The equilibrium atomic arrangement and electronic structure of these nanostructures turn out to be very similar to bulk diamond. We find that such diamondoids may enter spontaneously into carbon nanotubes.

2.5.1 Introduction

In his inspiring presentation entitled "There is Plenty of Room at the Bottom" [94] in 1959, Richard Feynman pointed out the untapped potential of functional nanostructures, assembled with atomic precision, to influence our every-day life. In the meantime, technological progress has been associated with a continuous drive towards miniaturization. Recent progress in nano-scale electromechanical systems (NEMS) suggests that complex functional nanostructures, invisible to the naked human eye, may soon follow suit.[95] Large-scale production of such complex nanostructures is likely to occur by hierarchical self-assembly from well-defined structural building blocks, [96, 97] which can be thought of as "nano-LEGO". To fulfill their mission, such nanostructures must be strong and chemically inert in their environment.

Carbon fullerenes [32] and nanotubes [33] have emerged as promising candidates for such building blocks, providing a variety of functionalities. Here, we investigate a new class of carbon nanostructures, the diamondoids. These nanoscale building blocks are very different, but compare well in stability and light weight with fullerenes and nanotubes. Beings essentially hydrogen-terminated nanosized diamond fragments,

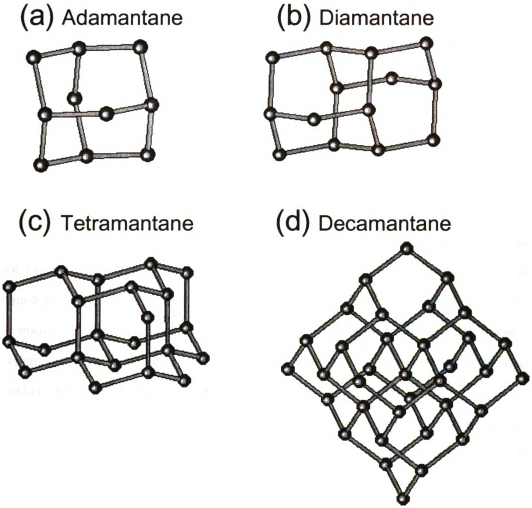

Figure 2.9: Hydrogen atoms, terminating the carbon skeleton, are omitted from the diagrams for clarity. (a) The smallest diamondoid, adamantane, consisting of a single diamond cage. (b) Diamantane with two diamond cages. (c) Tetramantane with four diamond cages. (d) Decamantane with ten diamond cages.

they may occur in a large variety of shapes, as shown in Fig. 2.9. The smallest possible diamondoid is adamantane, [98] consisting of ten carbon atoms arranged as a single diamond cage, [99] surrounded by sixteen hydrogen atoms, as shown in Fig. 2.9(a). Larger diamondoids [100, 101, 102] are created by connecting more diamond cages and are categorized according to the number of diamond cages they contain. The diamondoids shown in Fig. 2.9 contain up to tens of carbon atoms and are only a few nanometers in diameter.

Traditionally, diamondoids have been known in the oil industry, [103, 104] where they occur naturally dissolved in oil and its distilled by-products. At low temperatures and low pressures, diamondoids may precipitate from the solution and act as nucleation sites for the formation of sludge, which often blocks pipelines [105, 106]. Only recently, isomerically pure diamondoids with up to eleven adamantane cages have been extracted from the sludge [11] and are now being considered for nanotechnology applications. The isolated diamondoids occur in very different shapes, and many of them form molecular crystals. These uncommon organic molecules can be chemically functionalized, by substituting carbon or hydrogen atoms at the surface by other atoms or groups, to promote formation of specific polymers.

Given that diamondoids are essentially hydrogen terminated diamond fragments, we anticipate that in absence of significant structural changes, they share the toughness and insulating properties with their bulk diamond counterpart. Our study confirms this anticipation. In the following, we carry out a theoretical investigation of diamondoids using *ab initio* density functional calculations. We determine their equilibrium geometry, in particular the dependence of the bond lengths and bond angles on the system size, and their electronic density of states (DOS).

Beyond identifying the properties of unmodified isolated diamondoids, we also explore ways to manipulate them and to connect them together. We find that the interaction between unmodified diamondoids is too weak and does not favor polymerization to larger structures. Hence, we explore the possibility of creating specific binding sites by atomic substitution. We then explore the interaction between unmodified and functionalized diamondoids. In particular cases, we conclude, a nanotube attached to the tip of a Scanning Probe Microscope could also be used to manipulate diamondoids into position on a substrate, similar to the way this was achieved for adsorbed rare gas atoms [43].

Even more intriguing is the possibility to use a nanotube as a container for unmodified and functionalized diamondoids, very much the same it acts for fullerenes [34] and polymers [107]. The nanotube surrounding the encapsulated diamondoids may act as a template to connect these molecules in a well-defined way. In particular, we could envisage the polymerization of quasi-linear polymantanes to an infinite diamondoid wire, enclosed in a nanotube.

2.5.2 Properties of Isolated Diamondoids

Our calculations are based on the *ab initio* density functional theory (DFT) within the local density approximation (LDA). We use Troullier-Martins pseudopotentials to describe the effect of atomic nuclei plus core electrons on the valence electrons, and the Perdew-Zunger parametrized exchange-correlation potential, as implemented in the SIESTA code [9]. We used a double-zeta basis [108], augmented by ghost orbitals, and 50 Ry as energy cutoff in plane-wave expansions of the electron density and potential, which is sufficient to achieve a total energy convergence of $\leq$1 meV per atom during the self-consistency iterations.

We performed a full optimization of diamondoid structures C_nH_m containing up to ten diamond cages. Our optimized geometries, some of which are reproduced in Fig. 2.9, are in good agreement with those inferred experimentally [10, 11] and theoretically [12, 13]. Also, the equilibrium C-C bond length of 1.540 Å in the optimized bulk diamond structure was found to agree with the experimental value [109]. Constrained

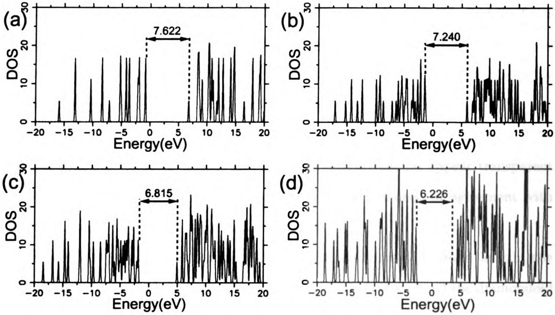

Figure 2.10: Electronic structure of an (a) adamantane, (b) diamantane, (c) tetramantane, and (d) decamantane, depicted in Fig. 2.9. $E = 0$ corresponds to the Fermi level. The fundamental band gaps are indicated in eV.

geometries were used when determining the interaction between diamondoids [110].

The lower diamondoids we considered here include adamantane, diamantane, triamantane, all four isomers of tetramantane, all nine isomers of pentamantane with a molecular weight of 344 a.m.u., six isomers of hexamantane, two isomers of heptamantane and one isomer each of octamantane, nonamantane and decamantane. With increasing adamantane size, the number of isomers increases geometrically, making an exhaustive study of all isomers impractical[11]. In our selection of isomers, we focused on those identified experimentally in Ref. [11]. For each of these diamondoids, we have determined the equilibrium structure, the binding energy per carbon atom, and the electronic DOS.

The electronic density of states of the diamondoids presented in Fig. 2.9 is shown in Fig. 2.10. The spectrum consists of discrete eigenvalues associated with the finite size of the molecules. With increasing size, the gap between the Highest Occupied Molecular Orbital (HOMO) and the Lowest Unoccupied Molecular Orbital (LUMO) will converge to the fundamental gap of diamond as the bulk counterpart of the finite molecules. In comparison to other atomic clusters, we find the HOMO-LUMO gap to lie very close to that of bulk diamond even for the smallest diamondoids, including adamantane, as shown in Fig. 2.11(a). In conjunction with the fact that LDA usually underestimates the HOMO-LUMO gap, its large value of several electron-volts suggests that diamondoids–similar to bulk diamond[111]–should appear transparent in visible light, and act as electrical insulators. This is indeed in agreement with observations in diamondoid-based molecular crystals.[11]

Figure 2.11 summarizes our results for the equilibrium C-C bond length, the HOMO-LUMO gap, and the formation energy per carbon atom in all the diamondoid isomers we have considered. The equilibrium C-C bond lengths in the diamondoids, depicted in Fig. 2.11(b), lie very close to the value found in bulk diamond. Since also the bond angles in these structures lie close to those found in diamond, we conclude that even the smallest diamondoids show sp^3 type bonding, which is very different from graphite-like sp^2 bonding found in fullerenes and nanotubes. Only in the smaller diamondoids, including adamantane, diamantane and triamantane, the C-C bond length is somewhat smaller than in bulk diamond, reflecting the small difference between the C-H and the C-C(sp^3) bond in hydrogen-terminated carbon atoms. The error bars shown reflect mainly the differences between the inequivalent sites in the lower diamondoids, and an estimated uncertainty resulting from our optimization procedure in the larger structures. In agreement with related theoretical studies,[12, 13] we find the hydrogen-terminated small diamondoids, investigated here, stable with respect to hydrogen desorption and surface reconstruction.

The structural resemblance between even the smaller diamondoids and diamond suggests that these nanostructures will also share the desirable toughness and insulating properties with bulk diamond. The latter is indeed the case, as suggested by the large HOMO-LUMO gap we find in all the diamondoids investigated here, shown

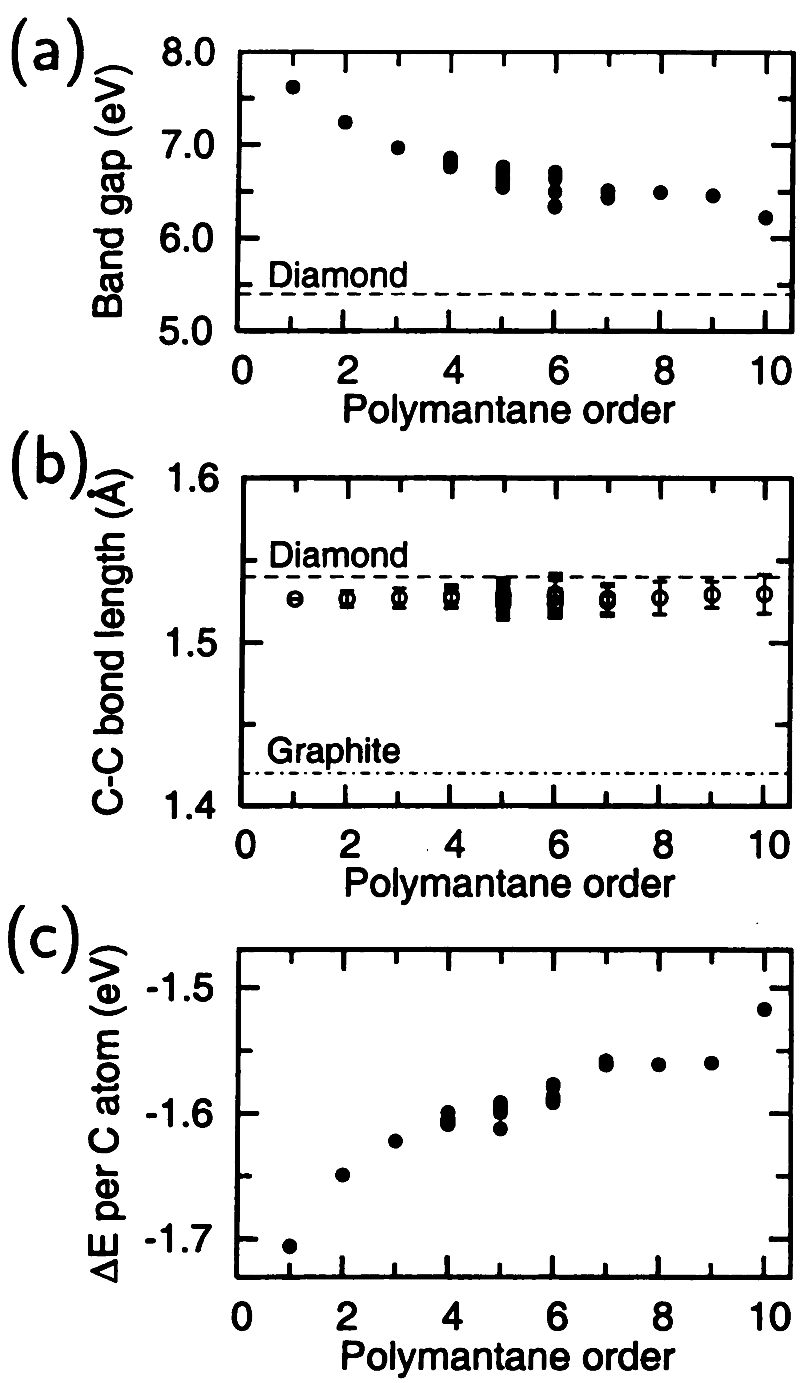

Figure 2.11: (a) HOMO-LUMO gaps in the density of states (DOS). (b) C-C bond lengths, with the error bar reflecting the spread of the values within each system. (c) Formation energy per carbon atom $\Delta E/n$ of the C_nH_m diamondoids.

in Fig. 2.11(a). In agreement with former studies,[12, 13] we find the HOMO-LUMO gap to decrease monotonically with increasing diamondoid size. Among the different isomers of a particular polymantane, we can observe a subtle trend, which correlates the more elongated structures with somewhat larger HOMO-LUMO gaps than more compact structures.

Figure 2.11(c) shows the formation energy per carbon atom $\Delta E/n$ of the C_nH_m diamondoids as a function of the diamondoid size. We define the formation energy by $\Delta E/n(C_nH_m)= [E_{tot}(C_nH_m)-nE_{tot}(C)-(m/2)E_{tot}(H_2)]/n$, where $E_{tot}(C)$ is the total energy of diamond per atom, and $E_{tot}(H_2)$ is the total energy of a hydrogen molecule.[112]

According to Fig. 2.11(c), we find all diamondoids, as well as bulk diamond, overbound due to underestimating the total energy of isolated atoms, a well-documented shortcoming of LDA. As suggested by the results in Fig. 2.11(c), the stability of the lower polymantanes is inferior to bulk diamond, since a significant fraction of carbon atoms is connected to fewer than four carbon neighbors. An intriguing observation is that the stability is nearly independent of the stacking arrangement of adamantane cages, suggesting an isomer-independent binding energy. With increasing size, we observe a monotonic increase in stability towards the bulk diamond value.

The properties of an elongated hexamantane isomer, and an infinite diamondoid chain as its quasi-1D crystalline counterpart, are discussed in Fig. 2.12. Such structural elements could find use in NEMS devices and, as we discuss in the following sections, could be self-assembled inside carbon nanotubes. Figures 2.12(a) and (d) show the close structural relationship between the finite molecule and the infinite chain, obtained by periodically repeating the unit cell shown in Fig. 2.12(d). The average C-C bond length in the infinite diamondoid chain is 1.530±0.008 Å, close to the values found for the other diamondoids, given in Fig. 2.11(b).

The electronic density of states of hexamantane is shown in Fig. 2.12(b). In all

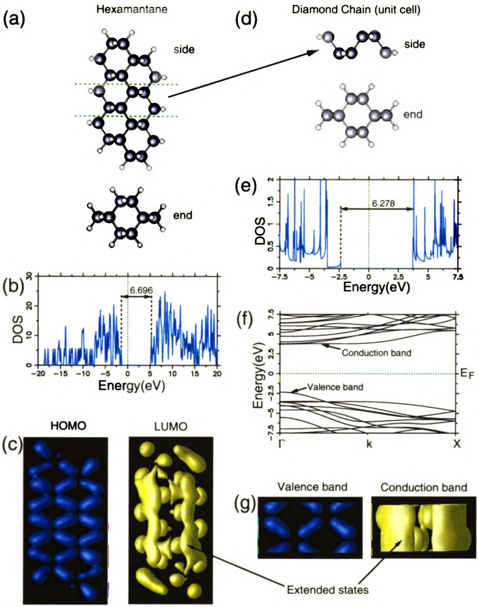

Figure 2.12: Comparison between structural and electronic properties of an elongated hexamantane isomer (left panels) and an infinite diamondoid chain (right panels). The equilibrium structure is shown in (a) and (d), with the large spheres denoting carbon and the small spheres hydrogen atoms. The electronic density of states is presented in (b) and (e), with the Fermi level at $E = 0$. The one-dimensional band structure of the infinite diamondoid chain is shown in (f). The charge distribution of electrons in the highest occupied molecular orbital (HOMO) and the lowest unoccupied molecular orbital (LUMO) of hexamantane is shown in (c). The corresponding charge distribution in the top valence and bottom conduction band of the diamondoid chain is shown in (g).

respects, including its large HOMO-LUMO gap, this DOS lies close to the results found in the other diamondoids, depicted in Fig. 2.10. The electronic spectrum of the infinite quasi-1D counterpart of hexamantane, shown in Fig. 2.12(e), is similar to that of hexamantane, and dominated by a series of van Hove singularities in the valence and conduction region. The dense sequence of these singularities reflects the dense spectrum of relatively flat bands, depicted in Fig. 2.12(f), which makes this system a wide-gap insulator with an indirect gap. In view of the negative electron affinity of diamond,[113] combined with a large length-to-diameter aspect ratio, diamondoid chains may even surpass carbon nanotubes in applications such as cold cathodes or low-voltage electron emitters in flat panel displays.

In spite of its wide fundamental gap, the infinite diamondoid chain could possibly acquire conductivity by electron or hole doping. Close inspection of the electronic dispersion relations in Fig. 2.12(f) reveals that the bands close to the Fermi level show an energy dispersion of below 2 eV. To investigate the charge delocalization as a pre-requisite for conduction, we display the charge distribution of the topmost valence and bottom conduction band in Fig. 2.12(g), and compare it to that of the HOMO and LUMO of hexamantane in Fig. 2.12(c).

Results for the infinite chain suggest that the charge associated with the valence band is localized in pockets near inter-atomic bonds, thus hindering hole transport. This charge distribution is very similar to that of the HOMO of hexamantane. The conduction band, on the other hand, consists of four strongly delocalized states located on the outer perimeter of the structure, which could be used to conduct electrons. These extended conduction states find their counterpart in the LUMO of hexamantane, which is similarly delocalized across the middle section of this molecule. The bottom of the conduction band is very flat, suggesting that electrons in a lightly electron-doped system should have a low mobility.

Due to the wide fundamental gap, chemical doping is unlikely to provide free carriers, since it would require introduction of impurities with a very low ionization potential, likely to introduce trap sites. One possibility of electron doping would involve gating a supported diamondoid chain. A more likely scenario of n-doping would involve enclosing the diamondoid chain inside a carbon nanotube, as discussed below, and n-doping the surrounding nanotube.

2.5.3 Interaction of Diamondoids with Carbon Nanotubes

Since the cross-section of carbon nanotubes is compatible with the size of diamondoids, nanotubes could be used to manipulate and assemble these molecules to larger structures. Precise deposition and positioning of diamondoids could be achieved with the help of a carbon nanotube attached to the tip of a Scanning Probe Microscope (SPM),[43, 44] which may combine its functionality as a storage, deposition, and manipulation device. Combination of diamondoids with nanotubes may, moreover, lead to functional nanostructures for particular applications. Key to all these applications is to understand the interaction of diamondoids with carbon nanotubes.

In the following, we describe the interaction of diamantane as a prototype diamondoid with (n, n) armchair carbon nanotubes of different diameter. Aspects of particular interest to us are the energy change associated with the entry of a diamondoid inside a nanotube, and the optimum nanotube diameter to maximize the encapsulation energy.

Our results for the entry of diamantane into armchair carbon nanotubes ranging from $(4, 4)$ to $(7, 7)$ are presented in Fig. 2.13. Due to computer limitations, we considered finite length nanotube segments, which have been hydrogen terminated at both ends. The encapsulation geometry is depicted in end-on and side view in the left panels of Fig. 2.13. The dependence of the diamantane-nanotube interaction energy on the diamantane position z along the tube axis is presented in the right panels of Fig. 2.13.

(a) (4,4) nanotube

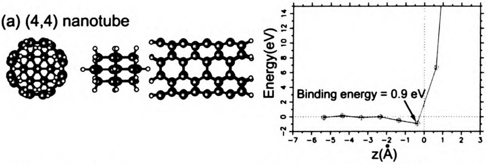

(b) (5,5) nanotube

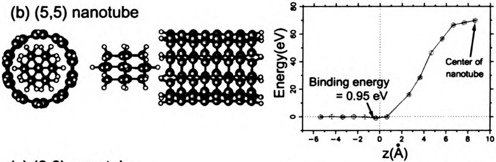

(c) (6,6) nanotube

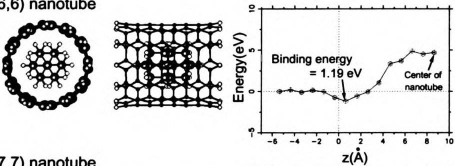

(d) (7,7) nanotube

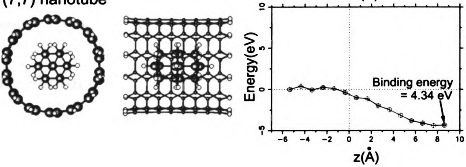

Figure 2.13: The end-on and side view of the insertion geometry is depicted in the left panels. The axial separation between the closest end of the diamantane and the nanotube is denoted by z, with $z < 0$ corresponding to the diamantane outside and $z > 0$ to the diamantane inside the carbon nanotube.

These energy results suggest that entry of diamantane into a $(4,4)$, $(5,5)$ and $(6,6)$ nanotube is energetically unfavorable. Nevertheless, the dip in the total energy at $z{\approx}0$ suggests the possibility of attaching this molecule to the hydrogen terminated nanotube end, and thus a possibility of manipulating diamondoids with a nanotube attached to an SPM tip.

As seen in Fig. 2.13, only (n,n) nanotubes with $n{\geq}7$ are wide enough to accommodate diamantane endohedrally without energy investment. The energy of diamantane encapsulated inside wider (n,n) nanotubes is shown in Fig. 2.14 as a function of its off-axis displacement y. We find that the $(7,7)$ nanotube has an ideal diameter to contain a single diamantane with optimal encapsulation energy. Containment in the $(6,6)$ nanotube is moderately endothermic. Containment in the $(8,8)$ nanotube is exothermic, but the minimum in the energy curve is rather flat, suggesting that the diamondoid would have some degree of lateral freedom and that the $(8,8)$ nanotube is too wide. Nevertheless, the enclosing nanotube should suppress free rotation of the diamondoid, thus facilitating specific reactions. Results very similar to those for diamantane are also expected for all higher, linear diamondoids, as well as the diamond chain, addressed in Fig. 2.12. The encapsulation of the smaller adamantane should proceed very similar to that of diamantane, with the exception that orientational alignment of adamantane with no obvious "long" axis cannot be achieved.

2.5.4 Summary

In summary, we performed *ab initio* density functional calculations to study structural and electronic properties of unmodified and chemically functionalized polymantanes, as well as their reactivity and interaction with carbon nanotubes. Our results support the conjecture that the lower polymantanes are essentially hydrogen terminated diamond fragments with diamond-like properties. Hence, these systems may be used as molecular building blocks of complex functional nanostructures, to be

(a) (6,6) nanotube

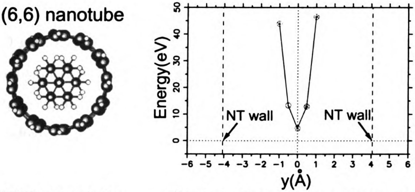

(b) (7,7) nanotube

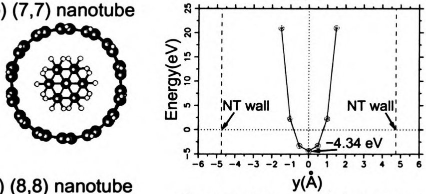

(c) (8,8) nanotube

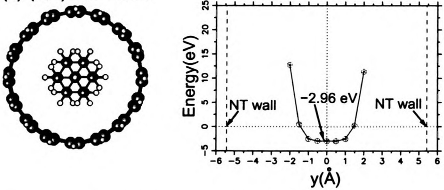

Figure 2.14: Energetics of diamantane, enclosed inside a (6, 6), (7, 7), and (8, 8) carbon nanotube, as a function of an off-axis displacement y. The geometry in end-on view is shown in the left panels.

found in future NEMS devices. Within computational uncertainty, we find the bond lengths and angles in the carbon skeletal structure of the diamondoids essentially the same as in bulk diamond. Similarity in bonding between diamondoids and diamond extends also to bond strength and resistance to deformations. The large HOMO-LUMO gaps in diamondoids are the molecular counterpart of a large fundamantal gap in diamond, which is responsible for its optical transparency in the visible range and its insulating properties. We also find the properties of hydrogen-terminated diamondoids to approach those of bulk diamond, as their size increases.

Unmodified diamondoids are non-reactive and interact only weakly with each other. We found, however, that substituting carbon by boron and nitrogen atoms may create localized binding sites in these modified diamondoids, and provide the possibility of connecting diamondoids by much stronger, directional bonds. Selective substitution at more than one carbon site per diamondoid may provide the possibility to connect even larger diamondoids into well-defined nanostructures for particular applications.

We have found that diamondoids should enter spontaneously into carbon nanotubes with a wide enough diameter, similar to the spontaneous encapsulation of fullerenes, leading to peapods.[34] Being orientationally constrained in these nano-sized containers, they may fuse into long structures, including a "diamond wire". Carbon nanotubes can be used not only to store diamondoids, but also to manipulate them sterically, preferably in conjunction with a Scanning Probe Microscope. Even nanotubes that are too narrow to contain a diamondoid may be used for such a purpose, since diamondoids preferentially bind to the reactive open end of a nanotube, which may be attached to the tip of a Scanning Probe Microscope.

Chapter 3

Structural Transitions in Ferrofluid Systems

3.1 Introduction

Complex fluids, consisting of a colloidal suspension of particles carrying electric or magnetic dipole moments [116], are intriguing systems with a wide range of technological applications [117]. Finite dipole aggregates are expected to display a plethora of nontrivial equilibrium structures due to the competition between the strongly anisotropic dipole-dipole interaction, favoring open structures, and isotropic inter-particle forces as well as surface tension, which favor compact structures. In ferrofluids, consisting of a colloidal suspension of magnetite particles, reported observations range from compact and branched macroscopic structures [118] to complex labyrinthine patterns [119, 120]. Similar, but less complex structures have been observed in electro-rheological fluids, where the electric dipoles are induced by inter-particle interactions [124].

Except for aggregates with few particles [125, 126], structural studies of complex fluids have focused on pattern formation in systems with infinitely many particles.

Here I present results in the interesting finite-size regime, where the surface tension of the aggregate plays a dominating role in its equilibrium structure. We find that with increasing number of particles, as the role of the surface diminishes, the structural motif evolves from chains and rings to multi-chain and multi-ring assemblies, single- and multi-wall coils, tubes and scrolls. I map the inter-particle interactions in the colloidal suspension onto a continuum model and show how changes in external parameters, such as external magnetic field or the liquid-particle interaction, affect the relative stability of these structures and induce structural transitions.

To gain microscopic insight into the causes of pattern formation in ferrofluids, which is beyond the scope of present experimental observations [118, 120], I perform total energy and structure optimization calculations for finite aggregates of magnetic particles suspended in a viscous liquid. Our model system is designed to represent a typical ferrofluid that contains magnetite particles, which are covered with surfactants such as oleic acid, which cause short-range entropic inter-particle repulsion to keep the particles in suspension and to prevent a structural collapse. Not only the dynamics of the ferrofluid, but also the effective inter-particle interaction is affected by the viscous liquid used in the colloidal suspension, which is usually n-eicosane or kerosene.

3.2 Equilibrium Structure of Ferrofluid Aggregates

The following discussion on the Equilibrium Structure of Ferrofluid Aggregates follows that presented in Reference [121].

I study the equilibrium structure of large but finite aggregates of magnetic dipoles, modeling a colloidal suspension of magnetite particles in a ferrofluid. With increasing system size, the structural motif evolves from chains and rings to multichain and multi-ring assemblies. Very large systems form single- and multi-wall coils, tubes and scrolls. These structural changes result from a competition between various energy terms, which can be described analytically within a continuum approximation. I also study the effect of external parameters on the relative stability of these structures.

The potential energy U_{tot} of magnetic particles with magnetic moment $\mu_i = \mu_0 \hat{\mu}_i$ [122] in an external magnetic field H is given by the interaction between each particle and the field, and pairwise interaction between the particles, as

$$U_{tot} = -\mu_0 \sum_i \hat{\mu}_i \cdot H + \sum_{j>i} \left(u_{ij}^{dd} + u_{ij}^{nm} \right) . \tag{3.1}$$

The dipole-dipole interaction u_{ij}^{dd} between two identical particles, separated by $r_{ij} = r_j - r_i$, has the classical form [123]

$$u_{ij}^{dd} = (\mu_0^2 / r_{ij}^3) \left[\hat{\mu}_i \cdot \hat{\mu}_j - 3(\hat{\mu}_i \cdot \hat{r}_{ij})(\hat{\mu}_j \cdot \hat{r}_{ij}) \right] . \tag{3.2}$$

Following previous work [127, 125], I have described the nonmagnetic part of the inter-particle interaction $u_{ij}^{nm} = u^{nm}(r_{ij})$ by an isotropic potential with a soft-core short-range repulsion and a weak, long-range attraction with the functional form

$$u_{ij}^{nm} = \epsilon \left[\exp\left(\frac{\sigma - r_{ij}}{\rho_1} \right) - \exp\left(\frac{\sigma - r_{ij}}{\rho_2} \right) \right] . \tag{3.3}$$

To model the inter-particle interaction in a typical ferrofluid, I will consider particles with a magnetic dipole of $\mu_0 = 2.1\times10^4\ \mu_B$. To describe the nonmagnetic interaction between the particles, I chose $\rho_1 = 2.5$ Å, $\rho_2 = 5.0$ Å, $\sigma = 100.0$ Å, and $\epsilon = 8$ meV.

In absence of the magnetic interaction, the particle aggregates minimize their surface tension by forming compact, spherical clusters with a near-constant equilibrium inter-particle spacing $L_0 \approx \sigma = 100.0$ Å. The dipole-dipole interaction, on the other hand, favors straight chains of aligned dipoles with the same separation L_0. Independent of the aggregate size, the equilibrium geometry should be a compact arrangement of deformed chains. In the following, I will analyze complex geometries in terms of the particular arrangement of deformed chains of dipoles.

I use a straight, $N \rightarrow \infty$ membered chain, which is aligned with an external field H, as a reference structure. In this system, the potential energy per particle is given by

$$U^c = U^c_{tot}/N \approx -2\zeta(\mu_0^2/L_0^3) + u^{nm}(L_0) - \mu_0 H \ , \tag{3.4}$$

where $\zeta = \sum_{n=1}^{\infty} n^{-3} \approx 1.20206$.

To compare total energies of finite systems with very many particles and to make universal conclusions about structural transitions, I found it useful to map chains of aligned dipoles onto continuous magnetic rods of diameter $d \approx (\sqrt{3}/2)L_0 = 86.6$ Å and total length L, illustrated in Fig. 3.1(a). In the continuum description, one particle corresponds to a rod segment of length L_0. I define the rod diameter d as the axial separation between adjacent chains in the optimum staggered geometry depicted in the middle panel of Fig. 3.1(a).

The total energy of a system of interacting chains of dipoles, modeled by deformed magnetic rods, has three major contributions. The energy required to bend a straight chain segment of length L_0 to a circle of radius R, as shown in the left panel Fig. 3.1(a), is

$$\Delta U^{\mathrm{bend}} = +\alpha L_0/R^2 \ . \tag{3.5}$$

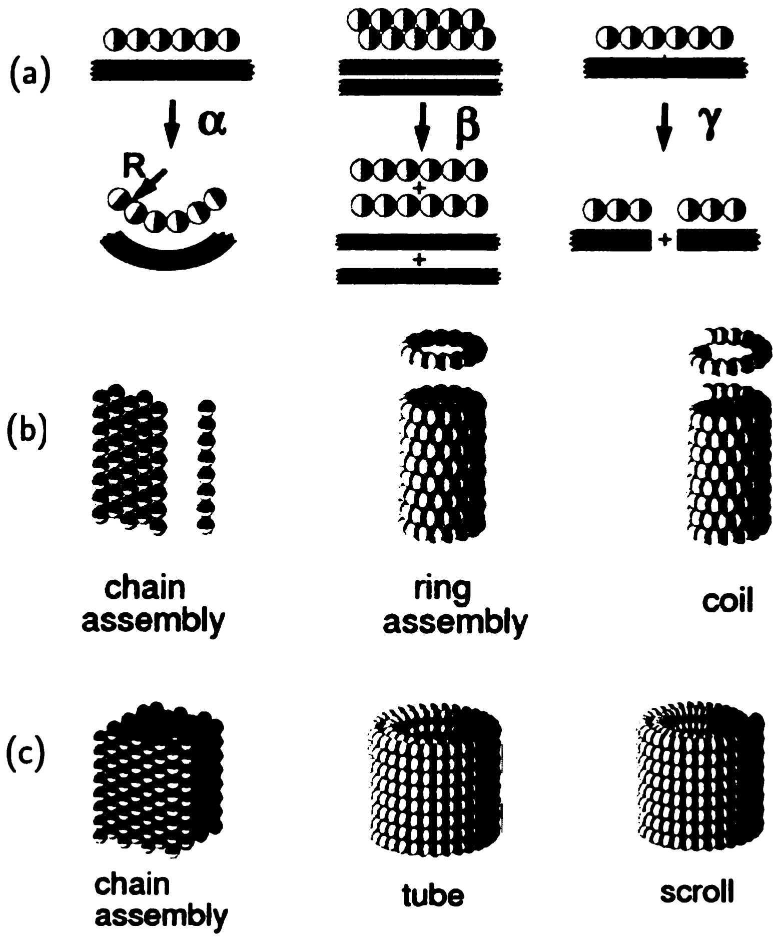

Figure 3.1: (a) Discrete and continuum models illustrating major energy terms associated with structural changes in an infinite chain of aligned dipoles, defined in Eqs. (3.5), (3.6), and (3.7), which govern the stability of dipole aggregates. (b) Two-dimensional assemblies of chains in planar layers, ring assemblies and coils forming single-wall tubes. (c) Three-dimensional assemblies of linear chains, multi-wall tubes, and scrolls. The dipole orientation of the individual particles, depicted as spheres, is visualized by the north (black) and south (white) hemispheres.

The inter-chain interaction energy gain, associated with the formation of chain pairs, is depicted in the middle panel of Fig. 3.1(a). This energy is maximized, when adjacent chains are offset axially by half a unit cell, and is given by

$$\Delta U^{\mathrm{ic}} = -\beta L_0 \,. \tag{3.6}$$

Finally, the energy investment to cleave a straight, infinite chain, illustrated in the right panel of Fig. 3.1(a), is

$$\Delta U^{\mathrm{cut}} = +\gamma \,. \tag{3.7}$$

Using the parameterized interaction within the ferrofluid, described above, I find $\alpha = \alpha_0 = 0.711$ eVÅ, $\beta = \beta_0 = 1.06\times10^{-4}$ eV/Å, and $\gamma = \gamma_0 = 5.70\times10^{-2}$ eV.

The equilibrium arrangement of the ferromagnetic particles results from the competing tendencies to minimize strain and to maximize the inter-particle attraction. A single, straight chain contains no strain, but contains two unstable ends. Linear chain assemblies, shown in the left panels of Fig. 3.1(b) and (c), experience further stabilization by the pairwise inter-chain interaction. Even though this geometry is also unstrained, the number of unstable ends is larger than in a single chain. Structures with unterminated chain ends may be stabilized by connecting these ends, which occurs at the expense of increasing strain energy. As shown in the middle panels of Figs. 3.1(b) and (c), a chain may thus form a ring, and rings may stack up to form a single-wall assembly or a multi-wall tube. In very large systems, where optimizing the inter-chain attraction is more important than avoiding a limited number of chain ends, we may find coils and multi-wall scrolls, shown in the right panels of Figs. 3.1(b) and (c), to compete favorably with ring assemblies and multi-wall tubes.

To check the accuracy of the continuum approach, I compared the results of the continuum and the discrete description for the two-dimensional structures depicted in Fig. 3.1(b). In the continuum approximation, the total energy of a two-dimensional multi-chain assembly of $N = L/L_0$ particles, distributed over N_c parallel chains of equal length, is

$$U^{mc} = +N_c\gamma - \beta L(N_c - 1)/N_c \tag{3.8}$$

with respect to the reference structure of same length L. The corresponding expressions for the energy of a multi-ring assembly and of a coil of radius R are, respectively,

$$\begin{aligned} U^{mr} &= -\beta(L - 2\pi R) + \alpha L/R^2 \, , & (3.9) \\ U^{coil} &= U^{mr} + \gamma \, . & (3.10) \end{aligned}$$

For a given number of particles N, corresponding to a total chain length L, the optimum number of chain segments N_c in the multi-chain assembly is determined by minimizing $U^{mc}(L, N_c)$ with respect to N_c, yielding

$$N_c^{opt} = (\beta/\gamma)^{1/2} L^{1/2} \, . \tag{3.11}$$

In a multi-ring assembly or a coil, the number of ring turns N_r is given by $N_r = L/(2\pi R)$, and its optimum value is obtained by minimizing the expression in Eq. (3.9) with respect to N_r, yielding

$$N_r^{opt} = \left(\frac{\beta}{8\pi^2\alpha}\right)^{1/3} L^{2/3} \, . \tag{3.12}$$

With the optimum number of rings given by Eq. (3.12), the optimum radius R^{opt} increases monotonically with L as

$$R^{opt} = \left(\frac{\alpha}{\pi\beta}\right)^{1/3} L^{1/3} \, . \tag{3.13}$$

A comparison between the continuum results, energies per particles in given structural motives are compared, which are in quite good agreements as shown in

Fig. 3.2(a) and (b). Also the results based on Eqs. (3.8) and (3.9), and those based on the discrete model, described by Eq. (3.1), are presented in Fig. 3.3(a) and (b). In view of the fact that no restrictions were placed on N_c or N_r being an integer in the continuum approach, I find the agreement between the two sets of results very satisfactory. Since a similar agreement between the discrete and the continuum model is achieved also for the three-dimensional aggregates, depicted in Fig. 3.1(c), I will base the following discussions on the continuum approach.

The structural transitions within the suggested motifs (two-dimensional multi-chain, multi-ring, and coil) are observed. A single-chain to double-chain transition occurs as the the number of particles (N) is larger than 24 ($L > 0.24\mu m$) and a triple-chain structure becomes a possible ground state when $83 < N < 144$, which is presented in Fig. 3.3(a). Considering multi-ring (coil) structures, a double-ring (double-winded coil) structure becomes a possible equilibrium structure when $N > 12$. Finally, a six-fold ring (six-fold-winded coil) structure is the most stable structure for up to 100 particles as shown in Fig. 3.3(b).

With the optimum structural parameters giving by Eqs. (3.11), (3.12), and (3.13), the energy of the optimized two-dimensional chain and ring assemblies, as well as coils, is given by Eqs. (3.8), (3.9), and (3.10). A structural phase transition between the motifs are observed (Fig. 3.3 (c)): a chain to ring transition occurs for $L > 0.03\mu m$ ($N > 3$) and a chain to coil transition occurs for $L > 0.18\mu m$ ($N > 18$).

As an extension of my approach, I consider single-walled and multi-walled tube structures and scroll as next possible equilibrium structures (Fig. 3.1 (c)). A $l \times w$ (length l and width w) sheet consisting of a ferrofluid chain (total length L) was considered to create (single and multi-walled) tube and scroll structures.

There are three interactions to describe energy of multi-walled tubes: strain energy (ΔU^s), inter-ring (chain) interaction (ΔU^{ir}), inter-wall interaction (ΔU^{iw}).

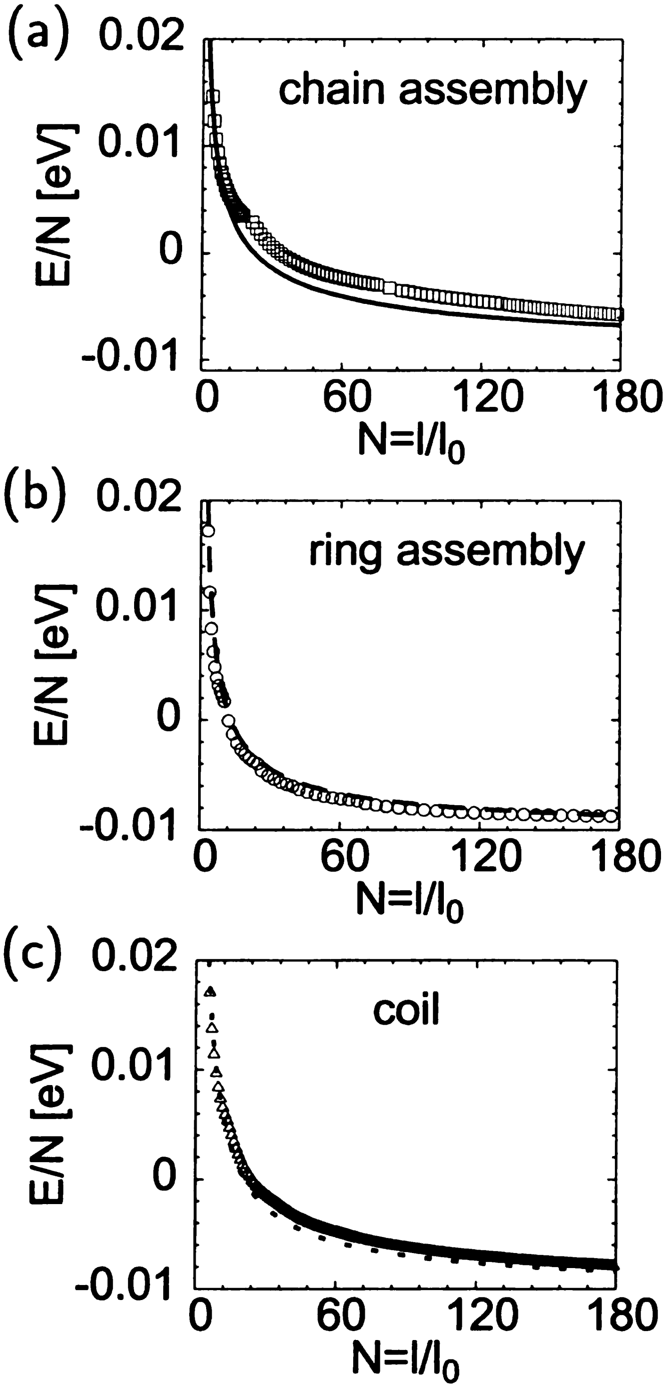

Figure 3.2: A comparison between discrete and continuum approach for energy for a chain assembly (a), a ring assembly (b), and a coil structure as a function of number of particles. Lines in each curves are the results from continuum approach and points are from numerical approach.

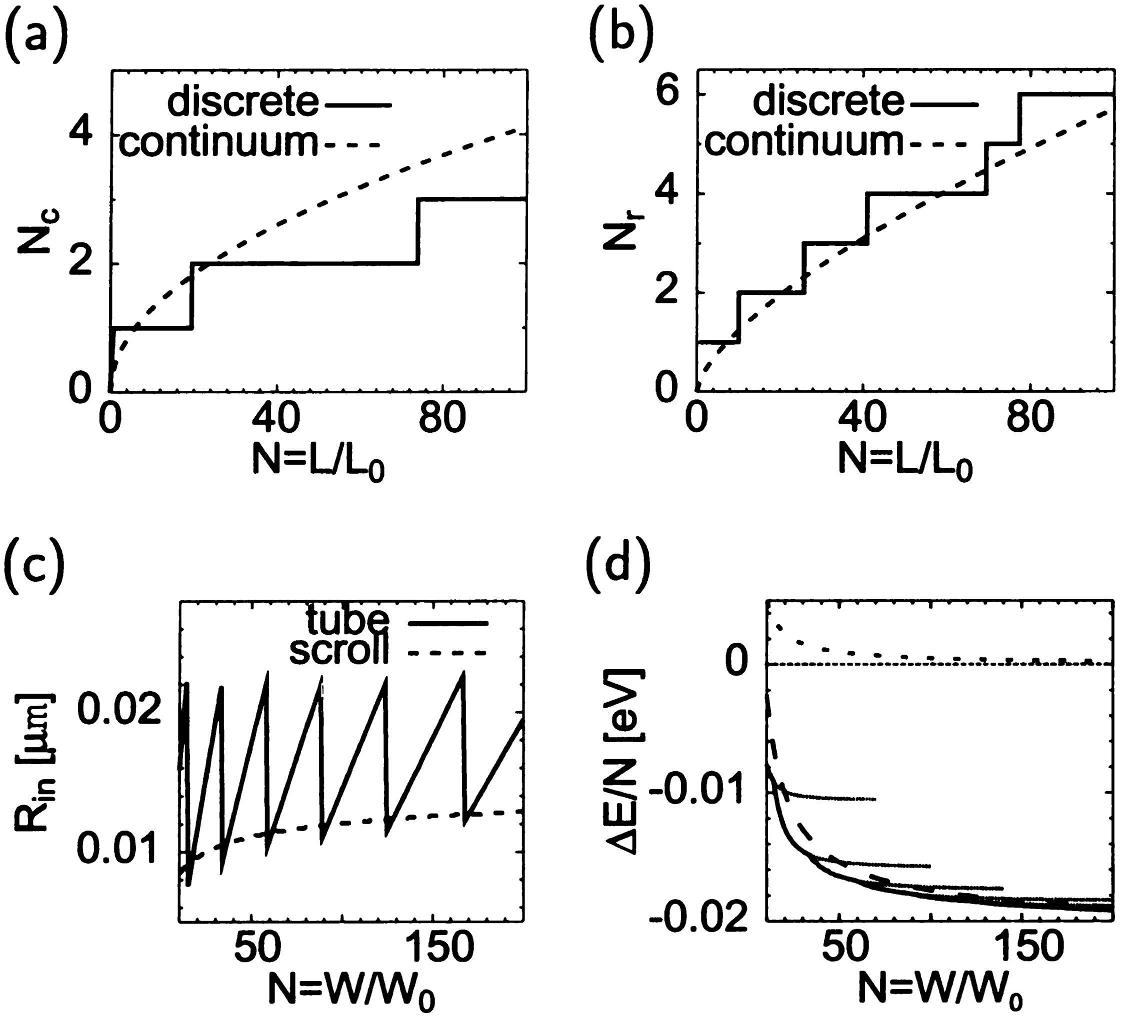

Figure 3.3: The optimum number of chains, N_c, (a) and rings, N_r, (b) as a function of system size (N). Numerical calculations by structural optimization are shown as solid lines. The results from the continuum approach are shown as dashed lines. For numerical calculations, I performed optimization up to 100 particles ($L > 1.0\mu m$). The results indicate the structural phase transitions within given motifs. (c) Dependence of the optimum interior radius of a scroll (dashed line) and a multi-wall tube (solid line) on number of particles $N = w/L_0$. Abrupt changes of R_{in} occur in multi-wall structures, when the optimum number of walls changes. (d) Total energy of multi-wall tubes and scrolls with respect to a reference strip of the same length and the width w. For sufficiently large values of w, tubular structures are preferred to the planar strip and approach the energy energy of infinite chain structure. The higher stability of multi-wall tubes over scrolls results from the absence of exposed edges.

The energy cost from bending $l \times w$ ferrofluid plane to make N_w-walled tube is

$$\Delta U^s = 2\pi\alpha \frac{l}{\Delta R} \sum_{n=1}^{N_w} \frac{1}{R_{in} + (n-1)\Delta R}, \tag{3.14}$$

where R_{in} is the inner-most tube radius, and the optimized inter-tube distance ΔR is $\sigma\sqrt{3}/2$. The inter-ring (inter-chain) interaction is given by

$$\Delta U^{ir} = -2\pi\beta(N_r - 1) \sum_{n=1}^{N_w} (R_{in} + (n-1)\Delta R). \tag{3.15}$$

Here, N_r is the number of rings in each tube. This interaction is identical to $-\beta w(N_r - 1)$. With total contact length l_c ($=l - \pi(R_{in} - R_{out})N_r$), inter-tube interaction length, the inter-wall interaction ΔU_{iw} is given by $-\beta \times l_c$. The energy of tube U^{tube} is obtained by the sum of ΔU^s, ΔU^{ir}, and ΔU^{iw}. Hence,

$$U^{tube}/l = \frac{2\pi\alpha}{\Delta R} \sum_n \frac{1}{R_{in} + (n-1)\Delta R} - \frac{\beta}{\Delta R}(2w - \pi(R_{in} + R_{out})). \tag{3.16}$$

For a scroll structure, the additional term ΔU_e, penalty from exposed edge, should be considered. For a given number of chains N_r ($= l/\Delta R$) in a ferrofluid sheet, ΔU^e is γN_r. Since radius of coil $R(\theta)$, depend on winding angle (θ) and is expressed as $R_{in} + \theta\Delta R/2\pi$, the strain energy of a coil structure is

$$\Delta U^s = \frac{2\pi l}{(\Delta R)^2} \ln(\frac{R_{out}}{R_{in}}), \tag{3.17}$$

R_{out} is the out-most scroll radius. The inter-ring (chain) and inter-wall interactions are same as those of multi-walled tube. The resultant energy formula for scroll U^{scroll} per unit length l is

$$U^{scroll}/l = \frac{2\pi\alpha}{(\Delta R)^2} \ln(\frac{R_{out}}{R_{in}}) - \frac{\beta}{\Delta R}(2w - \pi(R_{in} + R_{out})) + \frac{\gamma}{\Delta R}. \tag{3.18}$$

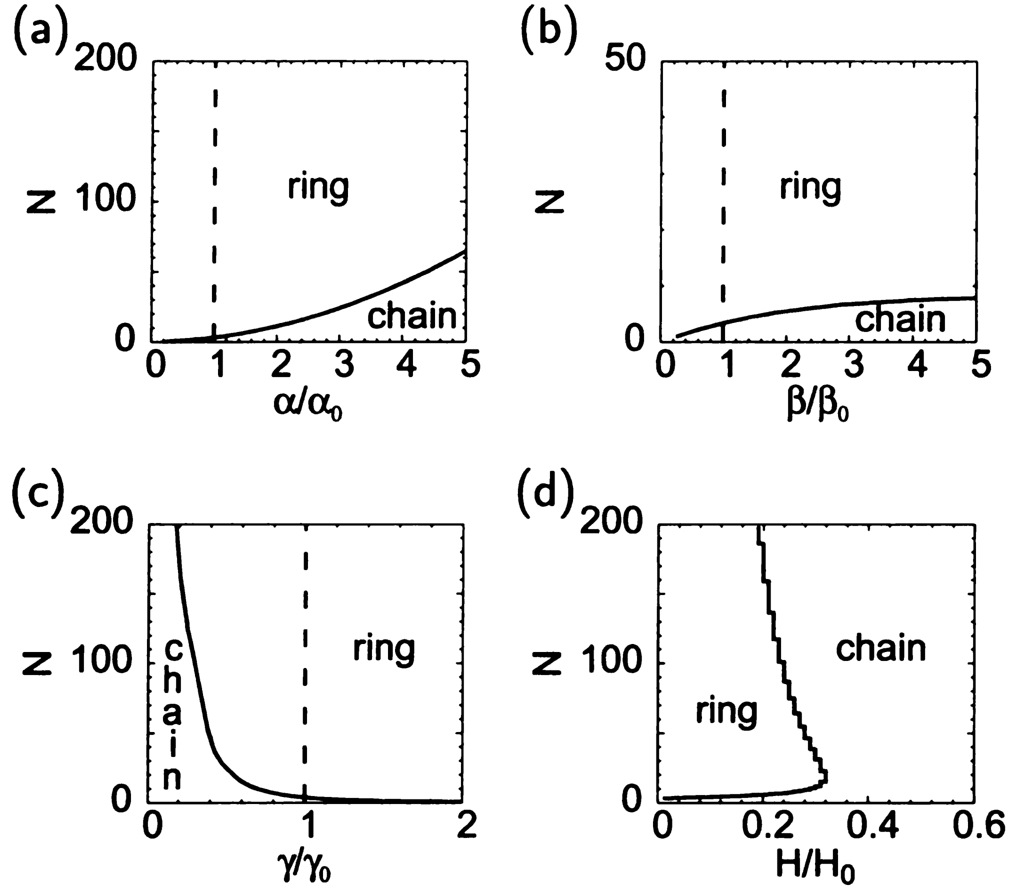

Figure 3.4: The "phase" diagram as a function of parameters: α (a), β (b), γ (c), and external magnetic field (d). The change of β and γ corresponds to the effect of liquid which covers magnetite in a ferrofluid. All parameters are rescaled: $\alpha_0 = 0.711$ eVÅ, $\beta_0 = 1.0566\times10^{-4}$ eV/Å, and $\gamma_0 = 0.05698eV$. $H_0 = 10^{-2}$ eV/μ_0

To generalize my approach of describing system using continuum approximation I investigate the effects of surfactant and external magnetic field on the structural phase transitions.

Figures 3.4 (a)-(c) show the "phase" diagram as a function of parameters (α, β, and γ), which is used in continuum approach. Especially, β and γ corresponds to the effect of surface tension from liquid and magnetite interface in a ferrofluid. As I change the interaction between liquid and particles, the change of "phases" are predicted as shown in Fig. 3.4 (b) and (c). All parameters are rescaled by the value from my present model system, meaning kerosene based ferrofluid.

To properly describe the effect of magnetic field in my scheme I consider the special case: no internal structure change can be induced by external magnetic field. Under this special condition, no external magnetic field contribution is expected for ring assembly and coil structures due to zero total magnetic moment. However, the energy gain is expected for the case of chain assembly under external magnetic field. Therefore, the Eq. 3.8 becomes

$$U^{mc} = +N_c\gamma - \beta L(N_c - 1)/N_c - H\mu_0 l/\sigma. \tag{3.19}$$

The effect of external magnetic field on "phase" diagram is displayed in Fig. 3.4(d). For the strong magnetic field chain assembly becomes to be the only possible phase. However, ring assembly is still most possible structure for the large system under not strong magnetic field.

3.3 Targeted Medication Delivery Using Magnetic Nanostructures

The following discussion on the targeted medication delivery using magnetic nanostructures follows that presented in Reference [128].

I use advanced quaternion molecular dynamics to model a potential application of magnetic nanostructures for targeted medication delivery. Inert microcapsules, containing the active medication and a small number of magnetite nanoparticles, may be transported using an inhomogeneous magnetic field through blood vessels to a desired location in the body. Triggered by an abrupt change in the applied field, structure of magnetite aggregates changes from a ring to a chain, thus puncturing the microcapsule and releasing the medication. The stability of the magnetic nanostructures under thermal and magnetic fluctuations has been also studied to prevent an accidental delivery.

The magnetic particles, typically consisting of magnetite, have a typical diameter of few hundred Ångstroms, carry a large permanent magnetic moment of the order of magnitude $10^4 - 10^5$ μ_{B}, and are covered by an approximately 20 Å thick surfactant layer which prevents them from coalescing at room temperature in a viscous suspension. Spontaneous formation of complex labyrinthine [131, 120] and branched [129] macroscopic structures has been observed and theoretically addressed [116, 132, 133, 134, 135, 136] in these systems at low temperatures and in applied magnetic fields.

Of particular interest in this study is the fact that aggregates of $4 \leq n \leq 14$ magnetic tops are a classically tunable two-level system [137]. Their most stable structure in zero field is a ring, but they open to a chain when exposed to a large nonzero magnetic field [130]. In this contribution, we describe a possible application of this structural transition as a one-way valve causing liquid-filled microcapsules to burst.

Microcapsules have been used extensively in medicine as micro-containers that transport and deliver an active substance to a specific site in the human body. Their typical diameter of 0.1 μm is small enough to allow the microcapsules to pass through all capillary blood vessels. The most significant application of this technique is in the chemotherapy of cancer, since the most potent drugs are indiscriminately toxic to all tissue. Such substances should not come into contact with healthy tissue, and only be locally delivered in the tumor region.

The standard solution to this problem has been to use albumin, polyalkylcyanoacrylate, ethylcellulose or polyglutaraldehyde for the membrane, that would safely contain the drug, yet biodegrade over time. Here we describe an alternate local drug delivery mechanism, based on the structural transition of an aggregate of magnetic tops, that allows to move the microcapsules to a particular location and to deliver the active substance in a planned fashion using a time-dependent magnetic field [138].

The principle of the mechanism proposed is illustrated in Fig. 3.5(a) and (b). We propose to enclose several magnetic nanoparticles together with the active drug in the microcapsule. In zero or very low applied magnetic field these particles will aggregate to a ring that fits snugly in the microcapsule (see Fig. 3.5(a)). A low inhomogeneous magnetic field can be used to concentrate the microcapsules in a particular location. At this moment, application of a stronger magnetic field will cause the ring of magnetic tops to open up to a chain [130] (see Fig. 3.5(b)). The imposed deformation of the cage will cause it to burst open, releasing the active substance at the desired location.

Of course, the response of the system to the environmental variables such as temperature and magnetic field is critical for the successful application of this technique. There is significant freedom in selecting the system parameters, such as the diameter of the microcapsules, their surface tension, the diameter and the permanent magnetic moment of the magnetic tops, the spatial variation and the strength of the externally

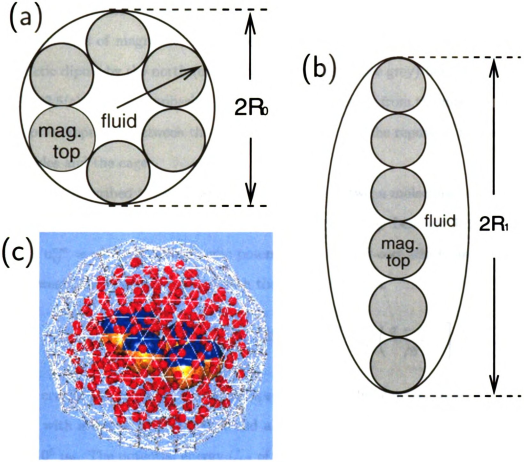

Figure 3.5: (a) In zero field, the equilibrium structure of the tops is a ring that fits into a spherical membrane of radius R_0. (b) In nonzero field the ring opens up to a chain, thus deforming the membrane to an ellipsoid with long axis R_1. The capsule will burst if $R_1 \gg R_0$.(c) Schematics of our model system. The outer shell of the microcapsule, consisting of mesh of 368 particles, contains 375 medication particles (grey) and six magnetic top of magnetite, which are represented by the large spheres with their magnetic dipole by the north (dark grey) and south (light grey) hemispheres.

applied magnetic field.

In our model, the outer shell of the microcapsule, a cage, consisting of a mesh of 368 particles (white rods), contains 375 medication particles (grey), and six spherical magnetic tops of magnetite, which are represented by the large spheres with their magnetic dipole by the north (dark grey) and south (white grey) hemispheres shown in Fig. 3.5(c). The near spherical shape of the cage results from the internal pressure due to the repulsion between the enclosed molecules and the repulsion between these molecules and the cage.

I have described the nonmagnetic interactions between molecules (microcapsule particles, medication particles, and magnetites) i and j by Lennard-Jones type potential $u_{ij}^{nm} = u^{nm}(r_{ij})$, an isotropic potential with a soft-core short-range repulsion and a weak, long-range attraction with the functional form:

$$u_{ij}^{nm} = \epsilon \left[\left(\frac{\sigma}{x}\right)^{p1} \exp\left(\frac{\sigma - r_{ij}}{\rho_1}\right) - \left(\frac{\sigma}{x}\right)^{p2} \exp\left(\frac{\sigma - r_{ij}}{\rho_2}\right) \right] \tag{3.20}$$

A crucial component of the microcapsule are six spherical magnetic tops of magnetite, with a diameter σ of 200 Å and a large permanent magnetic moment μ_0 of 1.68×10^5 μ_{B}. The potential energy U_{tot} of magnetic particles with magnetic moment $\mu_i = \mu_0 \hat{\mu}_i$ [122] in an external magnetic field H is given by the interaction between each particle and the field, and pairwise interaction between the particles, as

$$U_{tot} = -\mu_0 \sum_i \hat{\mu}_i \cdot H + \sum_{j>i} \left(u_{ij}^{dd} + u_{ij}^{nm}\right) \ . \tag{3.21}$$

The dipole-dipole interaction u_{ij}^{dd} between two identical particles, separated by $r_{ij} = r_j - r_i$, has the classical form [123]

$$u_{ij}^{dd} = (\mu_0^2/r_{ij}^3)\left[\hat{\mu}_i \cdot \hat{\mu}_j - 3(\hat{\mu}_i \cdot \hat{r}_{ij})(\hat{\mu}_j \cdot \hat{r}_{ij})\right] \ . \tag{3.22}$$

The nonmagnetic interaction between magnetites has been described by Eq. 3.20 using parameters of $\rho_1 = 5.0$ Å, $\rho_2 = 10.0$ Å, $p1 = 4$, $p2 = 0$, and $\epsilon = 64$ meV.

In absence of the magnetic interaction, the particle aggregates minimize their surface tension by forming compact, spherical clusters with a near-constant equilibrium inter-particle spacing $L_0 \approx \sigma = 200.0$ Å. The dipole-dipole interaction, on the other hand, favors straight chains of aligned dipoles with the same separation L_0. Independent of the aggregate size, the equilibrium geometry should be a compact arrangement of deformed chains [121].

The optimum configuration for six magnetic particles has been studied using the conjugate gradient technique [139]. Instead of spanning whole configuration space, we reduce our configuration space to a volume of a hard sphere with radius r_0 of 800.0 Å, which physically represents a delivery cage in our system. This approach helps to efficiently search a relaxed geometry. A ring phase (as shown in uppermost figure in Fig. 3.6(b)) known as an optimum geometry for a small system [130] is obtained at zero magnetic field from an arbitrary geometry. On the other hand a chain phase is obtained under external magnetic field of 1500 Oe (as displayed in uppermost figure in Fig. 3.7(b)).

To prevent the accidental delivery of medications under thermal or magnetic fluctuations, we need to understand the thermodynamic behavior of ferromagnetic particles. I study the thermodynamic behavior of six ferromagnetic particles confining in a hard sphere. I use microcanonical molecular dynamics (MD) simulations, where quaternion parameters [140] have been employed to properly describe the rotational motion of a magnetic top and to prevent the discontinuity and divergency as we solve equations of motion of the system. A fourth-order Runge-Kutta formalism is employed to integrate the Euler-Lagrange equations to obtain the trajectories of the particles [141] with a time step of 0.01 ns.

I choose the optimum geometry at a given magnetic field (a ring for zero magnetic

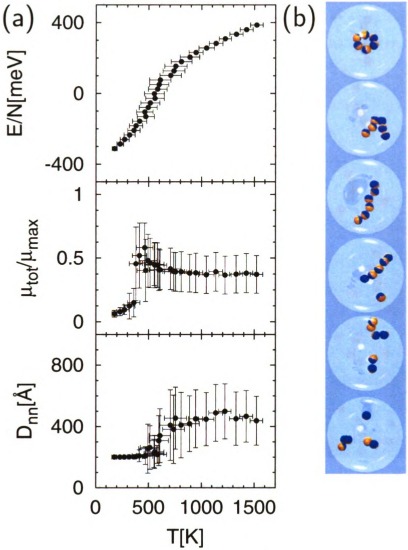

Figure 3.6: (a) Microcanonical molecular dynamics simulations have been performed to study the thermodynamic behavior of six ferromagnetic particles. Energy per particle as a function of temperature is shown in the upper panel. The slop of energy changes continuously between 400 and 800 K, which may correspond to a critical points for an infinite system. At high temperature ($T \geq 800$ K) the slop reaches at $3k_B$. The total mean magnetic moment μ_{tot}, an indicator to distinguish thermally equilibrium structures (rings and chains), is monitored with respect to maximum magnetic moment of system ($\mu_{tot} = N\mu_0$) as a function of temperature, which indicates the structural change from a ring ($\mu_{tot}/\mu_{max} \approx 0$) to chain segments ($\mu_{tot}/\mu_{max} \gg 0$) (middle panel). The average closest inter-particle distances has been also presented to monitor the structural changes (lower panel). (b) The snapshots of geometry at T $\approx$ 300, 400, 500, 600, 700, and 1000 K.

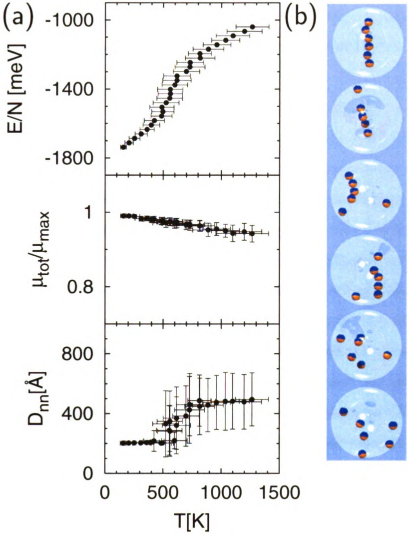

Figure 3.7: (a) Microcanonical molecular dynamics simulations have been used to study the thermodynamic behavior of six ferromagnetic particles under external magnetic field of 1500 Oe. The energy per particle as a function of temperature is displayed with error bars in energy and temperature (upper panel). The slope of energy continuously changes at the temperature range of 400 and 800 K, which may correspond to a critical points for an infinite system. The total magnetic moments μ_{tot} is monitored with respect to maximum magnetic moments of system μ_{max} ($=N\mu_0$) as a function of temperature, which show fluctuations in the orientations of each magnetic tops under high temperature (middle panel). The closest inter-particle distances are displayed to monitor structural transitions as a function of temperature. The melting of a chain structure occurs around 800 K. (b) The snapshots of geometry at T ≈ 300, 400, 500, 600, 700, and 1000 K from microcanonical molecular dynamics simulation discussed in (a).

field or a chain for high magnetic field) as a starting configuration of MD simulations. The described hard sphere (r_0=800 Å) has been used as a microcapsule containing six ferromagnetic particles. The system has been equilibrated at each given energy for 0.1 μ sec, corresponding to 10^4 steps in simulations. The average energies per particles (solid circle) as a function of temperature are presented with error bars, standard deviations in temperature and energy (upper panel of Fig. 3.6(a) and Fig. 3.7(a)). Also, the total magnetic moments μ_{tot} of the system ratio to maximum magnetic moment μ_{max} (=$N\mu_0$) as a function of temperature are displayed in the middle panels of Fig. 3.6(a) and Fig. 3.7(a). The lower panels in Fig. 3.6(a) and Fig. 3.7(a) show closest inter-particle distances D_{nn} as a function of temperature.

In case when no external magnetic field has been applied, the gradual change in energy slope (specific heat) occurs between 400 and 800 K (lower panel of Fig. 3.6(a)), which may correspond to a transition point for an infinite system. Based on the energy difference between a ring and a chain phase, 32.68 meV per particle, the approximate order of transition temperature of ≈ 380 K can be estimated. To identify the structure at a given temperature I monitor the total magnetic moments and the closest inter-particle distances during MD simulations.

Magnetic moment can be a good indicator to easily distinguish magnetic isomers since their equilibrium structure of small clusters ($4 \leq N \leq 14$) is either a ring or a chain. A ring phase can be identified by the magnetic moments ratio of $0 \leq \mu_{tot}/\mu_{max} \ll 1$ and a broken ring structure (chain segments) can be also identified by $0 \ll \mu_{tot}/\mu_{max} \leq 1$. The total magnetic moments ratio in the middle panel of Fig. 3.6(a) identify the expected transition from the energy curve: A ring phase to chain segments transitions occurs occurs between 400 and 800 K. Since no external magnetic field is applied, chain segments are not aligned in one direction, which results total magnetic moments of ≈ 0.5, far below the value of aligned chains, 1.0. The closest inter-particle distance D_{nn} plot shown in the lower panel in Fig. 3.6(a) confirms above observations. D_{nn} for a perfect ring and a perfect chain is ≈ 200.0 Å.

At high temperature (T_m=$T \geq 1000$ K) specific heat reaches to $3k_B$, which can be explained by equipartition theorem considering 6 degrees of freedom for each particle. This convergence in a specific heat indicates the structural melting (see downmost snapshot in Fig. 3.6(b)). Above T_m the average D_{nn} reaches to ≈ 470.0 Å due to spatial confinements and μ_{tot}/μ_{max} reaches to ≈ 0.4. Snapshots in Fig. 3.6(b) show a structural evolution as temperature increase at 300, 400, 500, 600, 700, and 1000 K.

The changes in energy slope also occurs at temperature range of 400 and 800 K as an external magnetic field of 1500 Oe has been applied (in the upper panel of Fig. 3.7(a)). Since high magnetic field has been applied, total magnetic moments can only indicate the rotational fluctuations in each top under thermal fluctuations. Considering the energy gain of each particle by interacting an external magnetic field, 1.46 eV, the rotational fluctuation of each magnetic top at low temperature can be estimated as 5.89×10^{-5} K^{-1} in the middle panel of Fig. 3.7(a). To identify isomers at each temperature we also monitor the D_{nn}. D_{nn} shown in the lower panel of Fig. 3.7(a) shows same behavior as that of non magnetic field case, meaning a single chain to chain segments transitions occurs between 400 and 800 K. The specific heat reaches to $3k_B$ above 100 K, indicating a melting of structure. Snapshots in Fig. 3.7(b) show a structural evolution as temperature increase at 300, 400, 500, 600, 700, and 1000 K.

Unlike an infinite system, where a divergence in specific heat observed at a phase transition point, a transition point is expanded as a transition region in a finite system. Since the system properties (possible isomers) of a ferrofluid system strongly depend on its size, the method like finite size scaling cannot be applied to the system to study the nature of the transition. Instead, the nature of the transition between two ordered phases, rings and chains, in a finite system is explicitly analyzed and identified as a "first-order" like transition using Metropolis Monte Carlo simulations [137].

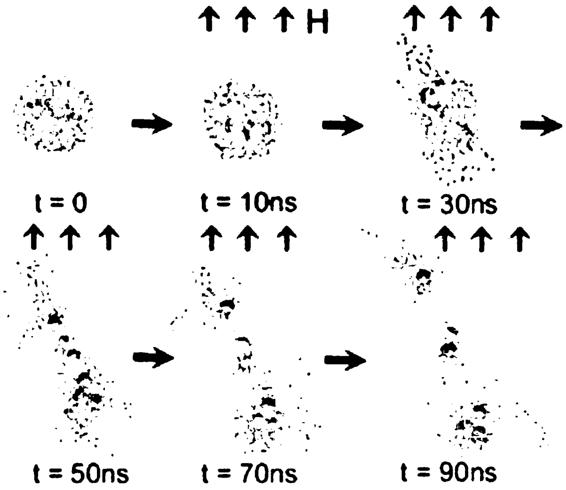

Figure 3.8: Inter-atomic bonds in the membrane are shown by the white rods, and the fluid molecules by the small red spheres. The magnetite particles are represented by the large spheres and the orientation of their magnetic dipole by the north (blue) and south (yellow) hemispheres. The five snap shots of the geometry after switching on the magnetic field of 1500 Oe at t = 10, 30, 50, 70, and 90 ns.

Finally, I investigate the targeted medication delivery using those magnetic particles. There are obviously various ways to understand the bursting of the microcapsule due to the structural transition in the magnetite aggregate in a quantitible fashion. My approach to this problem is to use MD simulations. In order to simulate field-induced medication delivery in a human body, I apply a magnetic field of 1500 Oe [142] and equilibriated the system at 300 K starting from the optimum geometries at a given magnetic field, and follow the structural evolution for a total time of 100 ns with time step of 0.01 ns. Based on the thermodynamic properties of six ferromagnetic particles, we can make sure that the ring phase will be maintained inside a microcapsule up to 400 K, which is far higher than human blood temperature, 310 K.

The results are shown in Fig. 3.8. The six consecutive snap shots illustrate the the time evolution of the bursting process. The magnetite preserve a ring configuration until ≈20 ns. The whole system of magnetites is rotated along the direction of magnetic field with keeping its initial optimum structure from no magnetic field (see snap shots at 10 ns in Fig. 3.8). With the structural change of magnetite assembly to a chain, the first onset of the bursting can be observed after ≈30 ns, where several fluid particles escapes from the microcapsule through a small hole in the cage. Then I observe the hole size to increase very fast following the initial fracture. 90 ns following the application of the magnetic field all fluid particles escape from the cage and the microcapsule collapses.

In conclusion, we developed quaternion molecular dynamics to model ferromagnetic particles for the use of potential application of magnetic nanostructures for targeted medication delivery. First, I study the energetics and thermodynamic behavior of six ferromagnetic particles in a hard sphere, modelling a medication microcapsule. My study shows the stability of delivery process under thermal or magnetic fluctuations. The microcapsule, containing medication and a small number of magnetite, can be destroyed by the structural transition of magnetite inside from ring to chain under magnetic fields, thus releasing the medication. My molecular dynamics simulations shows the successful medication delivery within ≈100 ns under magnetic fields of 1500 Oe.

3.4 Summary

In this section, I discuss the ground state configuration for a ferromagnet string suspended in a viscous liquid. I suggested a continuum approach as an efficient tool to study structural transitions, which is in good agreement with numerical computations. Based on the known configuration, chain and ring, we have investigated possible ground structures like chain and ring assembly, coil, multi-wall tube, and scroll structures. The structural phase transitions between the motifs were observed. To completely describe the system using our new approach, I consider the effect of ferrofluid liquid and external magnetic field on structural phase transitions. The phase diagrams depending on those parameters were presented.

I also use quaternion molecular dynamics to properly describe dynamic properties of ferromagnetic particles in a viscous liquid. I suggest ferromagnetic particles for the use of potential application of magnetic nanostructures for targeted medication delivery. The microcapsule, containing medication and a small number of magnetite, can be destroyed by the structural transition of magnetite inside from ring to chain under magnetic fields, thus releasing the medication. Our molecular dynamics simulations shows the successful medication delivery within $\approx$100 ns under magnetic fields of 1500 Oe.

Chapter 4

Quantum Transport through Molecules: Effect of Structural Changes

4.1 Theoretical Techniques

In this section, I will review the formulas and techniques applied to study the transport properties of mesoscopic systems.

In a mesoscopic system, where a system dimension is smaller than the mean-free path and the phase coherence length, carriers can travel an active region without scattering and moving elastically (ballistic transport) except for a possible reflection from a barrier. In this ballistic regime transport is determined in terms of reflection and transmission of carriers produced by elastic scattering from inhomogeneity or boundaries (barriers).

Our conductance calculations are based on the Landauer-Büttiker formula [143], which relates the conductance of a system to the scattering problem in mesoscopic systems. To evaluate the transport coefficient and hence to calculate the conductance,

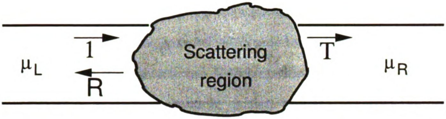

Figure 4.1: Illustration of a system for conductance calculation. Scattering region is sandwiched between left L and right electrode R which have chemical potentials of μ_L and μ_R, respectively. An incoming electron from left-electrode has a probability of T to be transmitted and R to be reflected from a scattering region, where $T+R$=1.

the general Green's function formalism, developed by Sanvito et al. [145], has been applied. In this approach the electronic structure of a system is described by a tight-binding model.

Also, the advance technique describing a non-equilibrium electronic situation based on Green's function technique and *ab initio* density functional theory, as implemented in the TRANSIESTA code [148], is applied to calculate current-voltage characteristics.

4.1.1 Conductance Calculations: Green's function technique

Our interest is to calculate a conductance of a mesoscopic system comprising of a scattering region contacted to semi-infinite electrodes in both sides (see Fig. 4.1). Electrodes are assumed to be ballistic conductors and act as a thermal bath where there are no phase correlations between incoming and outgoing electrons. If we assume chemical potentials are μ_L for left-electrode L and μ_R for right-electrode, where $\mu_L > \mu_R$, current flows take place entirely in the energy range between μ_L and μ_R at low temperature and low bias limit. Then, the current emitted from left-electrodes becomes [146]

$$I = ev\frac{\partial n}{\partial E}(\mu_L - \mu_R), \tag{4.1}$$

where $\partial n/\partial E$ is the electron density of states and v is a group velocity.

Since the scattering regions is sandwiched between two semi-infinite electrodes, each carrier propagating from left-electrode to the scattering region has a finite probability T to be transmitted and R to be reflected, where $T + R$=1. Generally, when there exist N_c scattering channels, carriers propagating from the n-th channel in the left-electrode has a probability $T_{mn}(= |t_{mn}|^2)$ to be transmitted to the m-th channel in the right electrode. Therefore the total net current I from the left to the right becomes

$$I = ev\frac{\partial n}{\partial E}(\mu_L - \mu_R)\sum_{mn}^{N_c} T_{mn}. \tag{4.2}$$

For one-dimensional case, we can decide the current and conductance using the relationship $e\Delta V = \Delta\mu$ and the density of state of $\partial n/\partial E$=$1/2\pi v\hbar$,

$$I = \frac{e}{h}(\mu_L - \mu_R)\sum_{mn}^{N_c} T_{mn},$$

$$G = \frac{I}{\Delta V} = \frac{e^2}{h}\sum_{mn}^{N_c} T_{mn},$$

here the spin degeneracy is not considered and $2e^2/h$ is called as a quantum conductance G_0 (G_0^{-1}=12.9 kΩ). The above equation which relates the conductance with transmission coefficients is the Landauer-Büttiker formula [143]. The total transmission probability, $\sum_{mn}^{N_c} T_{mn}$=Tr$\{tt^\dagger\}$, can be calculated using scattering matrix S defined as:

$$S = \begin{pmatrix} r & t' \\ t & r' \end{pmatrix}, \tag{4.3}$$

where r and t are reflection and transmission matrix of electrons injecting from left side and r' and t' are those from right side of a scattering region.

To use the Landauer-Büttiker formula for conductance calculation first we need to calculate scattering matrix and hence transmission coefficient. In the following I will review the technique developed by Sanvito et al. [145] to calculate the scattering

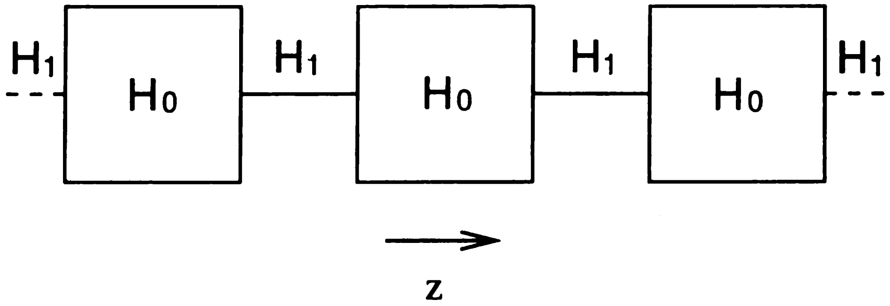

Figure 4.2: Representation of a semi-infinite electrode by a periodic array of conducting units called slices [145]. H_0 represents the intra-slice interaction and H_1 represents the coupling between adjacent slices. z indicates the transport direction.

matrix of the system consisting of an arbitrary scattering region sandwiched between two semi-infinite crystalline electrodes.

Let us consider an infinite system consisting of periodic slices and each unit is described by a intra-slice matrix H_0 and a hopping matrix between a nearest neighboring inter-slice H_1 (see Fig. 4.2), where H_0 is Hermitian and $H_{-1}{=}H_1^{\dagger}$. The total Hamiltonian of the system can be described by a tridigonalized matrix with diagonal components of H_0 and off-diagonal components of H_{-1} and H_1. The column vector corresponding to a slice at position z (transport direction) is

$$H_0\psi_z + H_{-1}\psi_{z-1} + H_1\psi_{z+1} = E\psi_z, \tag{4.4}$$

where z is an integer in the units of inter-slice distance. If we allow N quantum numbers corresponding to the degree of freedom within a slice, the column vector can be identified as ψ_z^μ $(\mu = 1, \cdots, N)$.

To solve the Schrödinger equation (Eq. 4.4) let us introduce the Bloch state,

$$\psi_z = Ae^{ik_z z}\phi_{k_z}, \tag{4.5}$$

which makes it convenient to describe a periodic system. Here, k_z is the k component in transport direction, ϕ_{k_z} is a normalized column vector, and A is an arbitrary constant. Then Eq. 4.4 can be rewritten as

$$\left(H_0 + H_{-1}x + H_1 x^{-1}\right)\phi_{k_z} = E\phi_z. \tag{4.6}$$

where $x = e^{-ik_z}$. We can determine all possible values of k_z at a given energy E by solving $\det\left(H_0 + H_1 x + H_{-1}x^{-1} - E\right) = 0$. There are two sets of roots in Eq. 4.6: (1) N wave vectors of k_z^μ ($\mu = 1, \cdots, N$) of positive real value (right-moving solution) and of positive imaginary value (right- decaying solution) (2) $\overline{k}_z^\mu$ ($\mu = 1, \cdots, N$) of negative real value (left-moving solution) and of positive imaginary value (left-decaying solution). From now on I will use a notation k_μ and $\overline{k}_\mu$ to represent k_z^μ and $\overline{k}_z^\mu$, respectively. For numerical purpose, it is more convenient to map Eq. 4.6 onto matrix H

$$H = \begin{pmatrix} -H_1^{-1}(H_0 - E) & -H_1^{-1}H_{-1} \\ I & 0 \end{pmatrix},$$

where I is a N-dimensional identity matrix and H_1 is not singular.

In the scattering problem it is useful to consider the retarded Green functions instead of wave functions [147]. Our goal is to describe the whole system, consisting of two semi-infinite electrodes and a scattering region. The semi-infinite electrodes can be described by an infinite electrode with imposing proper boundary conditions in Green's function. Therefore, let us consider the case of infinite electrodes and derive the case of semi-infinite electrodes with proper boundary condition, and finally we will describe the whole system with the combination of scattering region, which will be described by an effective Hamiltonian. Finally, the total Green's function can be obtained by solving a Dyson Equation.

Retarded Green's function $g_{zz'}$ of infinite system satisfies

$$[(E-H)\,g]_{zz'} = \delta_{zz'}. \tag{4.7}$$

Therefore, the Green's function is simply a wave function except at $z{=}z'$:

$$g_{zz'} = \begin{cases} \sum_{\mu=1}^{N} \phi_{k_\mu} e^{ik_l(z-z')} \chi_{k_\mu}^{\dagger} & z \geq z' \\ \sum_{\mu=1}^{N} \phi_{\bar{k}_\mu} e^{i\bar{k}_\mu(z-z')} \chi_{\bar{k}_\mu^{\dagger}} & z \leq z' \end{cases}$$

where the continuous condition holds at $z{=}z'$ resulting,

$$\sum_{\mu}^{N} \phi_{k_\mu} \chi_{k_\mu}^{\dagger} = \sum_{\mu}^{N} \phi_{\bar{k}_\mu} \chi_{\bar{k}_\mu}^{\dagger}. \tag{4.8}$$

At $z{=}z'$, it satisfies

$$\sum_{\mu=1}^{N} H_{-1} \left[\phi_{k_\mu} e^{-ik_\mu} \chi_{k_\mu}{}^{\dagger} - \phi_{\bar{k}_\mu} e^{-i\bar{k}_\mu} \chi_{\bar{k}_\mu}^{\dagger} \right] = 1 \tag{4.9}$$

using Eqs. 4.6 and 4.8. Combining continuity conditions and Eq. 4.9 we can finally get the solutions for $\chi_{k_\mu}{}^{\dagger}$ and $\chi_{\bar{k}_\mu}{}^{\dagger}$,

$$\chi_{k_\mu}{}^{\dagger} = \tilde{\phi}_{k_\mu}^{\dagger} \xi^{-1}, \overline{\chi}_{k_\mu}{}^{\dagger} = \tilde{\phi}_{\bar{k}_\mu}^{\dagger} \xi^{-1}, \tag{4.10}$$

where

$$\xi = \sum_{\mu=1}^{N} H_{-1} \left[\phi_{k_\mu} e^{-ik_\mu} \tilde{\phi}_{k_l}^{\dagger} - \phi_{\bar{k}_\mu} e^{-i\bar{k}_\mu} \tilde{\phi}_{\bar{k}_l}^{\dagger} \right] \tag{4.11}$$

and $\tilde{\phi}_{k_\mu}^{\dagger} \phi_{k_l} = \tilde{\phi}_{\bar{k}_l}^{\dagger} \phi_{\bar{k}_\mu} = \delta_{\mu l}$

Now the surface Green's function for a semi-infinite electrode can be obtained by applying proper boundary conditions at the end of the electrodes. The left-electrode extended to $z{=}-\infty$ and terminated at $z{=}z_0 - 1$ and the right-electrode extended to

$z=+\infty$ starting from $z=z_0+1$, which requires the condition that Green's function must vanish at $z=z_0$. The surface Green's functions of left (L) and right (R) electrodes which satisfy the boundary condition are

$$\begin{aligned}
g_L &= g_{(z_0-1)(z_0-1)}(z) \\
&= \left[I - \sum_{\mu,l} \phi_{\bar{k}_l} e^{-i\bar{k}_l} \tilde{\phi}^{+}_{\bar{k}_l} \phi_{k_\mu} e^{ik_\mu} \tilde{\phi}^{\dagger}_{k_\mu} \right] \xi^{-1} \\
g_R &= g_{(z_0+1)(z_0+1)}(z) \\
&= \left[I - \sum_{\mu,l} \phi_{k_l} e^{-ik_l} \tilde{\phi}^{+}_{k_l} \phi_{\bar{k}_\mu} e^{i\bar{k}_\mu} \tilde{\phi}^{\dagger}_{\bar{k}_\mu} \right] \xi^{-1}
\end{aligned}$$

Our next step is to consider the coupling between surface Green's function of the electrodes with a scatterer and hence to obtain the total Green's function of the scatterer containing electrodes via Dyson's equation. I will review the technique [145], recursive Green's function technique, which reduce the internal degree of freedom of a scatterer so that describe the scatterer by an effective coupling matrix between the two surfaces.

Let us consider the total Hamiltonian describing a system,

$$H = H_L + H_{LS} + H_S + H_{RS} + H_R, \tag{4.12}$$

In this Hamiltonian H_L and H_R are the Hamiltonians of isolated semi-finite left (L)- and right (R)-electrodes for each, H_{LS} (H_{RS}) is the Hamiltonian describing the coupling between left-electrode (right-electrode) and the scattering region, H_S is for the scattering region. The decimation technique, recursive Green's function technique, can be applied to reduce the internal degree of freedom of the scatterer so that the $H_{LS}+H_S+H_{RS}$ can be described by an effective Hamiltonian H_{eff}.

Suppose $H_{LS}+H_S+H_{RS}$ has N degrees of freedom and electrode surfaces have

M degrees of freedom. Using decimation method the internal degree of freedom of $N \times N$ can be reduced to $M \times M$ matrix by repeating such a step,

$$H_{ij}^{(k)} = H_{ij}^{(k-1)} + \frac{H_{ik}^{(k-1)} H_{kj}^{(k-1)}}{E - H_{kk}^{(k-1)}},$$

for k=$M - N$ times. The resultant effective $M \times M$ Hamiltonian has the following form,

$$H_{eff}(E) = \begin{pmatrix} H_L^*(E) & H_{LR}^*(E) \\ H_{RL}^*(E) & H_R^*(E) \end{pmatrix},$$

where $H_L^*(E)$ and $H_R^*(E)$ describe the intra-surface couplings in left and right surfaces and $H_{LR}^*(E)$ and $H_{RL}^*(E)$ are for the effective coupling between these surfaces.

Finally, we can determine the surface Green function of the whole system containing the scattering attached to semi-infinite electrodes by solving Dyson equation,

$$G(E) = [g(E)^{-1} - H_{eff}(E)]^{-1},$$

where

$$g(E) = \begin{pmatrix} g_L(E) & 0 \\ 0 & g_R(E) \end{pmatrix}.$$

When we consider the scatterer with length L, where perfect electrodes surfaces are located at z=0 and z=L, one has the wave function of electrons which has the following form:

$$\phi_z = \begin{cases} e^{ik_\mu z} \frac{1}{\sqrt{v_\mu}} \phi_{k_\mu} + \sum_l e^{i\bar{k}_l z} \frac{r_{l\mu}}{\sqrt{v_l}} \phi_{\overline{k_l}} & z \le 0 \\ \sum_l e^{ik_l z} \frac{t_{l\mu}}{\sqrt{v_l}} \phi_{k_l} & z \ge L \end{cases}$$

By introducing the projector operator $P_\mu(z') = \xi \phi_{k_\mu} e^{ik_\mu z'} / \sqrt{v_\mu}$, we obtain the components of S matrix,

$$S = \begin{pmatrix} r & t' \\ t & r' \end{pmatrix},$$

where

$$\begin{aligned}
t_{l\mu} &= e^{ik_l L}\sqrt{\frac{v_l}{v_\mu}}\tilde{\phi}^{\dagger}_{k_l} G_{L0}\xi\phi_{k_\mu}, \\
t'_{l\mu} &= e^{i\bar{k}_l L}\sqrt{\frac{v_l}{v_\mu}}\tilde{\phi}^{\dagger}_{\bar{k}_l} G_{0L}\xi\phi_{\bar{k}_\mu}, \\
r_{l\mu} &= \sqrt{\frac{v_l}{v_\mu}}\tilde{\phi}^{\dagger}_{\bar{k}_l}(G_{00}\xi - I)\phi_{k_l}, \\
r'_{l\mu} &= \sqrt{\frac{v_l}{v_\mu}}\tilde{\phi}^{\dagger}_{k_l}(G_{LL}\xi - I)\phi_{\bar{k}_\mu}.
\end{aligned}$$

4.1.2 Non-equilibrium Green's function technique

In the previous section, I have discussed the equilibrium Green's function technique for calculating the scattering matrix and hence the conductance of a system based on the Landauer-Büttiker formula. In that calculation, we assume that our bias voltage is low enough to treat electrons in equilibrium.

In fact, when finite bias voltage is applied to electrodes, the net current flows through the contact and the system is not in thermal equilibrium. Therefore, an advanced method is required to describe a non-equilibrium electronic structure of a nanostructure coupling to external electrodes with different chemical potentials. Also, the dissipation interaction such as electron-electron and electron-phonon interaction need to be described. The non-equilibrium Green's function technique [146] combines quantum transport with a statistical description of such interaction, which has an analogy to Boltzmann equation in classical dynamics.

I used commercially available program package, called as TRANSIESTA [148], to calculate current-voltage characteristics of organic molecules sandwiched between semi-infinite electrodes. This program package makes the use of non-equilibrium

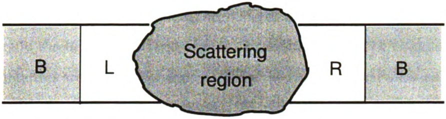

Figure 4.3: Illustration of a reduced system for conductance calculation. The left(L)- and right(R)-electrode Hamiltonians converge to the bulk electrode values. Scattering region is sandwiched between left(L)- and right(R)-electrode which have chemical potentials of μ_L and μ_R, respectively. The Hamiltonians of a scattering region and coupling between a scattering region and left- and right-electrode depend on the non-equilibrium electron density.

Green's function technique to calculate density matrix and conductance properties of a system under a finite bias voltage, which is implemented on SIESTA electronic structure approach [149]. Therefore, the system is described based on the density functional theory: exchange-correlation (XC) functional has been substituted to the local-density approximation (LDA) and the effect of the core electrons is described by soft nonlocal norm-conserving pseudopotentials [150], whereas the linear combination of finite-range numerical atomic orbitals [151] are used to describe the valence states. The assumption in this method is that the commonly used XC functionals are able to describe the electrons in nonequilibrium situation where a current flow is present. This mean field like approximation is not able to describe inelasting scattering process during quantum transport.

Figure 4.1 shows the systems of our interest. The physical system under our consideration is same as the previous one for equilibrium Green's function technique. Our system consists of a conductor connected with two semi-infinite electrodes where a finite bias voltage ΔV is applied. So, the states starting in the left electrodes are filled up to the electrochemical potential of the left electrode μ_L and those in the right electrodes are filled up to μ_R. Here, $e\Delta V = \mu_L - \mu_R$ when $\mu_L > \mu_R$. This is the situation which produces the "non-equilibrium" condition in an electronic subsystem.

The Hamiltonian of left (L)- and right (R)-electrode is assumed to be converged to bulk B values and the coupling between the left and the right electrode takes place only through the scattering region. In order to study the transport properties, our interests are in the three regions, where the Hamiltonian is different from that of bulk values: coupling between left-electrode and a scattering region (L-S), right-electrode and a scattering region (R-S), and scattering region (S). We can reduce our infinite system to a finite L-S-R part (see Fig. 4.3). The L-S-R part of the Green's function G can be obtained by inverting the finite matrix H,

$$H = \begin{pmatrix} H_L + \Sigma_L & V_L & 0 \\ V_L^\dagger & H_S & V_R \\ 0 & V_R^\dagger & H_R + \Sigma_R \end{pmatrix},$$

$G = [EI - H]^{-1}$, where I is the identity matrix. In H matrix, H_L, H_R, and H_S are the Hamiltonian matrices of left- and right-electrode and scattering region. The interaction between the scattering region and the left-electrode is described by V_L and that of the right-electrode is V_R. The coupling of L and R region with the rest of semi-infinite electrodes is fully described by the self-energies, Σ_L and Σ_R, respectively. $H_L + \Sigma_L$ or $H_R + \Sigma_R$ can be evaluated from the calculations for bulk of left and right electrodes. Since it is repeating in z direction, we can use Bloch theorem to evaluate this electrode components. The remaining part of Hamiltonian, V_L, V_R, and H_S depend on the non-equilibrium electron density and are determined by the self-consistent scheme.

In the self-consistent density functional scheme, an effective device potential has following terms: Hartree, exchage-correlation, norm-conserving psedupotentials to describe an atomic core, and other external potentials which can be evaluated using electron density $n(r)$. The electron density can be determined by the density matrix D. When we determine the density matrix of a system, we can solve the Schrödinger equation in conventional DFT scheme. Also, the current can be calculated using

Landauer-Büttiker formula for non-equilibrium condition.

Let us discuss how to build the non-equilibrium density matrix D. The total density matrix D has two parts, the contribution from the left L and the one from the right R [148],

$$D_{\mu\nu} = \int_{-\infty}^{\infty} de \left[\rho_{\mu\nu}^{L}(e) n_F(e-\mu_L) + \rho_{\mu\nu}^{R}(e) n_F(e-\mu_R)\right],$$

where the spectral density matrix ρ^L (ρ^R) can be calculated from retarded self-energy $\Sigma_L(e)$ and the retarded Green's function:

$$\begin{aligned}
\rho_{\mu\nu}^{L}(e) &= \frac{1}{\pi}\left(G(e)\Gamma_L(e)G^{\dagger}(e)\right)_{\mu\nu}, \\
\rho_{\mu\nu}^{R}(e) &= \frac{1}{\pi}\left(G(e)\Gamma_R(e)G^{\dagger}(e)\right)_{\mu\nu}.
\end{aligned}$$

The retarded self-energy Γ_L is evaluated by

$$\Gamma_L = i\left(\Sigma_L(e) - \Sigma_L(e)^{\dagger}\right)/2,$$

where

$$\Sigma_L(e) = \left(V g^L(e) V^{\dagger}\right).$$

Γ_R can be determined in the similar way.

The total density matrix D can be decomposed into equilibrium D^R (D^L) and non-equilibrium Δ^R (Δ^L) part [148]:

$$D_{\mu\nu} = w_{\mu\nu}\left(D_{\mu\nu}^{L} + \Delta_{\mu\nu}^{R}\right) + (1 - w_{\mu\nu})\left(D_{\mu\nu}^{R} + \Delta_{\mu\nu}^{L}\right), \qquad (4.13)$$

where $w_{\mu\nu} = (\Delta_{\mu\nu}^{L})^2 / \left[(\Delta_{\mu\nu}^{L})^2 + (\Delta_{\mu\nu}^{R})^2\right]$. The equilibrium part of the density matrix reads,

$$
\begin{aligned}
D^L_{\mu\nu} &= -\frac{1}{\pi}\mathrm{Im}\left(\int_{E_B}^{\infty} deG(e+i\delta)n_F(e-\mu_L)\right), \\
D^R_{\mu\nu} &= -\frac{1}{\pi}\mathrm{Im}\left(\int_{E_B}^{\infty} deG(e+i\delta)n_F(e-\mu_R)\right), \\
\Delta^L_{\mu\nu} &= \int_{-\infty}^{\infty} de\rho^L_{\mu\nu}(e)\left(n_F(e-\mu_L)-n_F(e-\mu_R)\right), \\
\Delta^R_{\mu\nu} &= \int_{-\infty}^{\infty} de\rho^R_{\mu\nu}(e)\left(n_F(e-\mu_R)-n_F(e-\mu_L)\right),
\end{aligned}
$$

where EB is below the bottom valence-band edge.

Having determined the effective DFT potential, I calculate the Hamiltonian matrix based on SIESTA scheme [149]. Using the non-equilibrium Green's function formalism, the current can be derived as following [148]:

$$
I = G_0 \int_{-\infty}^{\infty} de\left(n_F(e-\mu_L)-n_F(e-\mu_R)\right)\mathrm{Tr}\left(\Gamma_L(e)G(e)^{\dagger}\Gamma_R(e)G(e)\right).
$$

4.2 Microscopic Switching in Molecular Memory Devices

The following discussion on the microscopic switching in molecular memory devices follows that presented in Reference [152].

I study the energetics, electronic structure and electron transport through neutral and charged oligo(phenylene ethylene) molecules within a self-assembled monolayer sandwiched between parallel gold electrodes. Our results indicate that a net charge transfer to the molecules, induced by applying a bias voltage, may shift the balance between the π-system conjugation and the Coulomb repulsion within the system, thus inducing a transition from the stable planar to a less stable twisted isomer. The loss of π-conjugation due to intramolecular twisting causes an increase of the molecular impedance which persists until the structure relaxes to the ground state.

4.2.1 Introduction

With rising interest in self-assembling nanostructures, increasing research effort is being devoted to synthesize nano-switches [153] as building blocks of molecular electronics (moletronics) devices. Recent experimental data suggest that self-assembled monolayers (SAMs) of selected molecules may not only perform a switching function, but also remain in the switched state for many minutes [154]. Possible application of these systems in nonvolatile computer memory appears close at hand in view of the demonstrated fabrication feasibility of dense arrays containing such elements, using a combination of lithography and chemical self-assembly.

4.2.2 Electronic Properties of Isolated Molecules

The switching function reported in Ref. [154] is initiated by applying a 2 V bias voltage across an oligo(phenylene ethynylene) SAM bridging the gap between gold electrodes. As a consequence, the originally conducting system becomes insulating and remains in this state for 800 seconds at room temperature. Neither the physical origin of this memory effect nor the temperature dependence of the current-voltage (I-V) characteristics have been explained yet. I do not suspect a purely electronic origin, such as a deep electron trap with a long lifetime, as the cause in view of the structural floppiness of the system. In this manuscript, I rather investigate a scenario involving a bias-driven structural transition between two isomers with a different I-V characteristics within the SAM.

I propose that for bias voltages below 2 V, the three phenyl rings in the molecule of Fig. 4.4(a) are stabilized in their planar configuration by their conjugated π system which is responsible for their conductance. At higher bias voltages, the interaction with the changing Coulomb field of the surrounding molecules induces a transition to a twisted geometry, associated with a high-impedance state. The persistence of the high-impedance state and the temperature dependence of the I-V characteristics can be traced back to the activated transition between the isomers within this tunable two-level system.

Existing theoretical calculations of molecule-based devices have used molecular orbital calculations at different levels of sophistication [155, 156, 157]. Only in simpler systems, electron transport has been determined using the Landauer-Büttiker formalism [156, 157]. The observed current-voltage (I-V) characteristics of the π-conjugated oligo (phenylene ethynylene) sandwiched between gold electrodes [154] has been related to the character of the lowest unoccupied molecular orbital (LUMO), which changes as a function of the net charge on the molecule [155]. This interpretation relies on a plausibility argument that distinguishes between "conducting" and "insulating" molecular states according to their delocalization across the molecule. The insulator-conductor-insulator transition in oligo (phenylene ethynylene), induced by a bias voltage increase from $0-2$ V [154], has been associated with a net charge trans-

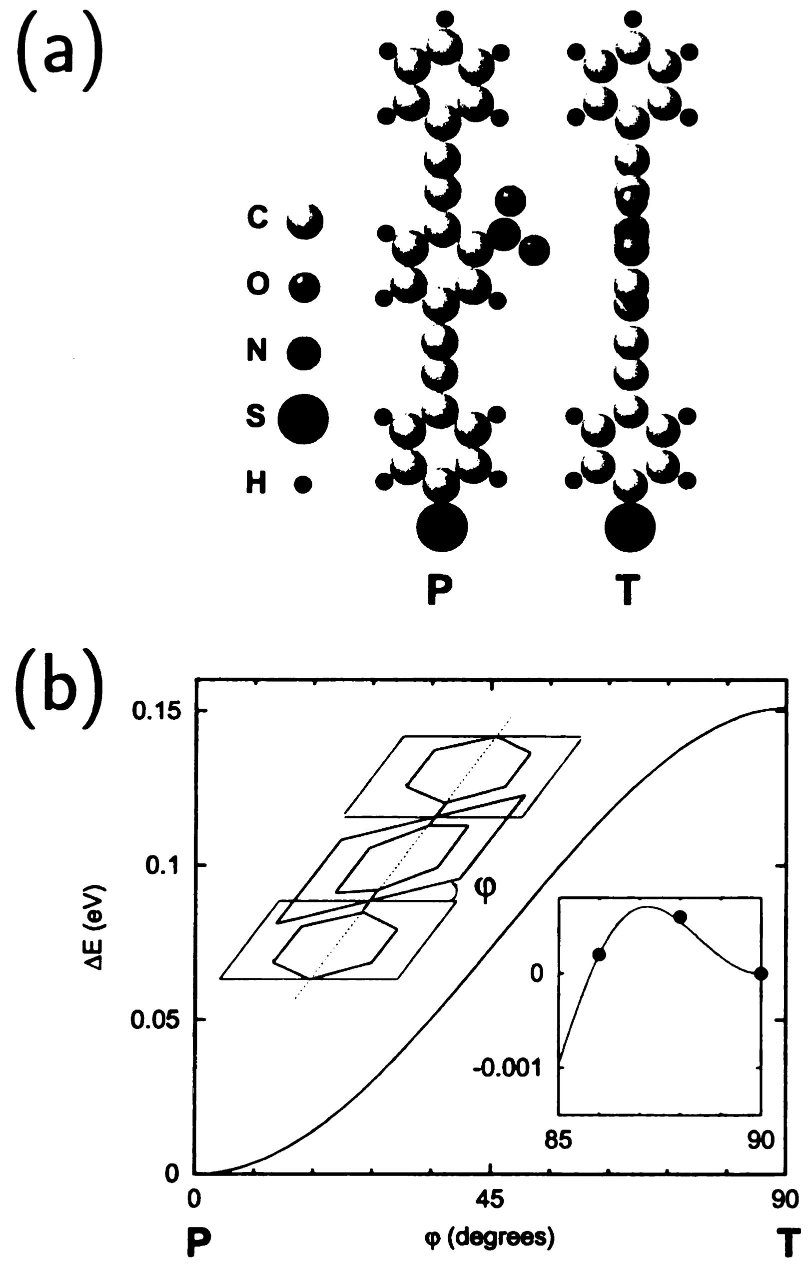

Figure 4.4: (a) Equilibrium structure of the stable planar (P) and metastable twisted (T) isomers of the oligo(phenylene ethynylene) molecule. Only the top and the bottom atoms are connected to the horizontal Au electrodes. (b) Potential energy of the neutral molecule as a function of the rotation of the central phenyl ring. The torsional dihedral angle φ is defined in the inset. The second inset displays the local stability of the T isomer with respect to variations of φ.

fer of up to two electrons to the molecule, thus changing the LUMO character [155]. This approach does not provide a quantitative description of the impedance increase, nor does it address the persistence of the high-impedance state.

To explain quantitatively the conductance changes and the memory effect in an oligo(phenylene ethynylene) SAM sandwiched between gold electrodes, we first described the energetics of the isomer transition using *ab initio* total energy calculations, based on the Density Functional theory (DFT) with generalized gradient corrections (GGA) [158]. To determine the I-V characteristics for the optimized geometries, I combined a parametrized electronic Hamiltonian, which correctly reproduces the states near E_F, with the Landauer-Büttiker formalism for ballistic transport [159, 143].

The isolated oligo (phenylene ethynylene) molecule, depicted in Fig. 4.4(a), belongs to the group of twisted intramolecular charge transfer (TICT) molecules [161]. In TICT systems, transitions between planar (P) and twisted (T) isomer states are induced by a changing balance between the strength of the π-electron conjugation, stabilizing the P state, and the Coulomb repulsion that stabilizes the T state. As I will discuss in the following, it is the loss of π electron conjugation during the P→T transition which is responsible for the conductance reduction. In Fig. 4.4(b), I show the energy of an isolated oligo(phenylene ethynylene) molecule as a function of the torsional dihedral angle φ. The results shown are for DFT-optimized geometries for a given value of φ. Our results show the P isomer, associated with $\varphi = 0°$, to be most stable. Even though the T isomer at $\varphi = 90°$ is also locally stable (albeit with an insignificant energy barrier of 0.5 meV), we can not identify an intramolecular mechanism that would induce the P→T transition, associated with an energy cost of 0.15 eV. In the particular system considered here, as I show below, the P→T transition may be induced by a torque acting on the polar central phenyl ring, caused by the changing Coulomb field of the surrounding molecules within the SAM.

Cyclic voltammetry measurements [160] indicate that the oligo(phenylene ethynylene) molecules within the SAM remain neutral for bias voltages $V_{bias} < 1.5$ V, but acquire a net charge $Q = -1\,e$ for 1.5 V$< V_{bias} < 2.0$ V and $Q = -2\,e$ for $V_{bias} > 2.0$ V. I find that the electronegative NO_2 radical induces a dipole moment in the central phenyl ring, normal to the long molecular axis. Nearly independent of the net molecular charge, the two oxygen atoms of this radical carry a net charge $Q_O \approx -1.1\ e$ each.

Consequently, we should consider the energetics within the entire SAM, consisting of an ordered layer of the oligo(phenylene ethynylene) molecules bridging the spacing between two aligned Au(001) surfaces [153, 154, 155]. The molecule ends are terminally attached to Au surface atoms. The close-packed ordered 2×2 overlayer, shown schematically in Fig. 4.5(a), has a nearest neighbor spacing $a = 8.16$ Å, twice the lattice constant of Au.

With the terminal phenyl rings anchored in the gold surface, an additional torque due to the surrounding charges, acting on the central phenyl ring carrying a large dipole, may change its orientation and thus modify the dihedral angle φ, as shown in Fig. 4.5(a). For a given *total charge* Q_{tot} of each molecule, which can be linked to the applied bias voltage, I consider a net charge $Q_O = -1.1\ e$ to reside on each of the oxygen atoms which are separated by ≈3.3 Å from the molecular axis. The remaining charge $Q_r = Q_{tot} - 2Q_O$ is distributed along the rest of the molecule. The energetics of this system of charges as a function of the dipole orientation ϕ is depicted in Fig. 4.5(b) for different values of the total charge Q_{tot}.

Even though the energy of aligned point dipoles on a square lattice is independent of the dipole orientation ϕ, the assumption of point dipoles becomes invalid once the size of the physical dipole becomes comparable to the intermolecular spacing. In this case, I find that molecules carrying $Q_{tot} = 0$ net charge tend to align along $\phi = 0°$ or $\phi = 90°$ due to the dominating Coulomb attraction between the oxygens and

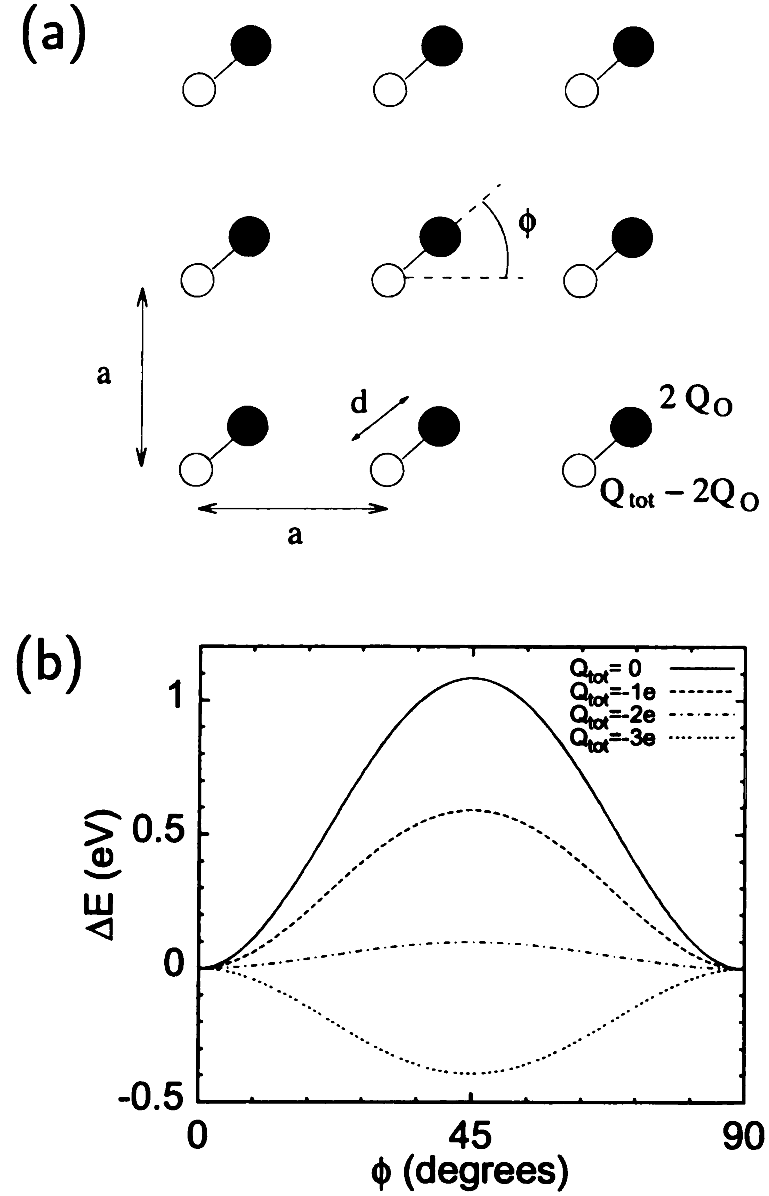

Figure 4.5: (a) Schematic top view of the SAM. The molecules, forming a square lattice on the electrodes, carry a net charge Q_{tot}. Their orientation ϕ relative to the lattice is strongly affected by the interaction of the dipoles consisting of the charge pair $+2Q_O$, $-2Q_O$, separated by the distance d, with the surrounding charges. (b) Potential energy of this dipole layer as a function of the dipole orientation ϕ, presented for different values of the total charge Q_{tot}.

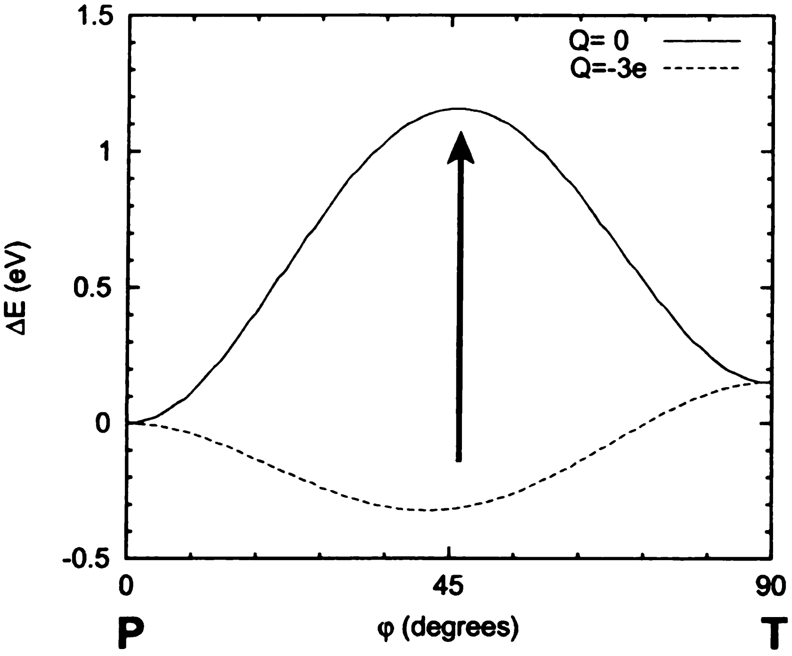

Figure 4.6: Total energy of an oligo(phenylene ethynylene) molecule as a function of the torsional dihedral angle φ, containing both the intramolecular strain and dipole-dipole interactions within the SAM.

the positively charged skeletons of the neighboring molecules. Combined with the fact that the P isomer with zero dihedral angle is most stable, I may assume that the neutral molecules become anchored in the gold electrodes with also the terminal phenyl rings aligned along along $\phi = 0°$ or $\phi = 90°$. I will also assume that once the terminal phenyl rings are attached in this way, they can no longer change their orientation. In this case, only the central phenyl rings may eventually rotate within the SAM.

Only as the net charge Q_{tot} exceeds two extra electrons, the interaction between the oxygens and the skeletons of the neighboring molecules becomes sufficiently repulsive to energetically favor the $\phi = \varphi = 45°$ orientation of the dipoles. As the Coulomb energy gain associated with this rotation exceeds the energy cost of the intramolecular twist, the molecules within the SAM will twist to a nonzero dihedral angle $\varphi \approx 45°$, thus disrupting the π electron system conjugation. The energetics of this transition is shown in Fig. 4.6. Should the extra charge be removed abruptly, the twisted state becomes unstable, as indicated by the solid arrow in Fig. 4.6. In this case, the intramolecular Coulomb repulsion can take over and complete the internal twist, thus relaxing the system to the metastable T state. Transition from the T state back to the equilibrium P state is a thermally activated process that involves crossing the activation barrier depicted in Fig. 4.4(b). More important, this relaxation is sterically hindered by the presence of surrounding molecules within the SAM, thus causing a time delay which lies at the origin of the memory effect.

My understanding of the bias-driven isomer transitions within the SAM derives from the interrelationship between the net charge Q_{tot} on the molecules and the applied bias voltage V_{bias}. I find that when packed in a SAM, oligo(phenylene ethynylene) molecules carrying less than one extra electron remain in (and eventually return to) the equilibrium P state with an intact π electron system conjugation for $\varphi = 0°$. This situation is associated with bias voltages $V_{bias} < 2$ V. As the molecule acquires more than two extra electrons, corresponding to $V_{bias} > 2$ V, the intra- and intermolecular Coulomb repulsion becomes dominant, thus inducing a transition to the metastable T state at $\varphi = 90°$. The deexcitation to the equilibrium $\varphi = 0°$ state is a thermally activated process that is slowed down by the steric hindrance within the SAM.

4.2.3 Quantum Transport through Molecules

After characterizing possible structural changes that may be induced in this two-level system by applying a bias voltage, I discuss in the following the effect of molecular structure changes on the conductance. We use the Landauer-Büttiker formalism [159, 143] to evaluate the electron transport through an oligo(phenylene ethylene) molecule in its two isomer states in the ballistic regime. In our calculation, we treat the molecule as a scattering region sandwiched between two semi-infinite gold leads. We use a recursive Greens function formalism to evaluate the transmission

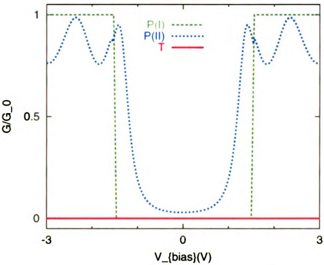

Figure 4.7: Conductance G of the molecule in units of the conductance quantum $G_0 = 2e^2/h \approx (12.9\ \mathrm{k}\Omega)^{-1}$ as a function of bias voltage. The effect of Au leads is modeled by either a periodic chain of P isomers (denoted P(I)) or by model conductors which minimize the contact resistance (denoted P(II)). The P isomer conducts only for $V_{bias} > 1.5$ V, whereas the T isomer is always insulating.

matrix $\mathbf{t}$, describing the scattering of electrons of energy $E = E_F + eV_{bias}$ from one semi-infinite lead to the other. The differential electrical conductance at the bias voltage V_{bias} is then related to the scattering properties by the Landauer-Büttiker formula[159, 143] $G = G_0 Tr\left\{\mathbf{t}^\dagger \mathbf{t}\right\}$, where $G_0 = 2e^2/h$ is the conductance quantum.

In view of the fact that the conductance behavior of the system depends significantly also on the (currently unknown) nature of the contacts, we use a simplified Hamiltonian to describe the electronic structure of the molecule. Our DFT calculations show that the electronic states near the Fermi level, corresponding to the frontier orbitals, are dominated by the $pp\pi$ hybrids of the carbon skeleton. The Hückel model we use to describe transport through these states, characterized by $E_p = 0$ eV and $V_{pp\pi} = -2.67$ eV, not only reproduces the electronic structure near E_F, but also makes the conductance calculation numerically tractable. Moreover, the transparency of the model allows us to discuss the general behavior of related systems.

The results of our conductance calculation are presented in Fig. 4.7 as a function of the bias voltage V_{bias} for the P and T isomers. We have compared these results with those of a four-state Linear Combination of Atomic Orbitals Hamiltonian, with parameters based on *ab initio* calculations [162], and found very little difference, justifying our approach. As mentioned above, the exact nature of the contacts between the molecule and the electrodes is unknown. In our calculation, which is based on two very different points of view, we model the effect of the Au leads by either a periodic chain of P isomers (denoted as P(I)) or by model conductors which minimize the contact resistance (denoted as P(II)).

We notice that independent of the model used for the leads, the T isomer is insulating independent of the applied bias voltage. The same insulating behavior occurs also for the P isomer for bias voltages $V_{bias} < 1.5$ V, in agreement with results of Ref. [154]. Depending on the leads connected to the molecule, we also find a drastic conductance increase for bias voltages > 1.5 V, in good agreement with the experimental observation. At bias voltages exceeding 2 V, we explain the observed sudden increase in the impedance by the $P \rightarrow T$ isomer transition. The persistence of the insulating state for many minutes is explained by the slow speed of the $T \rightarrow P$ deexcitation.

My description of the microscopic processes that are likely to occur in an oligo(phenylene ethylene) molecule sandwiched between gold electrodes has interesting consequences on its conductance behavior upon modifying the system. Adding neutral, nonpolar "spacer" molecules in the SAM should reduce the torque on the central phenyl ring that is induced by the surrounding molecules, thus requiring a higher bias voltage to initiate the intramolecular $P \rightarrow T$ twist causing persistent conductance loss. Since the inter-molecular Coulomb interaction should also depend on the molecular arrangement within the SAM, a change from a square to a triangular packing, induced by using a Au(111) surface instead of Au(001), should also modify the I-V characteristics of the device. Adding an extra NO_2 group opposite to the first NO_2 group attached to the central phenyl ring should strongly reduce the dipole moment of this molecule and thus inhibit or delay the $P \rightarrow T$ transition. The critical bias voltage required to induce an isomer transition should also be reduced when substituting NO_2 by a less electronegative radical. Radicals creating a larger dipole moment normal to the main molecular axis, on the other hand, should reduce the critical bias voltage needed to switch the conductance state. Substituting hydrogen by neutral radicals at the phenyl rings should not modify the I-V characteristics significantly as long as these radicals do not perturb the π-electron system. Finally, similar switching and memory behavior is expected when using other TICT molecules to bridge the gap between two metal electrodes.

4.2.4 Current-Voltage (IV) Characteristics

As I described above, the equilibrium Green's function technique combined with tight-binding Hamiltonian has been used to calculate the conductance of oligo molecules as a function of bias voltage. The geometry used for conductance calculations consisted of carbon atoms only, connected to Au electrodes. Since π electrons in the system plays an important role in the conductance properties, our results give insight into the observed switching behavior.

An advanced technique is required in the following sense. First, to study the current-voltage characteristics of systems we should be able to describe the non-equilibrium situation where a finite bias voltage is applied. Also, a better description of the many-body system is required, especially to study the effects of side groups in our interest. Under this requirement I used the non-equilibrium Green's function technique combining with the DFT scheme, as implemented in the TRANSIESTA code [148]. This technique has been applied to many physical systems [164], which successfully describe the transport properties of system comparing to experimental

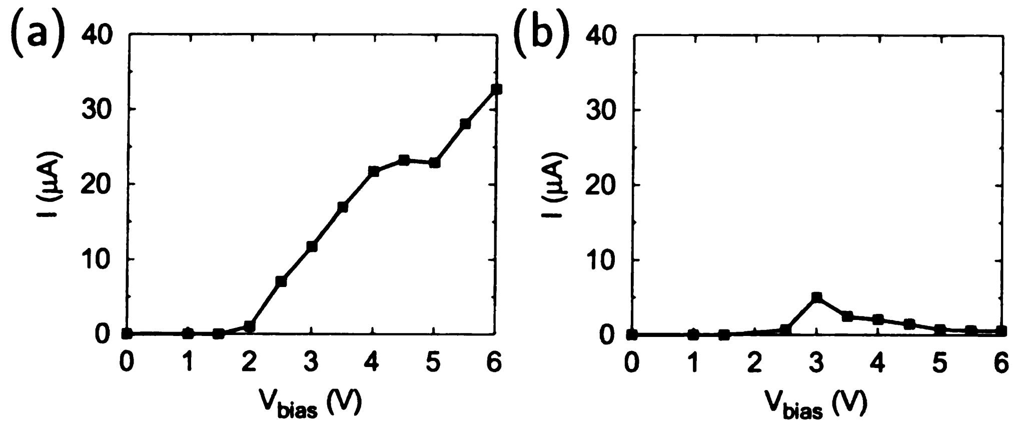

Figure 4.8: Current-Voltage (IV) characteristics of three phenyl ring molecules of planar (P) (a) and 90 degree twisted (T)(b) structure of middle ring. The results show the linear increase of current as a function of bias voltage for P geometry and it shows low conductance state for T geometry.

observations.

I considered the IV characteristics of three phenyl rings, which are connected to infinite phenyl rings. So, my electrode is described as semi-infinite phenyl rings instead of Au electrode, which was used in experiments. Figure 4.8 shows the IV characteristics of three phenyl ring molecules with planar (a) or 90 degree twisted (b) geometry. As observed experimentally, my results show that the planar geometry is in high conducting state and the twisted geometry is in low conducting state. In contrast to the results using equilibrium Green's function combined with tight-biding Hamiltonian, which show complete block of conductance channel in twisted geometry (Fig. 4.7), current results show low-conducting behavior (Fig. 4.8 (b)). Since only π electron contribute to the conductance in previous calculation, the rotating of middle ring will completely block the conductance channel, which results insulating state.

Not only the three phenyl ring molecules but also the molecules with different side groups in the middle ring have been considered. Depending on the side group, NDR or memory effects has been strongly affected. Experimentally, the devices which contain nitroamine in the center and only nitro group show NDR and switching behavior. On the other hand, the devices with no nitro group, either only amino group or only phenyl rings have no NDR and switching behavior. So, experimental group concludes that the nitro group is responsible for NDR and switching behavior [163].

To study the effects of side groups I calculated the transport IV characteristics of our oligo molecules with different side groups. In my calculation, semi-infinite electrodes are described as a infinite phenyl ring instead of Au electrode. The results are shown in Fig. 4.9. The devices containing nitro group (Fig. 4.9 (b)) and nitroamine (Fig. 4.9 (c)) show NDR in IV characteristics. On the other hand the device with amino group shows monotonic increase of current as a function of bias voltage. Also, as I rotate the middle ring of the structure, it becomes to be in a low-conducting state as shown in Fig. 4.9 (d). My results are quite well consistent with experimental observations. Those behavior can be explained by monitoring the transmission coefficients as a function of bias voltage.

4.2.5 Summary

In summary, I studied the electronic and transport properties of oligo (phenylene ethylene) molecules within a self-assembled monolayer, which experimentally found to be an interesting system which shows memory and switching behavior in current-voltage characteristics.

I used various techniques, density functional theory and equilibrium and nonequilibrium Green's function technique to determine the energetics and transport properties of neutral and charged oligo (phenylene ethylene) molecules within a self-assembled monolayer.

I found that a net charge transfer to the molecule, induced by an applied bias voltage, may shift the balance between the strength of the π-system conjugation, favoring a planar geometry, and and intra- and intermolecular Coulomb repulsion favoring an intramolecular twist. As the twisted geometry with a disrupted and hence non-conducting π-electron system constitutes a metastable state of the molecule,

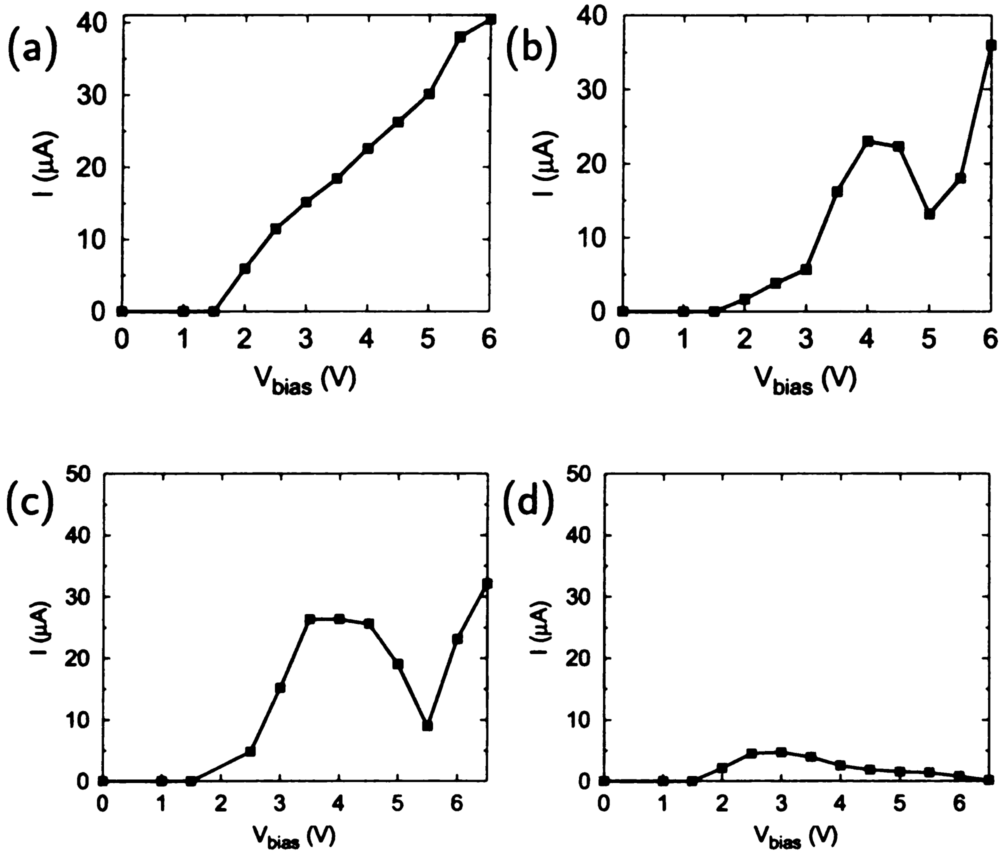

Figure 4.9: IV characteristics of three phenyl ring molecules with amino-group in the middle ring (a), nitro-group in the middle ring (b), and nitro and amino-group in the middle ring (c)-(d). The molecules without any nitro-group show linear increase of current as a function of bias voltage, whereas negative differential resistance (NDR) behavior has been observed for the molecules with nitro-groups in the middle ring.

the transition to the planar geometry takes place through thermal activation and is delayed due to the steric hindrance caused by the surrounding molecules within the SAM. The IV characteristics calculated from nonequilibrium Green's function technique show that nitro group is responsible for NDR behavior, which is consistent with experimental observation. The side-group dependence behavior can be explained by monitoring the transmission coefficient as a function of bias voltage.

BIBLIOGRAPHY

BIBLIOGRAPHY

[1] S. Berber, Y.-K. Kwon, and D. Tománek, Phys. Rev. Lett. **88**, 185502 (2002).

[2] Y.-K. Kwon *et al.*, Phys. Rev. Lett. **79**, 2065 (1997).

[3] Y.-K. Kwon, D. Tománek, and S. Iijima, Phys. Rev. Lett. **82**, 1470 (1999).

[4] S. G. Kim and D. Tománek, Phys. Rev. Lett. **72**, 2418 (1994).

[5] N. Troullier and J. L. Martins, Phys. Rev. B. **43**, 1993 (1991).

[6] L. Kleinman, and D. M. Bylander, Phys. Rev. Lett. **48**, 1425 (1982).

[7] O. F. Sankey and D. J. Niklewski, Phys. Rev. B **40**, 3979 (1989).

[8] N. Park *et al.*, Phys. Rev. B **65**, 121405 (2002).

[9] P. Ordejón, E. Artacho and J. M. Soler, Phys. Rev. B **53**, R10441 (2000); D. Sánchez-Portal, P. Ordejón, E. Artacho, and J. M. Soler, Int. J. Quantum Chem. **65**, 453 (1997).

[10] R. H. Boyd, S. N. Sanwal, S. Shary-Tehrany, D. McNally, J. Phys. Chem. **75**, 1264 (1971).

[11] J. E. Dahl, S. G. Liu and R. M. K. Carlson, Science **299**, 96 (2003).

[12] J.Y. Raty , G. Galli, C. Bostedt, T.W. van Buuren, and L.J. Terminello, Phys. Rev. Lett. **90**, 037401 (2003).

[13] J.Y. Raty and G. Galli, Nat. Mat. **2**, 792 (2003).

[14] D. M. Ceperley, and B. J. Alder, Phys. Rev. Lett. **45**, 566 (1980).

[15] J. P. Perdew, and A. Zunger, Phys. Rev. B. **23**, 5048 (1981).

[16] O. F. Sankey and D. J. Niklewski, Phys. Rev. B. **40**, 3979 (1989).

[17] N. Park, K. Lee, S. Han, J. Yu, and J. Ihm, Phys. Rev. B **65**, 121405(R) (2002).

[18] P. Hohenberg and W. Kohn, Phys. Rev. **136**, B864 (1964).

[19] W. Kohn and L. J. Sham, Phys. Rev. **140**, A1133 (1965).

[20] N. W. Aschroft and N. D. Mermin, *Solid State Physics*, 2nd edition (Harcourt, Inc., 1976).

[21] E. Hückel, Z. Physik **70**, 204 (1931).

[22] W. Wolfsberg and L. Helmholtz, J. Chem. Phys. **20**, 837 (1952).

[23] R. Hoffmann, J. Chem. Phys. **39**, 1397 (1963).

[24] W. Zhong, D. Tománek, and G. F. Bertsch, Solid State Comm. **86**, 607 (1993).

[25] J. D. Joannopoulos and F. Yndurain, Phys. Rev. B **10**, 5164 (1974).

[26] J. C. Slater and G. F. Koster, Phys. Rev. **94**, 1498 (1954).

[27] Y. K. Kwon, *ph.D thesis*, Michigan State University.

[28] D. Tománek and S. G. Louie, Phys. Rev. B **37**, 8327 (1988).

[29] D. Tománek, C. Sun, N. Sharma, and L. Wang, Phys. Rev. B **39**, 5361 (1989).

[30] D. Tománek and M. A. Schluter, Phys. Rev. Lett. **67**, 2331 (1991).

[31] M. Yoon, S. Berber, D. David Tománek (submitted for publication)

[32] H. W. Kroto *et al.*, Nature (London) **318**, 162 (1985).

[33] S. Iijima, Nature (London) **354**, 56 (1991).

[34] B. W. Smith, M. Monthioux, and D. E. Luzzi, Nature **396**, 323 (1998).

[35] K. Hirahara *et al.*, Phys. Rev. Lett. **85**, 5384 (2000).

[36] D. L. Dorset and J. R. Fryer, J. Phys. Chem. B **101**, 3968 (1997); H. Kawada *et al.*, Phys. Rev. B **51**, 8723 (1995); Y. Saito *et al.*, Phys. Rev. B **48**, 9182 (1993); R. Beyers *et al.*, Nature **370**, 196 (1994).

[37] B. W. Smith *et al.*, J. Appl. Phys. **91**, 9333 (2002).

[38] K. Hirahara *et al.*, Phys. Rev. B **64**, 115420 (2001).

[39] The encapsulation energy ΔE is defined as the energy of a single fullerene encapsulated in a particular nanotube, with respect to the non-interacting reference system. Consequently, ΔE does not depend on the precise geometry or termination of the open nanotube edge.

[40] S. Okada, S. Saito, A. Oshiyama, Phys. Rev. Lett. **86**, 3835 (2001).

[41] H. Ulbricht, G. Moos, and T. Hertel, Phys. Rev. Lett. **90**, 095501 (2003).

[42] Yang Wang, D. Tománek, and G. F. Bertsch, Phys. Rev. BR **44**, 6562 (1991).

[43] D.M. Eigler and E.K. Schweizer, Nature **344**, 524 (1990); J.A. Stroscio and D.M. Eigler, Science **254**, 1319 (1991).

[44] Y. Nakayama, H. Nishijima, S. Akita, K. I. Hohmura, S. H. Yoshimura, and K. Takeyasu, J. Vac. Sci. Techn. B **18**, 661 (2000).

[45] M. Hodak and L. A. Girifalco, Phys. Rev. B **67**, 075419 (2003).

[46] S. Okada, M. Otani, and A. Oshiyama, Phys. Rev. B **67**, 205411 (2003).

[47] B. W. Smith and D. E. Luzzi, Chem. Phys. Lett. **321**, 169 (2000).

[48] S. Bandow *et al.*, Chem. Phys. Lett. **337**, 48 (2001).

[49] K. P. Meletov *et al.*, Chem. Phys. Lett. **341**, 435 (2001).

[50] V. D. Blank *et al.*, Phys. Lett. A **205**, 208 (1995).

[51] G. C. McIntosh M. Yoon, S. Berber, and D. Tománek, Phys. RevḂ (2004).

[52] S. Han, M. Yoon, S. Berber, N. Park, E. Osawa, J. Ihm, D. David Tománek (submitted for publication)

Chem. Phys. Lett. **337**, 48 (2001).

[53] C. Ronchi *et al.*, Int. J. of Thermophysics **13**, 107 (1992).

[54] T.L. Makarova *et al.*, Nature (London) **413**, 716 (2001).

[55] Y.-H. Kim *et al.*, Phys. Rev. B **68**, 125420 (2003).

[56] E. Osawa *et al.*, J. Chem. Soc. Perk. Trans. 2, 943 (1998).

[57] Y.-H. Kim *et al.*, Phys. Rev. Lett. **90**, 65501 (2003).

[58] A. J. Stone and D. J. Wales, Chem. Phys. Lett. **128**, 501 (1986).

[59] Y. F. Zhao, B. I. Yakobson, and R. E. Smalley, Phys. Rev. Lett. **88**, 185501 (2002); Y. F. Zhao, R. E. Smalley, and B. I. Yakobson, Phys. Rev. B **66**, 195409 (2002).

[60] A. M. Rao *et al.*, Appl. Phys. A **64**, 231 (1997).

[61] K. Honda *et al.*, Fullerene Science and Technology **4**, 819 (1996); S. Osawa, M. Sakai, and E. Osawa, J. Phys. Chem. A **101**, 1378 (1997).

[62] H. Ueno *et al.*, Fullerene Science and Technology **6**, 319 (1998).

[63] W. E, W. Ren, and E. Vanden-Eijnden, Phys. Rev. B **66**, 052301 (2002).

[64] For the sake of comparison, we also calculated the activation barrier for a GSW transformation in a graphene sheet and obtained a much larger value of $\approx$9 eV, which compares well with the published value of $\approx$8 eV based on *ab initio* calculations of E. Kaxiras and K. C. Pandey, Phys. Rev. Lett. **61**, 2693 (1988).

[65] B. R. Eggen *et al.*, Science **272**, 87 (1996).

[66] Z. Slanina *et al.*, J. Organomet. Chem. **599**, 57 (2000).

[67] F. Banhart, Rep. Prog. Phys. **62**, 1181 (1999).

[68] H.F. Bettinger, B.I. Yakobson, and G.E. Scuseria, J. Am. Chem. Soc. **125**, 5572 (2003).

[69] R. L. Murry *et al.*, Nature **366**, 665 (1993); G. E. Scuseria, Science **271**, 942 (1996); E. Osawa *et al.*, Fullerene Science and Technology **6**, 259 (1998).

[70] The Arrhenius formula determines the reaction rate as $\nu \exp(-\Delta E/k_B T)$, where ν is the attempt frequency, ΔE the activation barrier, k_B the Boltzmann constant, and T the temperature.

[71] P.A. Heiney, J.E. Fischer, A.R. McGhie, W.J. Romanow, A.M. Denenstein, J.P. McCauley Jr., A.B. Smith III, and D.E. Cox, Phys. Rev. Lett. **66**, 2911 (1991).

[72] T. Okazaki *et al.*, J. Am. Chem. Soc. **123**, 9673 (2001).

[73] M. Yoon *et al.* Phys. Rev. Lett. **92**, 075504 (2004).

[74] H. W. Kroto *et al.*, Nature (London) **318**, 162 (1985).

[75] S. Iijima, Nature (London) **354**, 56 (1991).

[76] M. Terrones *et al.*, Science **288**, 1226 (2000).

[77] S. Bandow *et al.*, Chem. Phys. Lett. **337**, 48 (2001).

[78] H. Ueno, S. Osawa, E. Osawa, and K. Takeuchi, Fullerene Science and Technology **6**, 319 (1998).

[79] E. Osawa and K. Honda, Fullerene Science and Technology **4**, 939 (1996); A. J. Stone and D. J. Wales, Chem. Phys. Lett. **128**, 501 (1986).

[80] P. W. Fowler and D. E. Manolopoulos, *An Atlas of Fullerenes* (Clarendon, Oxford, 1995); E. Osawa *et al.*, J. Chem. Soc. Perkin Trans. **2**, 943 (1998).

[81] Y. F. Zhao, B. I. Yakobson, and R. E. Smalley, Phys. Rev. Lett. **88**, 185501 (2002); Y. F. Zhao, R. E. Smalley, and B. I. Yakobson, Phys. Rev. B **66**, 195409 (2002).

[82] D. Tománek, W. Zhong, and E. Krastev. Phys. Rev. B **48**, 15461 (1993); D. H. Robertson, D. W. Brenner, and J. W. Mintmire, Phys. Rev. B **45**, 12592 (1992).

[83] D. Tománek and M. A. Schluter, Phys. Rev. Lett. **67**, 2331 (1991).

[84] W. Press, T. Teukolsky, W. T. Vetterling, and B. P. Flannery, *Numerical Recipes* (Cambridge Univ. Press, 1986).

[85] W. E, W. Ren, and E. Vanden-Eijnden, Phys. Rev. B **66**, 052301 (2002).

[86] F. Banhart, Rep. Prog. Phys. **62**, 1181 (1999).

[87] B. R. Eggen *et al.*, Science **272**, 87 (1996).

[88] Z. Slanina *et al.*, J. Organometal. Chem. **599**, 57 (2000).

[89] E. Kaxiras and K. C. Pandey, Phys. Rev. Lett. **61**, 2693 (1988).

[90] M. Buongiorno Nardelli, B. I. Yakobson, and J. Bernholc, Phys. Rev. Lett. **81**, 4656 (1998) and Phys. Rev. B **57**, R4277 (1998); P. Zhang, P. E. Lammert, and V.H. Crespi, Phys. Rev. Lett. **81**, 5346 (1998).

[91] C. Journet *et al.*, Nature **388**, 756 (1997).

[92] P. Nikolaev *et al.*, Chem. Phys. Lett. **313**, 91 (1999).

[93] Y.-K. Kwon and D. Tománek, Phys. Rev. Lett. **84**, 1483 (2000).

[94] Presentation of Richard P. Feynman at the annual meeting of the American Physical Society at the California Institute of Technology on December 29, 1959. Reprinted in "The Pleasure of Finding Things Out", edited by J. Robbins (Perseus Books, 1999).

[95] K. E. Drexler, Scientific American **285**, 74 (2001).

[96] G. I. Leach, R. C. Merkle, Nanotechonology **5**, 168 (1994).

[97] G. Leach, Nanotechnology **7**, 197 (1996).

[98] P. R. von Schleyer, J. Am. Chem. Soc. **79**, 3292 (1957).

[99] W. H. Bragg, W. L. Bragg, Nature **91**, 554 (1913).

[100] C. Cupas, P. R. von Schleyer, D. J. Trecker, J. Am. Chem. Soc. **87**, 917 (1965).

[101] V. Z. Williams Jr., P. R. von Schleyer, G. J. Gleicher, L. B. Rodewald, J. Am. Chem. Soc. **88**, 3362 (1966).

[102] D. Farcasiu, H. Bohm, P. R. von Schleyer, J. Organic Chem. **42**, 96 (1977).

[103] G. A. Mansoori, J. Petrol. Science & Eng. **17**, 101 (1997).

[104] D. Vazquez Gurrola, J. Escobedo, G. A. Mansoori, "Characterization of Crude Oils from Southern Mexican Oil Fields", in EXITEP 1998 Proceedings, Mexico City, Mexico.

[105] J. Reiser, E. McGregor, J. Jones, R. Enick, G. Holder, Fluid Phase Equilibria **117**, 160 (1996).

[106] J. E. Dahl, J. M. Moldowan, K. E. Peters, G. E. Claypool, M. A. Rooney, G. E. Michael, M. R. Mello, M. L. Kohnen, Nature **399**, 54 (1999).

[107] G. C. McIntosh, D. Tománek, and Y. W. Park, Phys. Rev. B **67**, 125419 (2003).

[108] We found a significant energy difference between the presently used double-zeta and the minimum basis set. Based on calculations for the related ethylene molecule, using a triple-zeta basis would change the binding energy per atom by ≤ 3 meV.

[109] C. Kittel, *Introduction to Solid State Physics* (Wiley, New York, 1996).

[110] To limit the computational effort associated with a large number of degrees of freedom, we kept the atomic arrangement within interacting diamondoids frozen in the optimum geometry when determining the total energy of the interacting system. Due to the suppression of relaxations, our estimates provide only a lower limit on the binding energy.

[111] C. E. Nebel, Semicond. Sci. Technol. **18**, S1 (2003).

[112] We use the values $E_{tot}(\mathrm{C}) = -154.35$ eV for the total energy of diamond per atom, and $E_{tot}(\mathrm{H_2}) = -30.54$ eV for the total energy of a hydrogen molecule, based on the same computational approach and basis as applied to the diamondoids.

[113] Johan F. Prins, Semicond. Sci. Technol. **18**, S125 (2003).

[114] To limit the computational effort, we chose diamantane as a representative of elongated building blocks.

[115] D. Golberg, Y. Bando, W. Han, K. Kurashima, and T. Sato, Chem. Phys. Lett. **308**, 337 (1999).

[116] H. Zhang and M. Widom, Phys. Rev. E **49**, R3591 (1994); J. Mag. Mag. Mat. **122**, 119 (1993).

[117] K. Raj, B. Moshowitz, and R. Casciari, J. Magn. Mag. Mat. **149**, 174 (1995).

[118] Hao Wang *et al.*, Phys. Rev. Lett. **72**, 1929 (1994).

[119] A. J. Dickstein *et al.*, Science **261**, 1012 (1993).

[120] Chin-Yih Hong *et al.*, J. Appl. Phys. **81**, 4275 (1997).

[121] M. Yoon and D. Tománek (in preparation).

[122] We define $\hat{x}$ as the the directional unit vector.

[123] J.D. Jackson, *Classical Electrodynamics*, 2nd edition (John Wiley, New York, 1975).

[124] Dongqing Wei and G. N. Patey, Phys. Rev. Lett. **68**, 2043 (1992); R. Tao and J. M. Sun, Phys. Rev. Lett. **67**, 398 (1991); D. J. Klingenberg, Frank van Swol, and C. F. Zukoski, J. Chem. Phys. **91**,7888 (1989).

[125] P. Jund, S. G. Kim, D. Tománek, and J. Hetherington Phys. Rev. Lett. **74**, 3049 (1995).

[126] A. S. Clarke and G. N. Patey J. Chem. Phys. **100**, 2213 (1994).

[127] C. F. Tejero, A. Daanoun, H. N. W. Lekkerkerker, and M. Baus, Phys. Rev. Lett. **73**, 752 (1994).

[128] M. Yoon, P. Borrmann, S. G. Kim, P. Jund, and D. Tománek (in preparation).

[129] Hao Wang *et al.*, Phys. Rev. Lett. **72**, 1929 (1994).

[130] P. Jund, S. G. Kim, D. Tománek, and J. Hetherington, Phys. Rev. Lett. **74**, 3049 (1995).

[131] Akiva J. Dickstein *et al.*, Science **261**, 1012 (1993).

[132] J. J. Weis and D. Levesque, Phys. Rev. E **48**, 3728 (1993); D. Levesque and J. J. Weis, Phys. Rev. E **49**, 5131 (1994).

[133] A. S. Clarke and G. N. Patey, J. Chem. Phys. **100**, 2213 (1994).

[134] Holly B. Lavender, Karthik A. Iyer, and Sherwin J. Singer, J. Chem. Phys. **101**, 7856 (1994).

[135] Thomas C. Halsey and Will Toor, Phys. Rev. Lett. **65**, 2820 (1990); Thomas C. Halsey, James E. Martin, and Douglas Adolf, Phys. Rev. Lett. **68**, 1519 (1992); Thomas C. Halsey, Phys. Rev. E **48**, R673 (1993).

[136] R. Tao and J. M. Sun, Phys. Rev. Lett. **67**, 398 (1991).

[137] Peter Borrmann *et al.*, J. Chem. Phys. **111**, 10689 (1999).

[138] Patent application pending, Deutsches Patentamt, Munich (1996).

[139] W. Press, T. Teukolsky, W. T. Vetterling, and B. P. Flannery, *Numerical Recipes* (Cambridge Univ. Press, 1986).

[140] H. Goldstein, *Classical Mechanics*, 2nd edition (Addison Wesley, 1980).

[141] D. Tománek *et al.*, Z. Phys. D **40**, 539 (1997).

[142] In clinical studies, magnetic fields commonly used in Magnetic Resonance Imaging (MRI), up to 2×10^4 Oe have not been found to produce adverse effects directly in humans. Instead, indirect hazards associated with B fields in MRI are due to the forces exhibited on ferromagnetic materials and on moving electrical charges. Hardy K, Meltz ML, and Glickman R, eds., *Non-Ionizing Radiation: An Overview of the Physics and Biology* (Medical Physics Publishing, Madison, 1997), p268.

[143] M. Büttiker, Y. Imry, R. Landauer, and S. Pinhas, Phys. Rev. B **31**, 6207 (1985).

[144] C. H. Xu, C. Z. Wang, C. T. Chan, and K. M. Ho J. Phys. Condens. Matter. **4**, 6047 (1992)

[145] S. Sanvito, C. J. Lambert, J. H. Jefferson, and A. M. Bratkovsky, Phys. Rev. B **59**, 11936 (1999).

[146] S. Datta, *Electronic Transport in Mesoscopic Systems*, edited by H. Ahmed, M. Pepper, and A. Broers (Cambridge University Press, Cambridge, 1995).

[147] *Green's function in Quantum Physics* (Springer-Verlag, New York, 1983), 2nd ed.

[148] M. Brandbyge, J. -L. Mozos, P. Ordejón, J. Taylor, and K. Stokbro, Phys. Rev. B **65**, 165401 (2002).

[149] D. Sanchez-Portal, P. Ordejon, E. Artacho, and J. M. Soler, Int. J. Quantum Chem. **65**, 453 (1999).

[150] N. Troullier and J. L. Martin, Phys. Rev. B **43**, 1993 (1991).

[151] O. F. Sankey and D. J. Niklewski, Phys. Rev. B **40**, 3979 (1989); E. Artacho *et al.*, Phys. Status Solidi B **215**, 809 (1999).

[152] D. Tománek, M. Yoon, J. M. Pacheco, G. K. Gueorguiev, S. W. D. Bailey, and C. J. Lambert (in preparation).

[153] Mark A. Reed and James M. Tour, Scientific American **282**, Number 6, p. 86 (2000).

[154] J. Chen, M.A. Reed, A.M. Rawlett, and J.M. Tour, Science **286**, 1550-1552 (1999).

[155] Jorge Seminario, Angelica G. Zacharias, and James M. Tour, J. Am. Chem. Soc. **122**, 3015 (2000).

[156] M. Di Ventra, S.T. Pantelides, and N.D. Lang, Phys. Rev. Lett. **84**, 979 (2000).

[157] M. Di Ventra, S.T. Pantelides, and N.D. Lang, Appl. Phys. Lett. **76**, 3448 (2000).

[158] We use the Amsterdam Density Functional (ADF) code, as documented in G. te Velde and E. J. Baerends, J. Comp. Phys. **99**, 84 (1992).

[159] R. Landauer, Phil. Mag. **21**, 863 (1970).

[160] J. Chen, W. Wang, M. A. Reed, A. M. Rawlett, D. W. Price, and J. M. Tour, Appl. Phys. Lett. **77**, 1224 (2000).

[161] Katsuhiko Okuyama, Yasushi Numata, Shino Odawara, and Isamu Suzaka, J. Chem. Phys. **109**, 7185 (1998).

[162] D. Tománek and M. Schluter, Phys. Rev. Lett. **67**, 2331 (1991).

[163] Chen J, Su J, Wang W, and M. A. Reed, Physica E **16** 17 (2003).

[164] J. L. Mozos, P. Ordejon, M. Brandbyge, J. Taylor, and K. Stokbro, Nanotechnology **13**, 346 (2002); J. Taylor, M. Brandbyge, and K. Stokbro, Phys. Rev. Lett. **89**, 138301 (2002); S. K. Nielsen, M. Brandbyge, K. Hansen, K. Stokbro, J. M. van Ruitenbeek, and F. Besenbacher, Phys. Rev. Lett. **89**, 66804 (2002); M. Brandbyge, K. Stokbro, J. Taylor, J. -L. Mozos, and P. Ordejon, Phys. Rev. B **67**, 193104 (2003).